MAX-PLANCK-INSTITUT FÜR KOLLOID- UND GRENZFLÄCHENFORSCHUNG

Controlled Condensation to Functional Materials – Synergetic Effect of Nitrogen-content and Pore Structure

Dissertation

zur Erlangung des akademischen Grades
Doktor der Naturwissenschaften („Doctor rerum naturalium“, Dr. rer. nat.)
in der Wissenschaftsdisziplin „Materialwissenschaft“

eingereicht an der Mathematisch-Naturwissenschaftlichen Fakultät
der Universität Potsdam

von

Janina Kossmann

Potsdam, 26.01.2022

Hauptbetreuer: Prof. Dr. Dr. h.c. Markus Antonietti
Zweitbetreuer: Prof. Dr. Andreas Taubert
Mentorin: Dr. Maria Nieves López-Salas

Gutachter/innen: Prof. Dr. Dr. h.c. Markus Antonietti
Prof. Dr. Andreas Taubert
Dr. Ana Primo

Published online on the
Publication Server of the University of Potsdam:
https://doi.org/10.25932/publishup-53693
https://nbn-resolving.org/urn:nbn:de:kobv:517-opus4-536935

Acknowledgment

First of all, I would like to thank my supervisor, Prof. Markus Antonietti, for the opportunity to be part of this impressive department and conduct my research here, at the *Department of Colloid Chemistry* at the Max Planck Institute of Colloids and Interfaces.

I would like to acknowledge Prof. Taubert from the University of Potsdam for the supervision of the thesis.

Then, I would like to express my most sincere gratitude to my mentor and group leader Dr. Nieves López-Salas. She gave me great support through my years here and supported me in every situation I had to face. Thanks for the fruitful scientific discussions and the support. She is always positive and visionary. She helped me to solve difficulties and encouraged me. She taught me a lot in the field of carbonaceous materials and all the applications but also about human interactions and relations. She helped me to grow a lot in the last two and a half years. Thank you Nieves for being such a great mentor and friend.

With me growing, also my group grew a lot over time. And here is the moment to say my greatest thanks to my friend and colleague Enrico Lepre. He was with me from the very first day and always supported me. We got to know the institute and Potsdam together. Thanks, Enrico for all the support and the great friendship. It was a pleasure to work with you. But also of course to the rest of my group: Maria, Sol, Mateusz, Jessica, and Chun: Thank you for the support, nice discussions, and coffees together. I could not imagine a better group to work with.

I am very thankful for all collaborations during my PhD time. Starting with Nadja Tarakina, Diana Piankova, and Hannes Zschiesche from the MPI. Thanks for all the electron microscope work, the time we spend together at the microscope, and the super interesting scientific discussions. Thanks to Josep Albero from the Institute of Chemical Technology in Valencia for the time

together at the MPI and the followed collaboration. Thanks to Julian Heske and Thomas Kühne for the theoretical studies.

I am also very grateful to all colleagues and technicians for data collection. Thank you Rona Pitschke, Heike Runge, Bolortuya Badamdorj, Antje Völkel and Jessica Brandt.

I would also like to thank all my colleagues and friends from the MPI. Thank you for all the wonderful and fun time inside and outside the institute, for all the BBQs and beers in CB, the coffee breaks when nothing seems to work anymore, and for always cheering me up. Thanks to my MPI family! Thank you, Enrico, Stefano, Diana, Cansu, Nieves, Majd, Simon, and many others. A special thank you at this point to Diana and Cansu. I am unbelievably happy that I met you here. Thanks for being there for me in every situation, for supporting me, pushing me, and just being who you are.

Not so close to me distance-wise but very close mental-wise: My good old friends, spread all over Germany. You always supported me to reach for more. You gave me distraction when needed and were understanding when I needed to focus on the work. Thanks for being such an important part of my life Charly, Celina, Luci, and Coline (“die Babos”), Caro and Julia (“JaCaJu”), Flo and Gereon.

Last but not least special thanks to my family. Thank you for all the support over the years. Special thanks to my sister Christin. Thank you for the great support and for always pushing me for more. You have always been a role model for me (yes, it is hard to admit this). Vielen Dank auch an meine Familie. Danke, für die stetige Unterstützung und den Rückhalt.

Table of Contents

1. Motivation

The development of carbonaceous materials is of great interest for several applications including gas adsorption, electrochemical storage and conversion, or heterogeneous catalysis. All these applications are important for a sustainable society. With the exploration of the high performance of graphene in 2004, the interest in carbonaceous materials grows even more.[1] Unfortunately, the synthesis of graphene is not yet optimized in large scale, hence the use of the material is limited. Amorphous carbonaceous materials present a highly attractive alternative. In spite of, the knowledge about amorphous carbonaceous materials is broad, a lack of control over the condensation process, and with this over the precise design of the carbonaceous product, still exist. Two main properties of amorphous carbonaceous materials set the key to a high performance: The chemical structure, i.e. nitrogen-doping of the carbonaceous material, and the pore structure. The control and optimization of these properties can synergistically facilitate the interaction with different substances and thus enhance the efficiency of carbonaceous materials for several industrial applications. Within this optimization, the principle of *simple is better* should be kept in mind. Meaning, the process should lead to a minimization of waste, chemicals, and energy consumption to keep it sustainable and industrially applicable. Therefore, the choice of the precursor is of essential importance, leading to optimization of the product. This was suggested by Oschatz and Antonietti in 2018[2] with the concept of noble carbons, which states, that the choice of a stable, nitrogen-containing precursor will lead to an even more stable, nitrogen-doped carbonaceous material with promising properties. Molecules fulfilling this requirement are for example nucleobases. They are very stable molecules, shown also by the fact, that they are Nature´s choice to store the most important information.[2] By using a molecular, stable, high nitrogen-containing precursor, the simplicity of the synthetic route is given and it also allows the simple encoding of element connectivity.

With a more controlled condensation process, investigations on the structure-performance relation would also be more accessible. Main structural properties like nitrogen content as well as the pore structure, have an interplay influence on the performance and influence each other during synthesis, which makes this task challenging. A controlled nitrogen content in combination with control over the built pore structure in carbonaceous materials would give the possibility to design material properties according to different applications. One appealing approach is the smart choice of precursor and templating methods. If this can be achieved, the implementation of carbonaceous materials for several applications in industry can be targeted and all the appreciable aspects of carbonaceous materials like high thermal and chemical stability, electrically conductivity, tailorable pore structure, availability, and safe handling can be used.

2. Background

2.1 Carbonaceous Materials

Carbon has the second largest library of known chemical compounds, only surpassed by hydrogen. It is ranked as the 17th abundant terrestrial element but probably the most important one.[3] The wide vitality of carbon comes from its position in the periodic table of elements. Carbon has the ability to form bonds with elements with low and high electronegativity and itself. This versatility makes carbon the basis of organic life on earth and facilitates its use in many current technological applications. Besides organic compounds, carbon is also present in inorganic substances in the form of carbonates (i.e. minerals).[4-6] Until 1828 it was believed that carbon-based molecules can only be obtained from living organisms. With the synthesis of urea from an inorganic reagent by Friedrich Wöhler, the synthetic organic chemistry was born.[7-8] While numerous carbon-containing substances are topic of organic chemistry, the number is rather limited for material science. However, carbon appears in several allotropes with different chemical structures and properties while solely consisting of carbon. The most known allotropes are diamond, graphite, fullerenes, and carbon nanotubes (CNTs) (**Figure 2.1-1 A-D**). In diamond, carbon is sp^3-hybridized and ordered in a cubic crystal structure. Diamond is the hardest natural existing material, transmitting visible light, and has a wide band gap (5.5 eV).[6] In contrast to this, graphite is a black, soft material with sp^2-hybridized carbon which builds a hexagonal, honeycomb-like crystalline structure. The electron delocalization within the π-orbitals makes graphite electronically conductive.[9] Fullerenes, CNTs, as well as graphene (a single sp^2 carbon layer) can be assigned to the class of nanostructured sp^2-hybridized carbon allotropes.[10-12] Despite the astonishing properties of these crystalline materials they are not used in large-scale applications because of their high production costs. The synthesis requires usually harsh conditions (i.e. Hummers method to obtain graphene[13-14]) or a lot of energy (i.e. chemical vapor

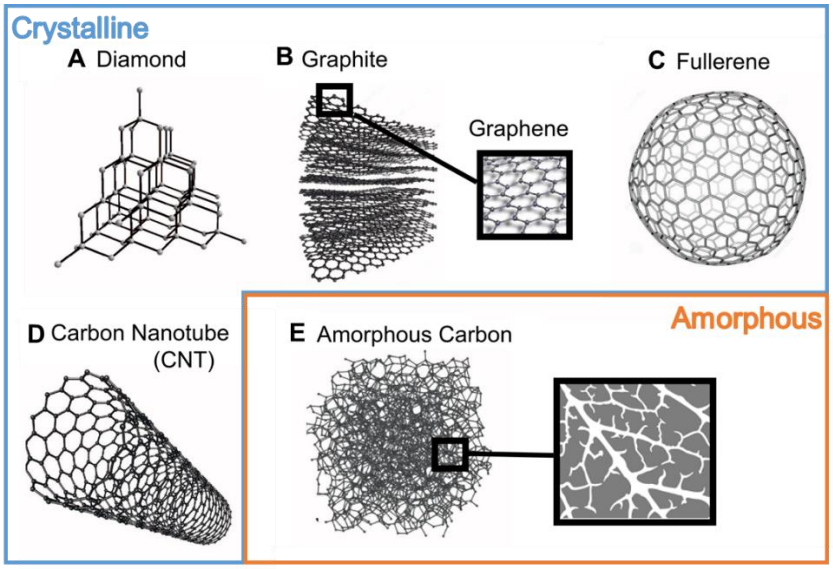

Figure 2.1-1. Atomic structures of most prominent carbon allotropes. Crystalline: A) diamond, B) graphite with single-layer graphene, C) fullerene, D) carbon nanotube (CNT), and E) amorphous carbon (with pore network).

deposition).[15] By replacing carbon six-membered rings of graphene by five- or seven-membered rings, other motives, or defects the structure gets distorted and amorphous carbon (**Figure 2.1-1 E**) with a highly defective nature is obtained. The high degree of disorder and defects cause an intrinsically large amount of pores with different sizes and architecture. This pore structure makes them stand out of the group of carbon allotropes. While porous carbons are not staying behind the crystalline carbon allotropes in terms of chemical, thermal, and mechanical stability, they have a tunable pore structure, simple processing, and are cheaper to produce.[16] As different applications demand different properties of a material, the possibility to adjust the pore structure according to the desired application gives a tremendous benefit. Thus, porous carbon materials are explored for a wide range of applications like as electrode material, in electrocatalysis, heterogeneous catalysis, water purification, or gas separation and storage, among others.[17-23] Different ways to introduce and adjust the pore structure and synthetic procedures to obtain and modify the chemical nature of carbonaceous will be discussed in section 2.2.

2.2 Introducing Porosity to Carbonaceous Materials

As mentioned, the porosity of carbonaceous materials has a big impact on the properties and applicability of the material. Several ways are known to introduce and modify the porosity. The most prominent procedures will be discussed in the following.

Activation

Activation of carbon materials describes the formation of pore volume and surface area by etching of carbon from the network. Different methods are known.[24-25] Carbon dioxide and water vapor (i.e. steam activation) activation includes a two-step procedure. First, the carbonaceous material is obtained by heat treatment in an inert atmosphere, followed by treatment with the activation agent at high temperatures. The activation with carbon dioxide follows the well-known Boudouard equilibrium (Equation 1.1.). At high temperatures, the equilibrium shifts to gaseous carbon monoxide. By CO_2 activation narrow micropores with a narrow pore size distribution (PSD) develop. Steam activation results in micropores with a broader PSD and slightly more mesoporosity.[26] Water etches carbon due to the formation of CO and H_2 (Equation 1.2.). With the formation of CO, the water gas shift reaction can take place, creating CO_2 (Equation 1.3), which can then act as an additional activation agent.

$$\mathrm{x CO_2(g) + C_y(s) \rightleftharpoons 2x\,CO(g) + C_{x-y}(s)} \quad (1.1)$$

$$\mathrm{x H_2O(g) + C_y(s) \rightleftharpoons xCO(g) + xH_2(g) + C_{y-x}(s)} \quad (1.2)$$

$$\mathrm{CO(g) + H_2O(g) \rightleftharpoons CO_2(g) + H_2(g)} \quad (1.3)$$

This activation methods are rather simple and broadly applicable but connected to high energy consumption, gives low carbon yields, and requires a two-step procedure. An alternative is the use of dehydration agents (like $ZnCl_2$, H_3PO_4, or KOH) in a one-step process, in which the precursor is impregnated with an aqueous solution of the dehydration agent and subsequently

carbonized.[27-29] After removing the dehydration agent the carbonaceous product is obtained in higher yields compared to carbon dioxide and steam activation. Besides the higher yields, the porosity can be adjusted by the activation agent to precursor ratio and the temperature.[30] The main drawback of this approach are possible inorganic impurities in the product.

All activation approaches described up to now are top-down methods, causing a lack of control over the induced porosity. The formation of worm-like or bottleneck pore structures for example can cause inaccessibility for some guest species and thus hinders the performance as catalysts.[31-32]

Templating

Another procedure to introduce porosity to carbonaceous materials and enhance the transport properties of the materials is using templates. Templating in general means the synthesis of a substance in the presence of a structure-directing agent (the template). The removal of the template leaves voids, which are the pores. The principle of templating was already used in macroscale for 6000 years. Within the process of casting, a liquid material was poured into a copper mold (the template) to produce tools and weapons. This process scaled down to the nanoscale (i.e. nanocasting) is now well known and used to obtain porous nanomaterials. The first material obtained with nanocasting was a porous carbon for chromatography in 1980,[33] but it was needed until 1998 until the term nanocasting was introduced for the synthesis of a porous polymer network with a silica template.[34] Today a large variety of templating methods to obtain well-defined bimodal, multimodal and hierarchical pore systems are known.[35-40] The herein presented template methods are classified according to the nature of the template: Hard, soft, and salt melt templating.

By using hard templates, as the name implies, the template holds the nanostructure of the precursor during the carbonization. Usually, the template is an inorganic solid like silica, zeolite,

or alumina membrane.[41-43] **Figure 2.2-1 A** shows the principle process of hard templating. The template is impregnated with a precursor, which polymerizes inside the pores of the template during the carbonization process. After removing the template, a carbon replica of the template is left.[44] The removal of the template is usually accompanied by harsh conditions like the use of hydrogen fluoride. Many studies about the synthesis of uniform microporous carbons by using hard templates, especially zeolites and silica can be found.[45-47] The obtained carbons by zeolite templating are usually not as ordered as their template. Zeolite has very narrow pores which can cause a geometrical mismatch between the narrow pores and the carbon material. Using silica as a template on the other hand offers a wide range of pore sizes and the materials can be designed more precisely. The most used silica templates are MCM (Mobil Composition of Matter),[48] SBA (Santa Barbara Amorphous type of materials),[49-50] and KIT (Korea Advanced Institute of Science and Technology).[51] These silica templates are interestingly achieved via soft templating.

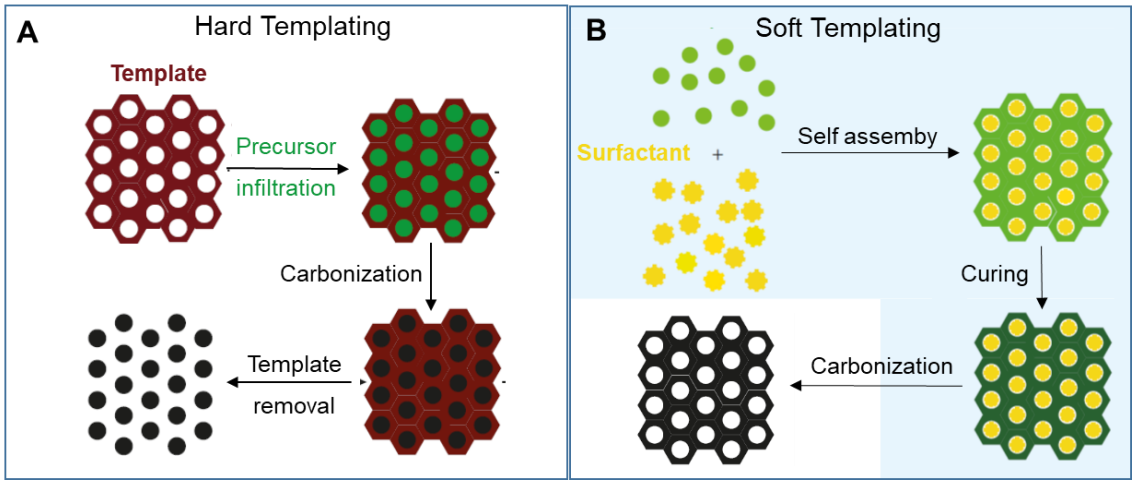

Figure 2.2-1. Schematic illustration of the principle of hard and soft templating.

Within soft templating, the template serves as a mold around which the framework is built and acts as a structure-directing agent. The process, shown in **Figure 2.2-1 B**, is driven by self-assembling of the precursor around the template with subsequent polymerization of the

precursor around the template.[52-53] The self-assembly is driven by non-covalent, weak interactions like Coulomb and Van-der-Waals forces. During carbonization, the template can either serve as a carbon source or be sacrificed to form the final pore structure. Common templates are for example block-copolymers like P123[1] from the Pluronic® family[54-55] or CTAB (cetyltrimethylammonium bromide). The advantage compared to hard templates is that no additional step of template removal is needed after carbonization and a higher control over the mesopores structure can be achieved.[56] However, the process requires the ability of the precursor to self-assemble into nanostructures, and the stability of the template during the crosslinking of the precursor as well as the stability of the resulting material during the decomposition of the template. All these restrictions limit the number of precursors that can be used. The presented methods to introduce porosity are well established but come have several disadvantages like the mentioned requirements, a rather difficult synthesis, high costs, or they require harsh conditions to remove the template.

Salt melt Templating

An inexpensive and sustainable approach with a high control over the porosity is given by the use of salt melt templating. In 1992 Rodriguez-Reinoso[57] reported the synthesis of microporous activated carbon using $ZnCl_2$, where the liquid phase on $ZnCl_2$ during carbonization can migrate in between the carbon layers and cause separation. It is also reported, that the incorporation of zinc prevents the contraction of the carbon network and increases the carbon yield. Even though $ZnCl_2$ was seen as an activation agent, the studies about the use of an inorganic salt within heat treatment raised and it was questioned if the use of an inorganic salt presents a new templating category.[24, 30] By now, “salt templating” is seen as a self-standing templating method.[58-59] The synthetic procedure includes mixing of the precursor with inorganic salt, let is undergo the

[1]PEO–PPO–PEO (poly(ethylene oxide)-b-poly(propylene oxide)-b-poly(ethylene oxide)

carbonization followed by simple water or acidic washing for salt removal. **Figure 2.2-2** illustrates the principle of salt melt templating. When the mixture of the salt and the carbon precursor is heated to the melting point of the salt, the carbon precursor dissolves in the liquid salt. With increasing temperature, the carbon precursor starts to polymerize and salts out of the liquid salt until the temperature is raised further and the precursor carbonizes. After cooling down to ambient temperatures the salt can be washed out with water or acid and the porous carbon is obtained. The only requirements are that the melting temperature of the salt has to be below the operating temperature and the precursor has to be soluble in the liquid salt. The melting temperature of the salt can be adjusted by changing the salt or using eutectic mixtures. In 2013 Fechler et al.[58] presented the use of different eutectic mixtures (i.e. $LiCl/ZnCl_2$, $NaCl/ZnCl_2$, and $KCl/ZnCl_2$) and the resulting differences in porosity. The differences in porosity are ascribed to different melting temperatures and the miscibility of the salt melts with the precursor.

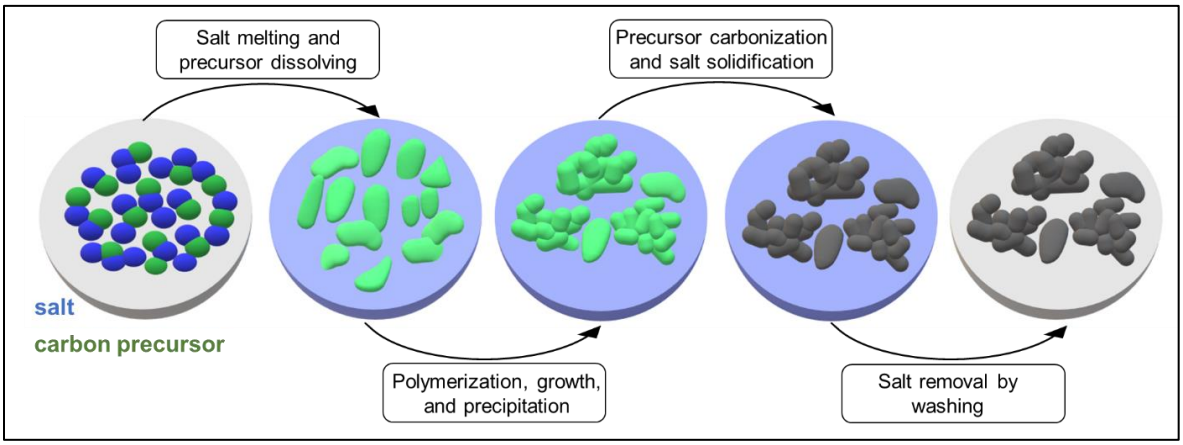

Figure 2.2-2. Schematic illustration of the principle of salt-melt templating. In a first step, the salt and the precursor are mixed. With increasing temperature, the salt melts and the precursor dissolves in the melt. With further increasing temperature, the precursor starts to condensate and polymerize. Upon a particular size, the polymer is not soluble in the salt and precipitates. With further heating, the polymer carbonizes. By cooling down the salt solidify and after washing off the salt, the carbonaceous material is obtained.

Besides a high variety of inorganic salts, also the operating temperatures and the salt to precursor ratio can be used to adjust the pore structure and morphology of the carbonaceous product.[58, 60-62] A lower salt content creates more microporous materials whereas a higher salt

content also introduces some mesoporosity. The use of inorganic salt as templates is convenient for different reasons. The pore structure of the final carbonaceous product can be adjusted by simple changes of the salts, the salt content, and the operating temperature. The procedure is simple, does not contain the use of any toxic chemicals or harsh conditions, and the salt can be reused.

2.3 Nitrogen Containing Carbonaceous Materials

Besides adjusting the pore structure, the incorporation of heteroatoms to the carbon network can further improve their physico-chemical properties. This adjustment of the composition of carbonaceous materials can cause changes in the position of the valence and conductive band, their work function, the oxidative/reductive, and the acid/base behavior and therefore affect the efficiency in many different applications.

Within the different heteroatoms introduced to the carbon network (i.e. N, B, S, P, O), nitrogen is the most extensively investigated. Different local nitrogen functionalities like pyridinic-N, pyrrolic-N, pyrazinic-N, graphitic-N, or as oxide-, nitro-, or amino-group can be inserted (**Figure 2.3-1**).

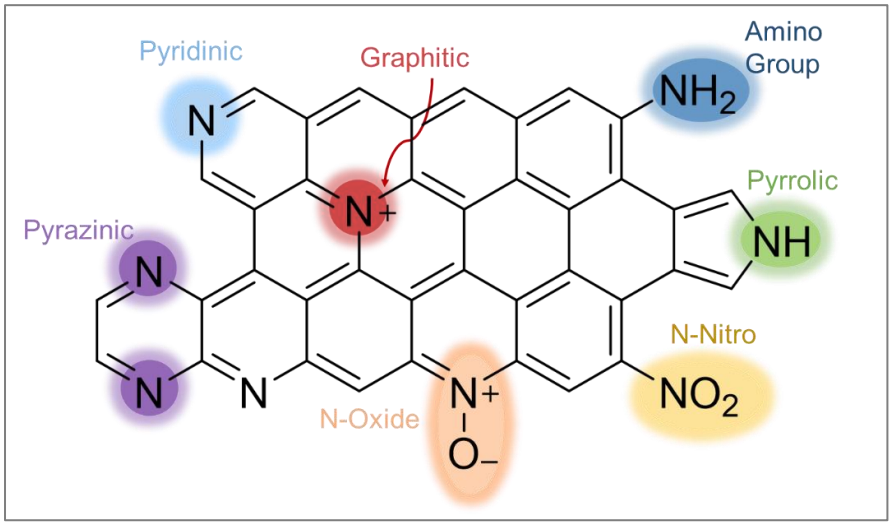

Figure 2.3-1. Selection of possible nitrogen functionalities within carbonaceous materials.

Nitrogen can be introduced by post- or pre-synthetic trategies causing structural modifications. Post-functionalization can be achieved for example by heat treatment of carbon in ammonia atmosphere but giving limited access to control the nitrogen content and functionalities.[63-65] Within the pre-synthetic strategy a nitrogen-containing source is added directly to the carbonization process or a nitrogen-containing substance is used as precursor.[66-67] Within the carbonization process the majority of not stable functional groups (-OH, -COOH, -NH_2) are leaving in form of gases due to complex pyrolysis reactions (like dehydrogenation and condensation) and mainly stable functional groups incorporated in the carbon network are staying. Resulting in nitrogen-doped carbonaceous materials (NCs). The used precursors can be of synthetic or natural, biomass-derived nature. Biomass-derived precursors have the advantage of no additional synthetic procedure towards the precursor and the use of renewable resources. Suitable are carbon- and nitrogen- containing, organic materials like wood,[68] prawn shells,[69] chitosan,[70] and agricultural waste among others.[71] By using natural precursors the design of the carbonaceous product is limited and the yields are low. More possibilities to influence the carbonaceous products are given by the use of synthetic precursors. Common synthetic precursors are cross-linked materials like zeolitic imidazole frameworks (ZIFs),[72] MOFs,[73-74] porous aromatic frameworks,[75] or conjugated microporous polymers[76] and non-crosslinked materials like linear polymers, such as polyimides,[77] polypyrroles,[78-79] polyanilines,[80-81] and polymeric ILs.[82] Most of them are pre-condensed or cross-linked polymers or oligomers. The significant disadvantage of those is the synthesis prior to the final heat treatment. This makes the process more complicated and cost-intensive, but usually brings the advantage of a sufficient yield.[83] Most molecules completely decompose when exposed directly to temperatures up to 1000 °C. Therefore, the literature about molecular precursors for nitrogen containing carbonaceous materials is rare. Anyway, the use of molecular precursors would highly simplify the synthetic route. Molecules with strong intermolecular interactions or a low vapor pressure are suitable to obtain carbonaceous materials

with high carbon yields. Also, the elimination scheme throughout the condensation should yield stable leaving groups like CO, CO_2, SH_2, or NH_3. Nucleobases are a good example of suitable molecular precursors. They are thermodynamically stable compounds with a high nitrogen content. Indeed they have already been used as molecular precursors for highly nitrogen-doped carbonaceous materials.[84-86] Another example of a suitable molecular precursor that satisfies the mentioned criteria and has already been used are ILs.[87-90] They have a low vapor pressure, and by choosing ILs with condensable groups (i.e. cyano groups) a stable intermediate polymer can form and prevent the formation of volatile compounds.

The final nitrogen content not only depends on the used precursor but also on the synthetic conditions. With increasing temperature, the nitrogen content usually decreases. A broad range of nitrogen contents can be found in literature from very low (1-2 wt%) to higher values of up to 20 wt%.[91-92] With increasing investigations on NC materials, the ability to synthesize materials with higher nitrogen contents were explored, simultaneously. With increasing nitrogen content, the properties contrast significantly compared to bare carbon materials and therefore deserve to be seen as a separate class of materials. Even though the border is vague, just materials below a C_3N composition (25 mol% nitrogen) will be called NCs in this thesis. Terminology wise all nitrogen containing carbonaceous materials can be called carbon nitrides but with the discovery of C_3N_4 and the following bloom, the term carbon nitride is mostly connected with C_3N_4. Nevertheless, herein the term “carbon nitride” will be used as generically for materials above a C_3N composition (as illustrated in **Figure 2.3-2**).

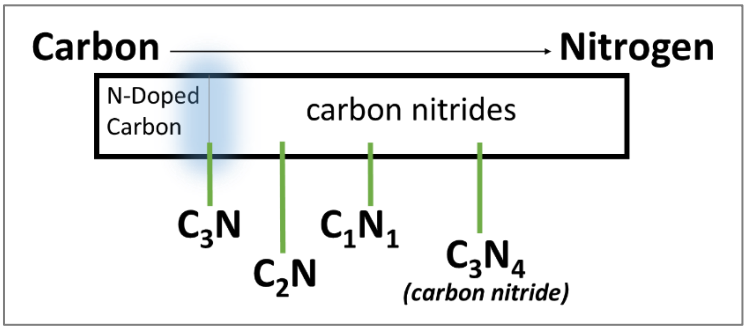

Figure 2.3-2. Selection of members of the carbon nitride family with increasing nitrogen content.

2.4 Carbon Nitrides

The first report about a solid-state carbon nitride goes back to 1834, when Liebig described the thermolysis and condensation of dithiocyan (SCN) to a carbon nitride material.[93] It happened to pass a long time until carbon nitrides were rediscovered in the mid-1980s with a theoretical paper by Cohen.[94] He proposed a hypothetic cubic carbon nitride, which could exceed diamond in properties like hardness and thermal stability. This was followed by different theoretical calculations and synthetic approaches to synthesize a crystalline solid of the proposed kind. Within those, carbon nitrides with different structures and compositions (like C_3N, C_2N, C_1N_1, and *g*-C_3N_4) were explored.

C_3N_4

The most prominent member of the carbon nitride family is graphitic carbon nitride (*g*-C_3N_4), which consists of polymeric chains and graphitic layers of N-rich aromatic rings constituted of triazine or heptazine monomer units linked together with N-bonds (**Figure 2.4-1**). They can be synthesized by heat treatment of N-rich precursors like urea or melamine. The demonstration of its excellent photocatalytic performance under visible light in 2009[95-96] further increased the research interest in *g*-C_3N_4 and was followed by numerous publications. The research within the field of *g*-C_3N_4 is beyond the scope of this thesis and will not be further discussed herewith refer to some reviews.[97-102]

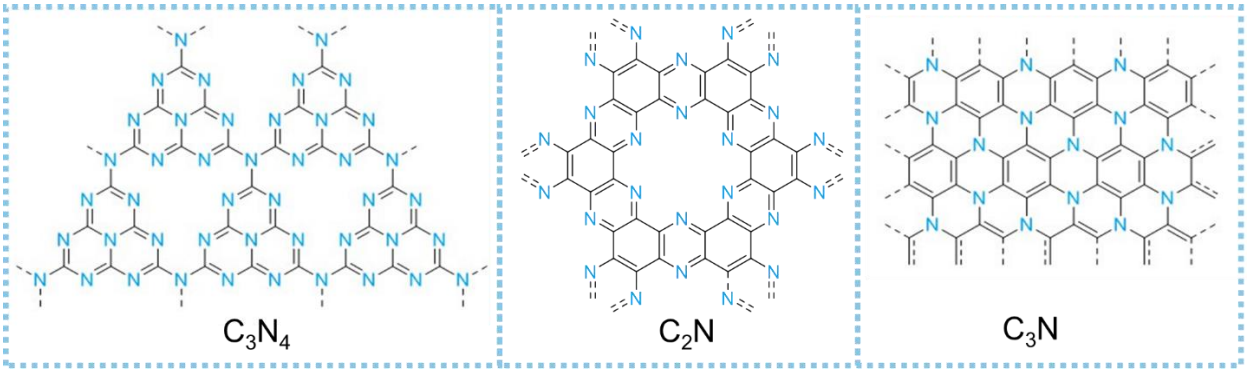

Figure 2.4-1. Ideal molecular structures of C_3N_4, C_2N, and C_3N.

C_2N

C_2N materials are thermally stable up to 750 °C, are conductive, and obtain a high surface area.[103-105] The covalent structure is ideally composed of 77 mol% carbon and 33 mol% nitrogen, with a well-defined skeleton and structural nanopores as shown in **Figure 2.4-1.** The benzene rings in the ideal C_2N structure are connected by bridging nitrogen atoms, which provides a large π-electron pool to the network with an intrinsic electron density on the nitrogen atoms.[104] The structural pores build by this structure are called N6-cavities, and make C_2N materials suitable for anchoring metal single atoms or metallic nanoparticles.[106-107] The high content of nitrogen brings also high polarity to the surface of the material, which is for example beneficial for applications where the wettability of the material is important. Such applications are for example deionization, membrane separation, and (electro)catalysis.[108-110] C_2N materials have been explored for several applications and proven to show special performance in gas and water adsorption[111-112] and energy storage.[113-117] Likewise, different synthetic procedures towards C_2N materials are reported. Fechler et al. reported the salt melt template synthesis of bulk C_2N materials from hexaketocyclohexane and urea to obtain microporous C_2N in 2016.[103] Walczak et al. obtained C_2N materials with a surface area of 1000 $m^2 g^{-1}$ without any templating by the direct condensation of hexaazatriphenylene crystals as molecular precursor.[112]

The synthetic procedure has an important impact on the final C_2N material. Different synthetic strategies like solvothermal or ionothermal synthesis or direct bulk condensation are described in the literature. By a solvothermal synthesis, with low temperatures, the formation of a regular 2D crystalline structure is favored. These materials are beneficial for semiconductor applications.[118] When synthesized by ionothermal synthesis or direct bulk condensation with higher temperatures, the formation of rings and further condensation between the pore walls results in a 3D highly porous structure, which is more appealing for applications like adsorption and energy storage.[105] At this point I would like to advise the reader to read the recently published review of Tian et al.[105] for more insights into C_2N materials.

C_3N

C_3N materials possess a graphene-like crystalline structure with ideally 25 mol% of nitrogen, shown in **Figure 2.4-1**.[119] They show good chemical stability and an indirect band gap, which makes them promising for semiconductor applications. The synthesis of C_3N crystalline flakes from the molecular precursor m-phenylenediamine is described in 2013 by King et al..[120] In contrast to C_3N_4 and C_2N, C_3N has no structural pores but a honeycomb lattice as described by Yang and coworkers. They obtained the 2D material by hydrothermal synthesis of 2,3-diaminophenazine.[119] Reports about the utilization as photocatalyst, gas adsorbent,[121-122] electrocatalyst,[123-124] and for energy storage devices[125] can be found.[116, 126] However, the performance of C_3N is limited due to the narrow band gap, but in combination with another wide-bandgap semiconductor the performance of the material can be improved significantly.[127-128] C_3N materials possess high potential and several theoretical studies about the properties of these materials can be found. However, the synthesis is still challenging and therefore still has a lot of potential for future research.[126, 129-130]

C_1N_1

Within the list of carbon nitrides, C_1N_1 materials are probably the ones the least explored. However, the story of $(CN)_1$ materials is not new as such. Considering C_1N_1 as a type of paracyan (i.e. the polycondensed structure of cyanogen), the first report can be found as early as 1782 by Macquer and Scheede about the production of HCN and HgCN.[131] Around 40 years later, Gay-Lussac produced paracyan as a brown solid by heating up silver cyanides.[132] During the mid-17th century many studies about paracyan, synthesized from a variety of cyanides can be found.[133] In 1954, Bircumshaw reported the synthesis of paracyan by heating up oxamide in a sealed tube. He described the material as a dark brown, black when fully polymerized, light powder with 32-34% carbon and 32-44% nitrogen.[134] After this, some reports about paracyan materials can be found [135-137] and also one patent by Labes and co-workers in 1986.[138] In 2009 May et al. published detailed investigations on the possible crystal structures of CN, suggesting the in **Figure 2.4-2** shown structures as most probable.[46] Especially proposed structure **C** fits very well with the other members of the carbon nitride family shown in **Figure 2.4-1**.

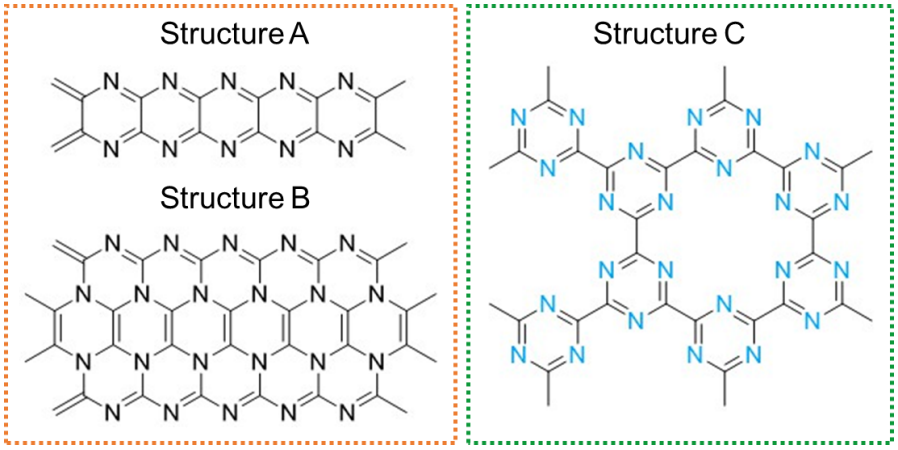

Figure 2.4-2. pCN structures proposed by P. W. May et al.[46] compromising sp^2 hybridized carbon.

Despite the long history and the theoretical papers predicting astonishing properties for C_1N_1 materials, more current reports are still rare. For instance, only a handful of papers described the synthesis of C_1N_1 materials and their properties. Cao et al. reported the solvothermal synthesis of

CN nanostructures in 2006 using cyanuric chloride and sodium as precursor.[139] In 2017 Li et al. reported a similar synthesis by using cyanuric chloride and sodium in an autoclave and their performance as anode material for Li-Ion batteries.[140] In 2020 Li et al. used cyanuric chloride on a copper surface to obtain C_3N_3 films and reported the photoelectrochemical activity for water splitting.[141] In 2019 Wu et al. reported the synthesis of Fe encapsulated in a C_3N_3 framework, derived from a covalent triazine framework (CTF), and their performance in oxygen reduction reaction (ORR), oxygen evolution reaction (OER), and hydrogen evolution reaction (HER).[142] Unfortunately, all these procedures contain either toxic substances like cyanuric chlorides as precursor or transition metals. However, they show the great potential of C_1N_1 materials, which were proposed by theoretical works long ago.

2.5 Applications of N-doped Carbonaceous Materials

As mentioned before, different properties of carbonaceous materials like pore structure and size, surface area, nitrogen content, and conductivity are beneficial for different applications, like the use as electrodes, catalysts, sensors, or adsorbents. **Figure 2.5-1** shows the variety of carbonaceous materials in terms of properties and applications. The ability to introduce heteroatoms and to tune the pore structure makes them for example suitable as selective gas adsorbents and separators.[143-144] Indeed, carbonaceous materials are already used as adsorbents in liquid phase separation for dye molecules in water treatment,[145] for filtration of drinking water,[146] and heavy metal removal. Conductive and high surface area materials are suitable as electrodes for energy storage and conversion devices.[18] The following chapters will describe two different applications in more detail. Section 2.5.1 will focus on the application as gas adsorbent and separator with the focus on carbon dioxide and water vapor as adsorptive. In section 2.5.2 the use of NCs in electrocatalysis, with the focus on the oxygen reduction reaction, will be discussed.

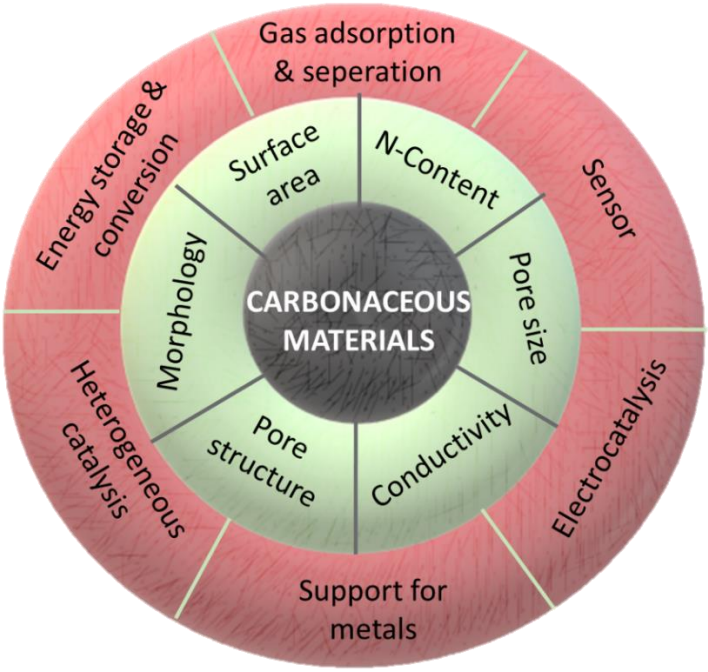

Figure 2.5-1. Schematic illustration of the variety of carbonaceous materials with different properties of carbonaceous materials and different applications.

2.5.1 N-Doped Carbonaceous Materials as Gas Adsorbent and Separator

2.5.1.1 Carbon Dioxide Capture

Due to the extensive use of fossil fuels, chemical processing, and deforestation the global CO_2 emission is rising for the last 80 years exponentially,[147] causing an increase in global warming. Increasing the CO_2 emission is one of the biggest challenges that society and the research community have to face in our days. Several long-time strategies are pursued to mitigate CO_2 emissions like neutral energy vectors, implementing systems to capture residual heat in power plants, reforestation, developing electric vehicles, and investigations on renewable energy sources and energy storage systems.

One way to make changes in a shorter time scale is CO_2 capture and storage. Finding a solution for efficient and selective CO_2 capture is an actual topic for material chemistry. The challenge in this is to capture it out of a low-pressure flux containing a high volume of other gases and a low percentage of CO_2. Currently, liquid state sorption using aqueous amine solutions is the choice in many power plants.[148] The flue gas is bubbled through a column with an aqueous amine solution where the amine reacts with CO_2 to carbamates in a reversible reaction. With increasing the temperature the reaction equilibrium is shifted back to the reactants, and CO_2 can be released.[148] This procedure shows a high efficiency but has drawbacks like solvent evaporation, the use of toxic amines, corrosion of the equipment, and a high energy demand for the process and regeneration.[149]

An alternative to chemisorption is sorption on solid materials. When developing new materials for efficient CO_2 capture, different aspects need to be considered:

- CO_2 needs to be separated out of a mixture of gases like He, H_2, O_2, N_2, and CH_4.
- The gas flow can have different temperatures, therefore the materials must be stable and efficient with a broad range of temperatures.
- The materials need to show a high capacity, meaning a high CO_2 uptake.
- A low regeneration energy. The energy to regenerate the material plays a key role for the implementation in big scale to make the process cost-efficient.

Several reports about materials for CO_2 capture already exist. Amine-based and calcium-oxide-based materials, as well as metal oxides, show a high selectivity but CO_2 is chemisorbed and therefore the regeneration requires a lot of energy which makes the process cost intensive.[150] On the other hand, physisorption over porous materials can give a high capacity and high selectivity even at low pressures. The materials are stable against common impurities, like water, and the regeneration is possible under mild conditions as the physisorption binding is

not so strong. The most prominent examples in this content are zeolites, MOFs, and porous covalent organic condensates. **Figure 2.5-2** shows an overview of the discussed materials for CO_2 capture.

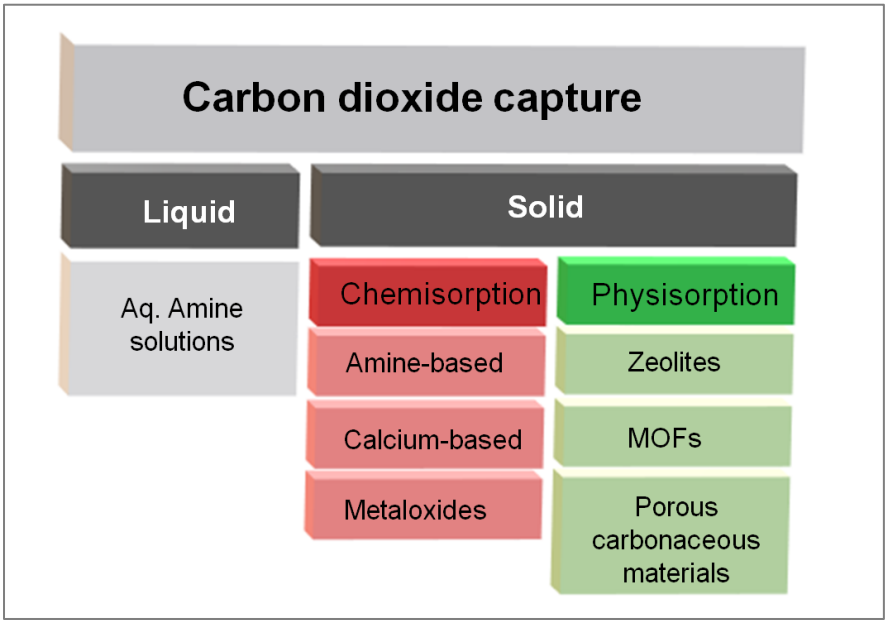

Figure 2.5-2. Overview of materials for CO_2 capture. Grouped into liquid sorbents, which are currently used in industry, and solid sorbents. Solid sorbents are further subdivided according to the sorption mechanism (i.e. chemisorption and physisorption).

Zeolites are already used in industrial scale. However, they show a relatively low selectivity and their capacity is sensitive towards temperature and the presence of water.[151] Some MOFs show a very high selectivity due to their high surface area and tuneability of the pore network. In addition, their meta-cation plays a key role in their high selectivity. Mg-MOF-74 for example shows an $IAST^{2}_{(CO2/N2)}$ selectivity of 182 at 298 K.[152] It is worth mentioning here, that also Rubisco, the natural CO_2 fixation protein, contains magnesium. Zaworotko et al. reported a MOF containing zinc and periodically arranged hexafluorosilicate ($SiFe_6^{2-}$) with an IAST of 1500.[153] Despite a high capacity and selectivity, MOFs are accompanied by a complicated synthesis which makes them

[2] Ideal adsorbed solution theory: standard to predict gas-mixture adsorption isotherms.

not cost-efficient for large-scale production.[150] In contrast to this carbonaceous porous materials are easy to synthesize and can be obtained from inexpensive and renewable precursors. In addition, they are known to be chemical and thermal stable. The regeneration energy is low due to the physisorption process. However, the selectivity and capacity for ordinary porous carbon are known to be rather poor.[144] Nitrogen functionalization can enhance the CO_2 capacity[154-158] and selectivity[144, 159-162] due to the introduction of basic sites in the carbonaceous network that helps binding CO_2 molecules. In addition to nitrogen functionalization of carbonaceous materials, also the pore structure can be tuned as discussed before. By adjusting the pore size similar to CO_2, van der Waals interactions of both sides of the pore wall add up each other and affect higher interactions. However, the values obtained so far are, as mentioned above, rather poor. Interestingly, Nature provides a great example of how selective CO_2 sorption is possible at low pressure from air using carbonaceous networks. Rubisco adsorbs CO_2 with an $IAST_{(CO2/O2)}$ of 1500. This value is way above the standard for synthetic materials[151, 163] but is what is the aim of the scientific community.

The use of carbon nitrides as solid CO_2 sorbents has already shown to be highly promising. The high nitrogen content arranged in for example N6-cavities gives a simultaneous optimization of the electronic structure, the polarity, and the pore size/geometry for CO_2 sorption.[144] This is for example reported for the C_2N material C-HAT-CN by Walczak et al.[143] The microporous material shows a negligible nitrogen uptake but a high CO_2 uptake, acting like a molecular sieve with an isosteric heat of adsorption of 52 kJ mol^{-1}. Theoretical calculation showed that the high binding enthalpy, which is far from being comparable to those of CO_2 and usual nitrogen-doped carbons, occurs due to the acceptor character of carbon in the C_2N materials together with stabilization/rebinding of nitrogen surrounding the CO_2.

2.5.1.2 Water Sorption

The adsorption of water might not seem useful at first glance. However, indeed a high adsorption of water to a material can contribute to mitigate the ever-growing energy demands. Cooling and heating of buildings consume ca. 20 – 50% of the global energy[164-166], and conventional compressor air conditioning uses electrical energy and thus contributes to CO_2 emissions.[166-167] Thermally driven adsorption chillers (TDCs) and adsorption heat pumps (AHPs) represent an environmentally friendly alternative to compressor air conditioning. Their working principle is based on reversible adsorption and desorption of an adsorptive (refrigerant) to an adsorbent, as shown in **Figure 2.5-3**. In a first step, the refrigerant evaporates with Q_{evap}, using for example waste heat and producing useful cold. The refrigerant is adsorbed by the sorption material with Q_{ads} and can be used to heat a cold steam. When the sorption material is full of the refrigerant, the second cycle starts with the desorption of the refrigerant by adding Q_{des} while producing useful cold again. The desorbed refrigerant condenses subsequently with Q_{cond}, heating up a cold steam. With this system, waste heat from industry, which is usually rejected to the environment, or solar heat can be used as driving force.[166, 168-169]

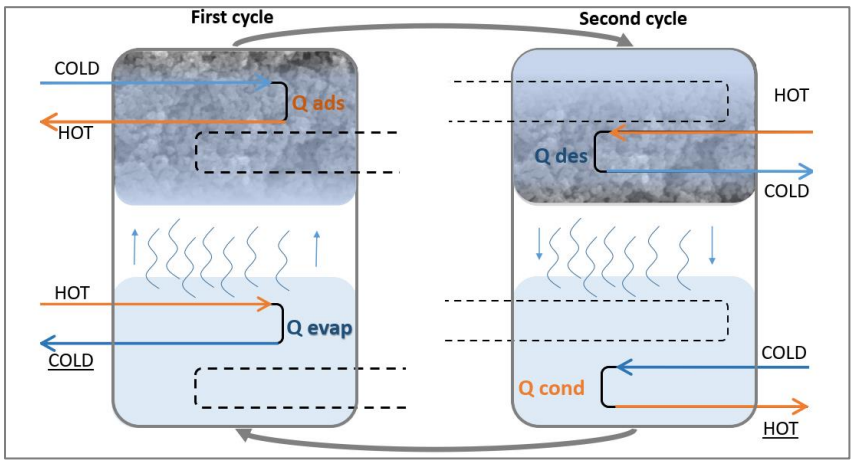

Figure 2.5-3. Schematic illustration of the working principle of thermally driven adsorption chillers (TDCs) and adsorption heat pumps (AHCs). The refrigerant (i.e. water) is evaporated with Q_{evap} and cooling a hot steam, the adsorbent adsorbs the vapor with Q_{ads}, which can heat a cold steam. In a second cycle, the refrigerant is desorbed by Q_{des} and condenses with Q_{cond}.

The efficiency and implementation to the large-scale of such systems strongly depend on the choice of the refrigerant and adsorbent. On one hand, water is the refrigerant of choice due to its high evaporation enthalpy, nontoxic character, and high availability. However, the choice of the adsorbent is not that straightforward as many requirements have to be fulfilled. For instance, the material should be thermally stable, easy to synthesize, cost-efficient in large scale, abundant, and hydrophilic. To maximize the efficiency, the material needs to have a high surface area and pore volume and a large water uptake at low relative pressures.[166, 170] Also a steep lifting in the uptake, appearing as an S-shaped isotherm, is favorable for practical use. A steep lifting in the uptake can be translated into a narrow range of relative pressures where a large loading can be achieved.[168] The onset of water uptake (i.e. the start of the S-shape) is influenced by the hydrophilicity of the material, and the maximum water uptake is correlated to the pore volume.[170] Currently, adsorbents used in industrial-scale are silica gels[171] and zeolites.[172] Besides the limited water uptake of silica gels, the adsorption happens at higher relative pressures. Zeolites show a higher uptake but the strong binding makes the desorption step too energy-consuming.[167] Other materials that are used as adsorbents are aluminophosphates and silica-aluminophosphates. The maximum water uptake of these materials is higher than those for zeolites but still comparably low (0.3 g g^{-1}).[169, 173] Their template-based synthesis makes the process not cost-efficient.[174] The current academic champions in terms of water uptake are MOFs.[175] Several reports about MOFs with a very high water uptake arose in the last decade. Janiak et al. reported for example a water uptake of 1.06 g g^{-1} for MIL-101Cr MOF functionalizes with nitro- and amino groups[176] and Abtab et. al report even a water uptake of 1.95 g g^{-1} for Cr-SOC-MOF-1.[177] However, the complicated multi-step synthesis of MOFs and their metal content makes them less cost-efficient and compromises their sustainability. Additionally, the chromium content in the mentioned MOFs might cause legislation issues.[178]

A chemical and thermal stable, low cost, metal free, and abundant alternative for TDCs and AHPs would be porous carbon or porous covalent materials. At the moment they are known to be hydrophobic and therefore, reports about TDC or AHPs with water as refrigerant are rare. When using carbons as adsorbents, the reported refrigerant are usually methanol or ammonia,[179-180] which comes with drawbacks like solvent loss, toxicity, and higher costs, which make them also not suitable for large-scale applications. However, the hydrophilicity of carbon materials can be tuned by heteroatom doping of the material. With the introduction of heteroatoms, a higher polarization of the material can be obtained. Thus, water sorption on carbon materials is now a topic of interest. The reported isotherms are generally S-shaped, type V, with a hysteresis loop.[181-182] By introducing functional groups to the carbon surface the onset and maximum uptake can be tuned due to the ability of hydrogen bonding. The review of Liu et al.[183] provides an overview of water sorption on porous and non-porous carbon materials and how functional groups and pore size influence the water loading. In summary, functional groups are necessary as nucleation sites for water on the otherwise hydrophobic carbon surface, meaning that functional groups have an influence on the low loading area while pore size and volume are more important in the higher loading region. Regarding the favorable pore size of water sorption, most researchers agree on microporous carbon materials being favorable for water sorption due to enhanced hydrogen bonding due to both pore walls that ultimately increase the water uptake.[183] Micropores shift the onset of water sorption to lower relative pressures and mesopores increase to maximum uptake.[183-184] Thommes et al.[185] reported about the influence of pore size and water uptake in ordered mesoporous carbon. They highlight that water adsorption appears in two steps by micro- and mesoporous filling. Additionally, they point out how sensitive water sorption is to small changes in the mesopores size.

Optimization of the pore structure of carbon nitride materials can result in highly efficient water sorbents. As already reported for C_2N materials, the N6-cavities provide attractive polar pores for

water adsorption, resulting in hydrophilic materials.[105, 143] However, the maximum water uptake is not yet sufficient for the application as AHPs or TDCs. By tuning of the pore volume, especially the mesopores volume, the total water uptake could be increased and open the door to the utilization of porous carbon nitrides as sorbents for TDCs and AHPs.

2.5.2 N-Doped Carbonaceous Materials as Electrocatalyst for the Oxygen Reduction Reaction

The demand for energy is increasing dramatically, and the need for greener energy conversion technologies is growing. One of the most promising technologies is seen in fuel cells (FCs). It presents a green alternative for combustion engines. In an FC, a fuel like hydrogen (or MeOH) is oxidized at the anode and oxygen is reduced at the cathode, producing water, which does not give problems to the environment. Depending on the electrolyte and catalyst, the reaction can take place in a two- or four-electron transfer mechanism (see **Scheme 2.5-1**). The four-electron process is usually preferred for FCs due to the inherent higher current per molecule of oxygen reduced and the prevention of hydrogen peroxide formation, which is known as a degradation source.

Scheme 2.5-1. Oxygen reduction reaction pathways in acidic and alkaline media.

Acidic media:

Two-electron $O_2 + 2H^+ + 2e^- \rightarrow H_2O_2$

$H_2O_2 + 2H^+ + 2e^- \rightarrow 2H_2O$

Four-electron $O_2 + 4H^+ + 4e^- \rightarrow 2H_2O$

Alkaline media:

Two-electron $O_2 + H_2O + 2e^- \rightarrow HO_2^- + OH^-$

$HO_2^- + H_2O + 2e^- \rightarrow 3OH^-$

Four-electron $O_2 + 2H_2O + 4e^- \rightarrow 4OH^-$

Table 2.5-1. Different types of fuel cells with the used electrolyte, operating temperature, catalyst, and sensitivities.

	Polymer Electrolyte FC	Alkaline FC	Phosphoric Acid FC	Molten Carbonate FC	Solid Oxide FC
Electrolyte	Polymer membrane	KOH	H_3PO_4	CO_3^{2-}	Ceramic
Operating temperature	80 °C	60-220 °C	200 °C	650 °C	600-1000 °C
Catalyst	Pt	Pt	Pt	Ni	Perovskites
Sensitive towards	CO	CO_2	-	-	-

A lot of different FCs are currently under development. They can be classified by the electrolyte and differ regarding the operating temperature, the catalyst, and the tolerance against impurities. A summary of different FCs is given in **Table 2.5-1**. Among them, polymer electrolyte FCs (PEMFCs) show the great advantage of operating near room temperature and not containing a corrosive liquid (e.g. like KOH in alkaline FCs).

The efficiency of FCs is strongly depending on the catalyst. In PEMFCs platinum is used as catalyst at the anode and the cathode. While the oxidation at the anode is sufficiently efficient, the reduction at the cathode builds the bottleneck for the efficiency of the cell. The cleavage of the O_2 bonds requires higher activation energy and the oxygen reduction kinetics are slow when compared with the anodic fuel oxidation. For instance, the hydrogen oxidation at the anode is by six times faster than the oxygen reduction reaction (ORR) at the cathode.[186] This requires a more selective and active catalyst towards ORR to implement this technology to large scale.

Currently, most used catalysts are platinum-based (e.g. platinum on carbon) due to their highly selective and efficient reduction of oxygen in a four-electron path mechanism.[187-190] However, the use of platinum comes with a lot of drawbacks like scarcity of platinum and thus high costs, long time instability, CO poisoning, and intolerance to methanol cross-over.[187, 191-194] These drawbacks promoted an intense exploration for alternative materials,[195] including precious and non-precious metals as well as metal-free catalysts. The use of carbonaceous materials showed promising

results in this context (especially in alkaline media)[196-200] and the introduction of additional non-noble metals can further improve the activity of the material.[187, 191, 201-203] As already mentioned in sections 2.3. and 2.4, the introduction of nitrogen into the carbon network can enhance the ability to anchor active metallic species.[204] Nitrogen induces electron relocalization, gives more electron donor functions, and stabilizes the metal.[2, 205] Additionally, the carbonaceous support can be designed as needed with the described methods in sections 2.2 and 2.3.[206] Carbonaceous materials show many advantages when compared with other supports. For instance, they are stable in a wide pH range, in high temperatures, and can be produced from low-cost, ready available precursors.

By reducing the size of the metal attached to the support from nanoparticles to single atoms the selectivity activity can be further increased.[207-209] The limiting factor when decreasing the size is the stabilization of the metallic atoms or clusters on the support surface and avoiding agglomerations into nanoparticles.[210] Theoretical studies, as well as experimental results, show that NCs are very promising candidates to stabilize small metallic particles and single atoms.[208, 211-213] Different synthetic routes are known to introduce metals into the carbonaceous network. One strategic way is in situ preparation by chemical vapor deposition, atomic layer deposition, or pyrolysis. Another strategic way is post-treatment of the carbonaceous support with the metal by impregnation and subsequent heat treatment.

Regarding ORR, iron and cobalt doped NCs appear to have great activity and stability but also show activity towards the Fenton-like radical oxygen activation pathway, which limits the practical approach of these materials due to the degradation of the polymer membrane in PEMFCs.[186, 214] Not only the metal itself and the metal size but also the coordination of the metal appear to influence the selectivity of the electrocatalyst. Recently Zhang et al. reported how the change in coordination of a Ni-SAC influences the mechanism of the reaction. When nickel is just coordinated to nitrogen (Ni-N_4) they obtained a highly selective two-electron path mechanism for

hydrogen peroxide production. If nickel was coordinated to nitrogen and oxygen ($Ni-N_2-O_2$) the reaction was going in a four-electron mechanism.[215] The importance of the environment of the metal is also reported by Zhaoyong and coworkers. They reported the highly selective hydrogen peroxide production attributed to nickel anchored by multiple oxygen defects.[216]

A look at Nature's solution for oxygen reduction can also inspire here. Nature's choices are copper containing metalloenzymes like laccase and amine oxidase.[191, 217-218] Thus, copper ligands have been tested and probed as an efficient bioinspired ORR electrocatalyst. Multiatom centers with different oxidation states of copper fostering different steps of the ORR mechanism.[219] Lu and coworkers reported that the more positive redox potential and the d-orbital density of weakens the O-O bonds.[220] This makes copper a promising candidate as electrocatalyst material for ORR. Indeed, copper decorated NCs were also tested as electrocatalysts for ORR, and Cu-N is claimed to be the active site.[186, 218, 221] As mentioned before the use of NCs as support brings the advantage of adjusting the porosity of the material according to the application. In this context, a high surface area is beneficial, since the reaction takes place at the surface, with a hierarchically pore structure for fast transport of oxygen to the active sites.[222]

3. Outline

As mentioned in the motivation and further outlined in the literature background, the knowledge about carbonaceous materials is broad and gives already various tools to optimize the carbonaceous product. As explained in sections 2.3 and 2.4, especially members of the carbon nitride family recently gained a lot of attention, and the astonishing properties of C_3N_4 show that there is always more to discover. However, for the utilization of carbonaceous materials in industrial scale, still a better understanding and control over the condensation process is required. The aim of this thesis is to contribute to this understanding and give tools to control the condensation and thus to adjust the pore structure, surface, and bulk chemistry of the materials. Inspired by the concept of noble carbons and Nature, the condensation of nucleobases (xanthines) and ionic liquids will be discussed. Using these highly nitrogen-containing molecular precursors, no further post- or pre-treatment is needed, and the concept of “simple is better” is still satisfied. The pore structure of the materials will be controlled by salt melt templating, which offers a templating method without the use of any hazardous or toxic reagents. Furthermore, the salt can be reused. The obtained materials will be fully characterized, and the utilization for sorption applications, as heterogeneous catalysts, and as electrocatalyst will be discussed.

The synergetic effect of tuning the porosity and inserting large amounts of nitrogen into the carbonaceous materials is the overall topic in chapter 4. The condensation of guanine without a salt melt and the condensation temperature influences on the materials will be discussed in section 4.1. The discovery of structural pores, which are highly selective towards CO_2, will be described. Further tuning of the pore structure of the material by salt melt templating will be presented in section 4.2, showing the stability of the formed structural pores. Furthermore, the potential of the prepared materials as heterogeneous catalyst and their basic strength in dependence on the nitrogen content and pore morphology will be discussed. A similar approach will be used to explore the water sorption behavior of uric acid-derived materials, presented in

section 4.3. The use of carbon materials as water sorbents for heat transformation applications is not much explored, since carbon materials are rather hydrophobic. The introduction of large amounts of nitrogen and adjustment of the pore structure, hydrophilicity, and water uptake will be optimized and highly hydrophilic carbonaceous materials are obtained. Temperature dependence structural and compositional changes will be explored and discussed for all materials.

In section 5, the utilization of obtained NCs as support for metal nanoclusters will be presented. Due to the high thermal stability, porosity, and nitrogen content of ionic liquid noble carbon precursor derived NCs, a simple metal doping by impregnation and heat treatment can be achieved. The utilization of M-NCs as catalysts for ORR in dependency of the metal content and oxidation state will be discussed and compared with the performance of a commercial carbon/platinum 20% catalyst. With this, an example of the advantage of controlled condensation by the smart precursor choice and salt melt templating, for an industrial highly attractive application will be shown and provide an option to replace rare platinum with a simple synthesized, highly stable M-NC.

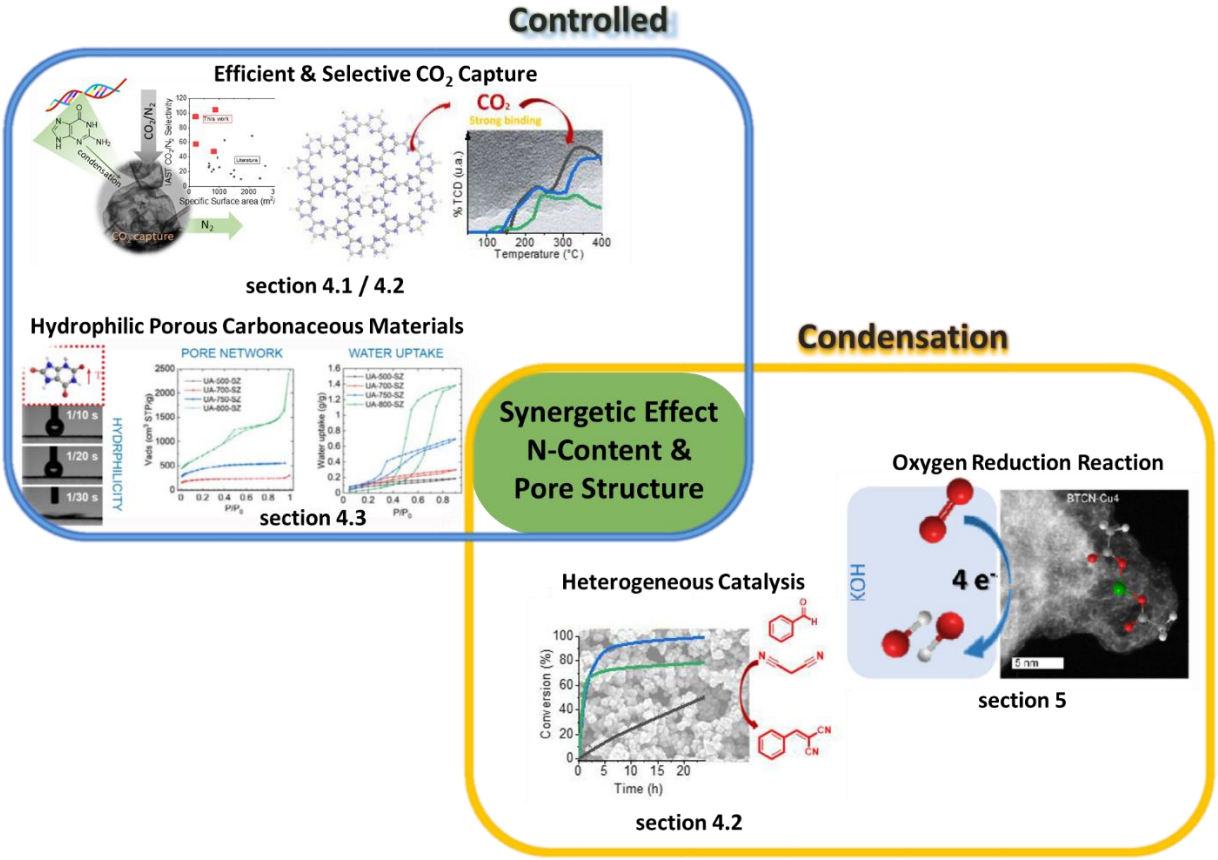

Figure 3-1. Graphical overview of the outline of this thesis.

4. Controlled Condensation of Nucleobases to N-Doped Carbonaceous Materials and Carbon Nitrides

As outlined in sections 2.3 and 2.4, many different nitrogen-containing precursors are known to obtain NCs and carbon nitrides, but at the same time the literature about the use of molecular precursors is rather rare. Besides the higher yield, by using defined macromolecules or polymers as precursors, the composition and structure of the final product might be more predictable. Solid-state synthesis, which includes pyrolysis, is for reasons also called *Black Box* synthesis.[223] It is little known about the reaction process during heat treatment and therefore the process is rather uncontrolled. In 2010 two interesting reports about the pyrolysis of ILs to carbonaceous materials with special properties, like high temperature resistance in air, appeared.[88] Followed by a report about the direct pyrolysis of adenine in 2015.[224] In 2018, Oschatz et al. published the concept of “Noble, Heteroatom-Doped Carbons”.[2] In short, they explain how carbonization of very stable precursors (i.e. HOMO level more positive than 1.3 V) lead to even more stable products. The bond formation within the process is limited to a number of even more stable motifs, which results in the formation of sp2-conjugated and layered materials. These very stable precursors are mostly high in heteroatom content, which is transferred to the final product. Noble carbons are outstanding in their stability against oxidation and have proven to be excellent electrocatalysts for ORR,[197, 225-227] electrodes for batteries,[224, 228-230] supercapacitors, and as support material for metals.[231-232] At this point, it is worth having a look into Nature. Nature chooses nucleobases to store the most important information. Therefore, these molecules must be very stable and they also contain a high amount of nitrogen (e.g. C/N ratio of guanine is 1), which makes them suitable precursors for noble carbons. Indeed, nucleobases from bacterial waste have shown to be good precursors without any further post- or pre-treatment.[227, 233-234]

Inspired by the concept of noble carbons and Nature´s choice, the condensation of guanine and uric acid was investigated intensively. Interestingly guanine is an oxidized pentamer of HCN with equimolar carbon and nitrogen content, which makes it a suitable, not toxic precursor for C_1N_1 materials.

4.1 Direct Condensation of Guanine to C_1N_1 Materials for Efficient and Selective Carbon Dioxide Capture[3]

As discussed in section 2.5.1.1 the selectivity and capacity of carbonaceous materials towards CO_2 sorption can be improved by nitrogen doping as well as by pore size adjustment. With NCs or carbon nitrides possessing chemical motifs complement to CO_2 and pores comparable to adsorbate size, the binding can be similar to the binding of a cryptand specific ion[235] resulting in a high selectivity and uptake. Pores fulfilling these requirements will be called cryptopores. Since these pores are ideally invisible for other gases, the analysis of those is challenging. However, the following will present C_1N_1 materials with an outstanding CO_2 selectivity and the characterization gives evidence for the presence of cryptopores.

Carbonaceous condensates with high nitrogen content have been synthesized by simple heat treatment of guanine in nitrogen atmosphere as shown in **Figure 4.1-1 A**. According to thermogravimetrical analysis (TGA) in nitrogen atmosphere (**Figure 4.1-1 B**) the first mass loss of guanine ends at around 500 °C and continues until 800 °C. To follow the product formation at different temperatures, samples were condensed at 500 °C, 600 °C, 700 °C, and 800 °C. TGA coupled to mass spectrometry (TGA-MS) (**Figure S 4.1-1**) of guanine shows water, CO_2, and

[3] Results of this section are adapted from the original work with permission of the authors:
J. Kossmann, D. Piankova, N.V. Tarakina, J. Heske, T.D. Kühne, J. Schmidt, M. Antonietti, N. López-Salas, Carbon, Guanine condensates as covalent materials and the concept of cryptopores, (2020), 172, 497-505.

ammonia as main leaving products. Samples will be named according to the condensation temperature in the following (i.e. cG@500 fur guanine condensed at 500 °C).

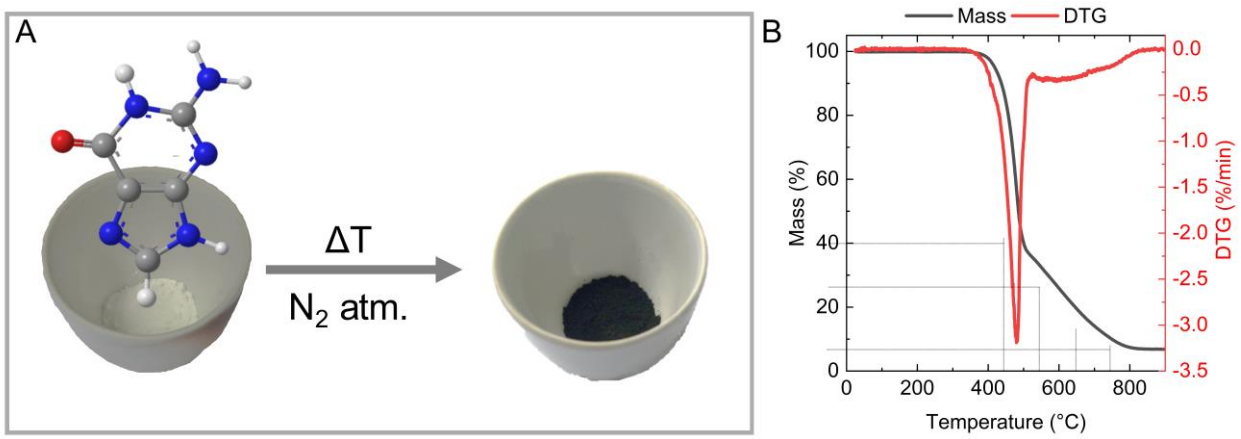

Figure 4.1-1. A) Visualization of the simple synthetic procedure followed in this section (i.e. heat treatment of guanine in nitrogen atmosphere). B) TGA and DTG in nitrogen atmosphere of guanine. Dashed lines show the temperatures used during the heat treatment in this section.

Yields after condensation (**Table 4.1-1**) are in line with the expected yields from TGA and decrease from 54 wt% for cG@500 to 10 wt% for cG@800. **Table 4.1-1** also shows the composition according to energy dispersive X-ray analysis (EDX) and elemental analysis (EA) in at%. The unexpected high oxygen content can be ascribed to adsorbed water or CO_2 to the material. Here it is to mention that the different measurement conditions can influence the results and thereby explain the significant difference in oxygen contents. While EDX measurements take place under high vacuum, EA measurements are performed under ambient air conditions and therefore the oxygen content might be higher with EA results. Samples condensed at 500 °C, 600 °C, and 700 °C exhibits around 45 at% nitrogen and 53 at% carbon, resulting in a C/N ratio of 1.2. Nitrogen content only decreases to 26 at% when increasing the temperature to 800 °C, resulting in a C/N ratio of 2.8. This shows the formation of C_1N_1 condensates from guanine, which are stable until 700 °C and starts to decompose at higher temperatures to C_2N- or C_3N- like

materials. This thermal behavior goes well along with the thermal behavior reported for CTFs[236-237] and with the thermal limits reported for C_2N compounds.[104, 238-239]

Table 4.1-1. Yield of condensation in wt%, composition according to EDX and EA analysis in at%.

Sample	Yield [wt%]	EDX/EA composition [at%]				
		C [a]	N [a]	O [a]	H [a,b]	C/N [c]
cG@500	54	53.6(4)/ 48.1(3)	45.5(4)/ 40.9(2)	0.9(1)/ 4.3(0)	25.2(0)	1.2(0.1)/ 1.2 (0.1)
cG@600	29	51.9(2)/ 44.7(3)	42.1(3)/ 30.0(0)	6.0(2)/ 6.2(1)	19.1(2)	1.2(0.1)/ 1.5(0.1)
cG@700	23	54.5(2)/ 59.8(2)	41.8(1)/ 28.9(1)	3.7(1)/ 5.1(1)	16.1(3)	1.3(0.1)/ 1.6(0.1)
cG@800	10	71.8(4)/ 57.5(3)	26.0(4)/ 20.7(2)	2.2(0)/ 3.5(3)	18.3(2)	2.8(0.0)/ 2.8(0.3)

[a] Standard deviation values are given in brackets; [b] Obtained only by EA; [c] Propagation of error is given in brackets;

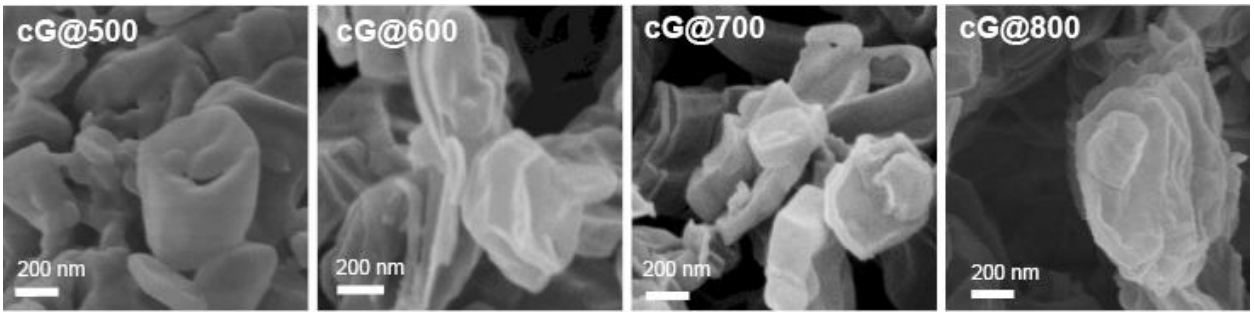

Figure 4.1-2. SEM micrographs of guanine condensed at different temperatures (cG@500, cG@600, cG@700, and cG@800) with a scale bar of 200 nm showing particles of ca. 1 µm for all condensates.

Scanning electron microscope (SEM) micrographs in **Figure 4.1-2** show particles of around 1 µm for all condensates. SEM-EDX (**Figure S 4.1-2**) and EDX coupled to scanning transmission electron microscope (STEM-EDX) (**Figure S 4.1-3**) mapping confirm that carbon and nitrogen are homogeneously distributed through the material.

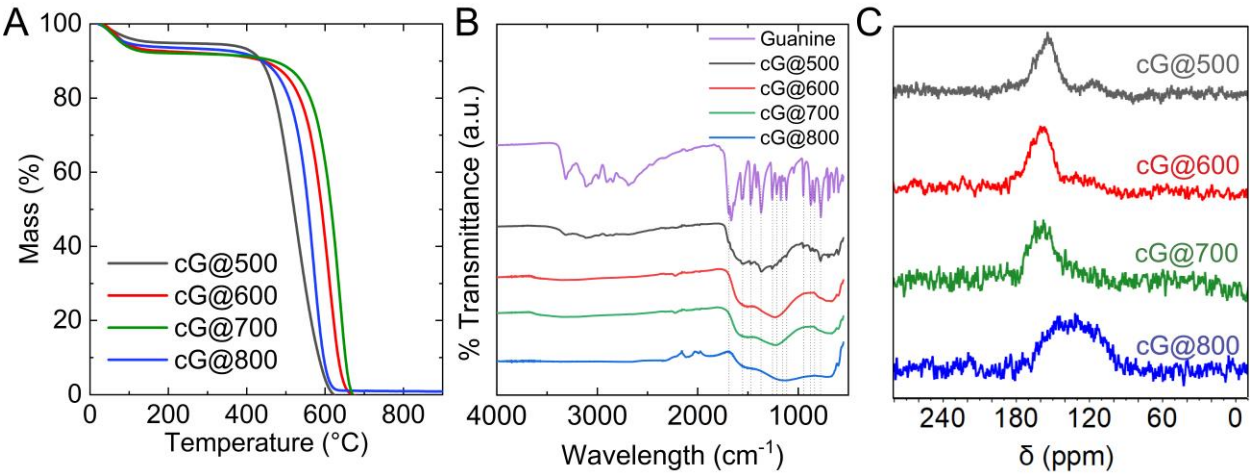

Figure 4.1-3. A) TGA in synthetic air, B) FTIR spectra, and C) solid-state NMR of guanine condensed at different temperatures.

The TGA curves of the materials in synthetic air atmosphere (**Figure 4.1-3 A**) show a first mass loss at ca. 100 °C, which can be ascribed to adsorbed water. All materials are stable until ca. 500 °C with a slight increase in stability from cG@500 to cG@700 followed by a decrease to cG@800. Further confirming the stability of C_1N_1 materials up to 700 °C.

Fourier-transform infrared spectroscopy (FTIR) and solid-state nuclear magnetic resonance (ssNMR) results further show an incomplete condensation of cG@500. FTIR spectra of cG@500 (**Figure 4.1-3 B**) exhibits subtle peaks which are related to guanine and ssNMR spectra (**Figure 4.1-3 C**) shows two peaks in positions similar to those of guanine. FTIR spectra of cG@600 and cG@700 present broad peaks centered at 1600 cm^{-1} and 1250 cm^{-1} which can be ascribed to CN/C=C conjugated structures and ssNMR peaks broaden compared to cG@500. cG@800 shows in both measurements significant differences compared to the lower temperature derived materials. FTIR peaks, as well as ssNMR peak, broaden, and ssNMR peak additionally shifted to lower δ. In summary, spectroscopic measurements confirm the formation of three different materials. With a condensation temperature of 500 °C, a not fully condensed polyguanine

is formed which further condense at 600 °C to a C_1N_1 material which is stable until 700 °C and decompose at 800 °C to a highly nitrogen-doped carbon.

Powder X-ray diffraction (PXRD) spectra (**Figure S 4.1-4**) show that all samples are amorphous with a broad main peak at 26.5° from graphitic stacking and a weak broad peak at 42°. Peak intensity decreases with increasing condensation temperature, indicating a partly de-stacking of the layers. cG@500 additionally shows a peak at 14°, which is characteristic for NCs with in-plane porosity like C_3N_4.[240] X-ray photoelectron spectroscopy (XPS) (**Figure 4.1-4**) nicely confirms previous observations. Deconvolution of the C1s spectra of cG@500 shows C-N/C-O bonds prevail over C=C bonds and for cG@800 the pure carbon connections increase significantly, confirming the rupture of the C_1N_1 network above 700 °C. Deconvolution of the N1s spectra shows the presence of electron-rich (397 eV) and electron-poor (399 eV) nitrogen functionalities. The ratio of quaternary-N and pyridinic-N remains the same through all samples.

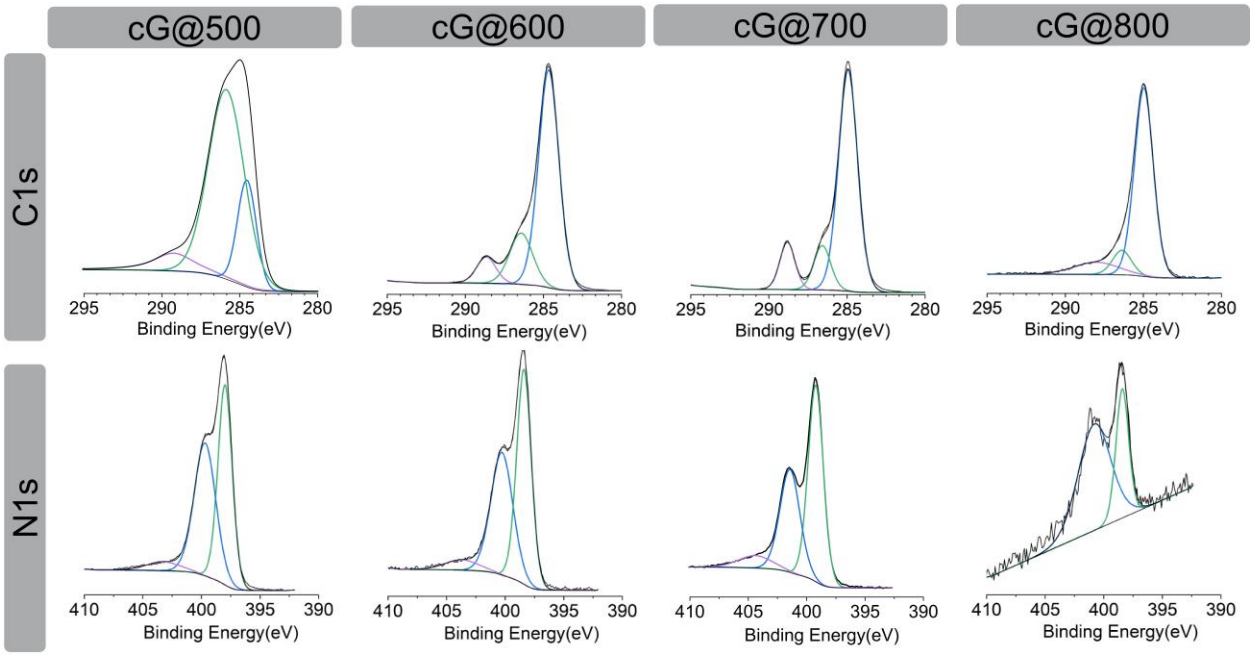

Figure 4.1-4. Upper panel C1s and down panel N1s XPS spectra and deconvolution of cG@500, cG@600, cG@700, and cG@800.

Further investigations of the sub-micrometer structure of C_1N_1 materials have been performed by electron microscopy investigations. Secondary electron scanning electron microscopy (SE-STEM) and high-angular annular-dark field scanning electron microscopy (HAADF-STEM) images in **Figure 4.1-5** show that particles are partly hollow with a more dense shell and a less dense inner part with voids. The thickness of the shell decreases with increasing temperature and the inner part becomes more uniform with voids of a few tens of nanometer (see also **Figure S 4.1-5**). The last row of **Figure 4.1-5** shows high-resolution transmission electron microscopy (HRTEM) images of the samples with fast Fourier transforms (FFT). Images show the amorphous structure of the materials with an increased nanoscale structural order. At 500 °C the FFT ring is broad and diffuse indicating no local order. With increasing the temperature to 600 °C the FFT ring gets more defined showing samples fringes with a length of about 10 Å, presumably isolated planes of carbon/nitride layers. Increasing the temperature further to 700 °C the FFT ring is more pronounced at q ca. 2.74 nm^{-1}, corresponding to a d-spacing of ca. 0.37 nm (see also **Figure S 4.1-6**). Electron energy loss spectroscopy (EELS) of C_1N_1 materials (**Figure S 4.1-7**) shows sharp C and N K-edge peaks. C K-edge at 290 eV and 300 eV can be ascribed to 1s-π* and 1s-σ* electronic transition of sp2 hybridized carbon with a shoulder at 320 eV which can be ascribed to C-N bonds. N K-edges at 400 eV and 410 eV indicate the participation of nitrogen atoms in a sp2-hybridized network.

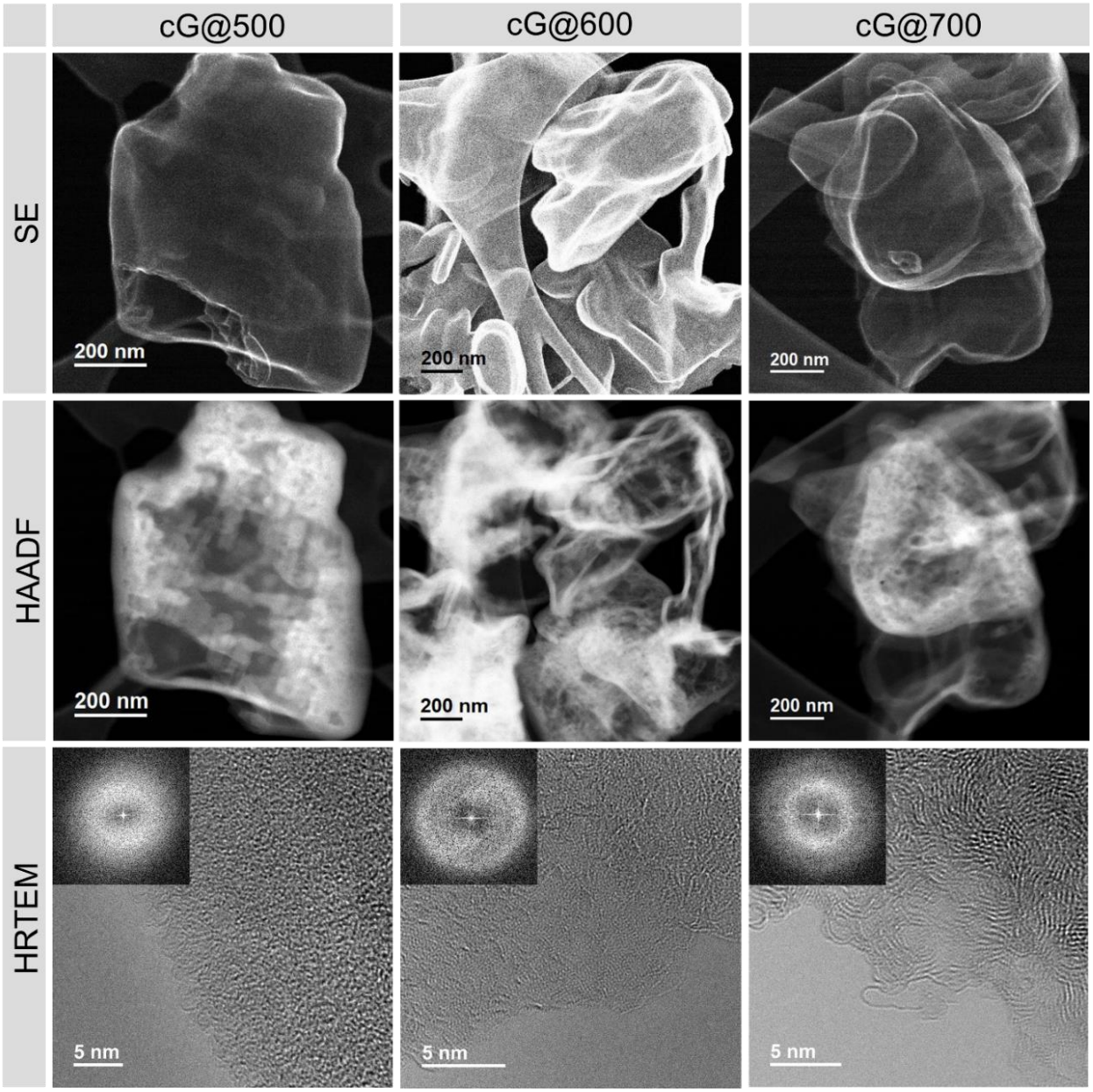

Figure 4.1-5. SE-STEM images (upper row) and corresponding HAADF-STEM (second row) images of cG@500, cG@600, and cG@700 showing the morphology and the internal structure. HRTEM images (down row) with FFT transforms as inlet.

Surface area analysis has been performed by nitrogen adsorption/desorption isotherms at 77 K. **Figure 4.1-6 A** presents the isotherms measured. cG@500 does not show any nitrogen uptake, indicating that the incompletely condensed polyguanine did not develop porosity. On the contrary, cG@600, cG@700, and cG@800 show type IV isotherms with a significant nitrogen uptake already at low relative pressures and a strong hysteresis, typical for micro- and mesoporous materials. Indeed, surface area according to BET model of cG@600 and cG@700 is around 200 $m^2\ g^{-1}$ and decreases slightly with higher condensation temperature to 160 $m^2\ g^{-1}$ for cG@800 (see **Table 4.1-2**). CO_2 adsorption isotherms in **Figure 4.1-6 B** shows surprising results. On the one hand, cG@500 shows a considerable high CO_2 uptake of 0.9 mmol g^{-1} compared to zero surface area measured by nitrogen sorption. On the other hand, the difference of cG@600 and cG@700 to cG@800: While the C_1N_1 materials cG@600 and cG@700 have a high CO_2 uptake of 2.7 mmol g^{-1} and 2.8 mmol g^{-1} respectively the CO_2 uptake decrease to 1.5 mmol g^{-1} for cG@800 (**Table 4.1-2**).

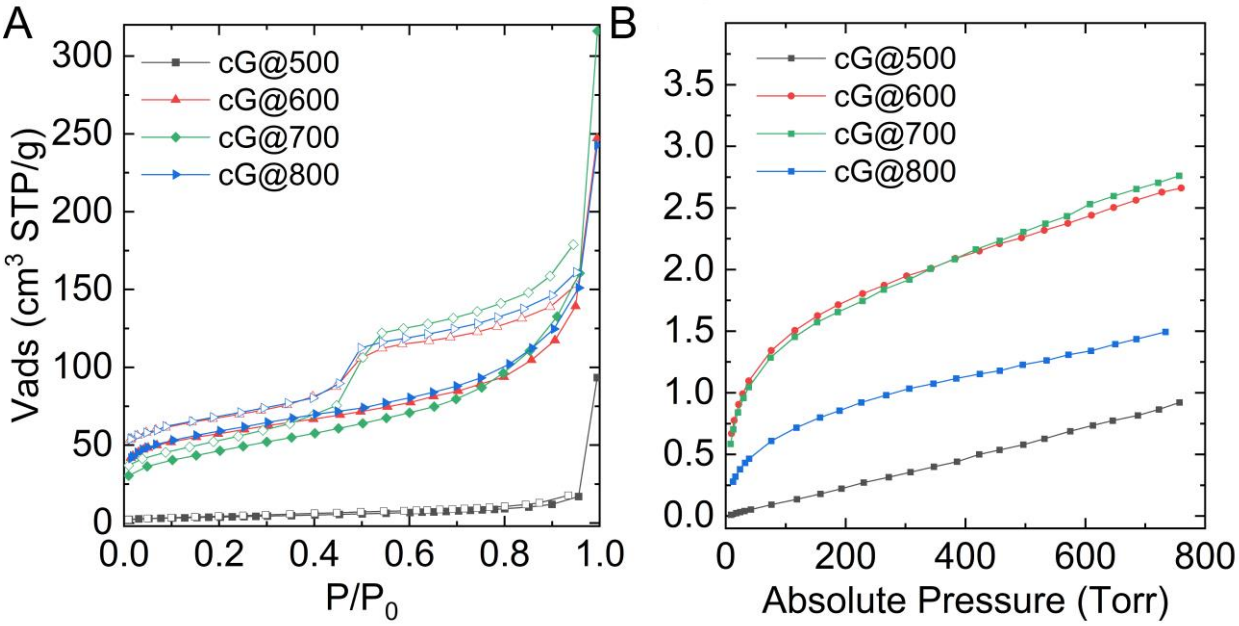

Figure 4.1-6. A) Nitrogen adsorption (filled symbols) and desorption (empty symbols) isotherms at 77 K and B) CO_2 adsorption isotherms at 273 K of guanine condensed at different temperatures.

Table 4.1-2. Sorption characteristics of guanine condensates at different temperatures: Specific surface area (SSA) obtained by applying the BET model and total pore volume (V_T) extracted from nitrogen adsorption isotherms. Maximum CO_2 uptake from CO_2 adsorption isotherms at 273 K.

Sample	SSA [a] [m^2 g^{-1}]	V_T [b] [cm^3 g^{-1}]	max. CO_2 uptake [mmol g^{-1}]
cG@500	13	0.03	0.9
cG@600	208	0.22	2.7
cG@700	212	0.23	2.8
cG@800	163	0.25	1.5

[a] Obtained using QSDFT method applied to N_2 adsorption isotherm at 77 K. [b] at p/p_0 = 0.96 for pores with a diameter smaller than 60 nm.

These results already point to the high affinity of C_1N_1 materials to CO_2. To further understand the CO_2 adsorption of C_1N_1 materials, isotherms at 298 K are measured and the IAST of the materials is calculated. **Figure 4.1-7 A** and **B** present the results and, indeed the materials show a very high $IAST_{CO2/N2}$ selectivity when compared to other porous carbonaceous materials. As illustrated in **Figure 4.1-7 C** the values of 97 and 66 for cG@600 and cG@700 respectively are above most carbonaceous materials, even with a comparable low surface area according to BET model.[144, 241] Other carbonaceous materials with a comparable selectivity are SNS[242] and CIN[243] materials (see **Table S 4.1-1**). However, all the reported carbonaceous materials show a lower heat of adsorption, and the CO_2 sorption is ascribed to adsorption in the micropores of carbonaceous materials. Other types of materials, which are reported as CO_2 sorbents with high selectivity are polymeric triazine networks like PCBZL[244] and CIN.[243] Even though the $IAST_{CO2/N2}$ value of those (148 for PCBZL and 100 for CIN) are very tempting, the synthetic procedure to obtain the materials includes many synthetic steps and harmful reagents (i.e. cyanuric trichloride for PCBLZ).

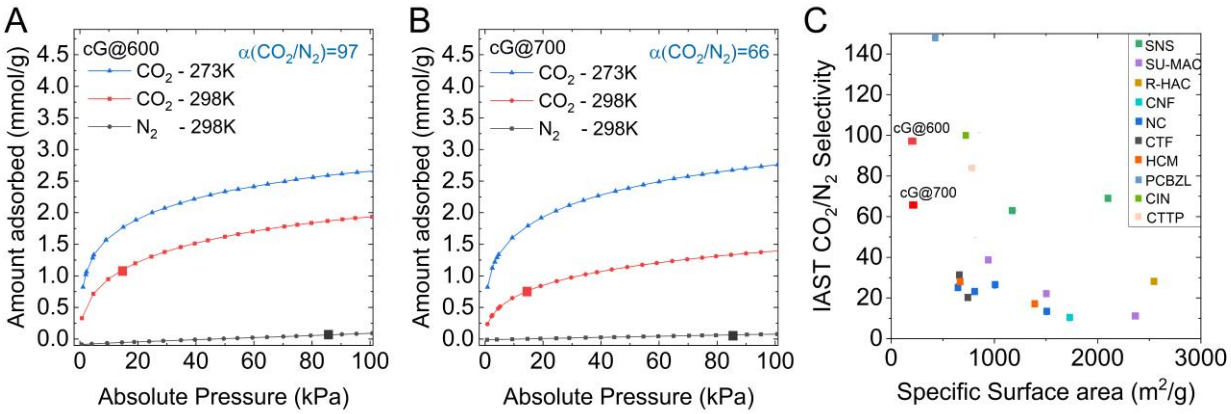

Figure 4.1-7. $IAST_{CO2/N2}$ of A) cG@600 and B) cG@700 with CO_2 adsorption isotherms at 273 K, and 298 K and N_2 adsorption isotherm at 298 K. C) Specific surface area vs. $IAST_{CO2/N2}$ of some reported carbonaceous materials.

The specific heat of adsorption (Q_{st}) of 51 kJ mol^{-1} and 59 kJ mol^{-1} is beyond the typical values for physisorption of CO_2 (see **Figure S 4.1-8** and **Table 4.1-1**) further confirming the strong affinity of CO_2 to C_1N_1 materials. Temperature programmed desorption of CO_2 (CO_2-TPD) further helps to understand the binding of CO_2 to the materials. The TCD signal of cG@500 in **Figure 4.1-8** shows only one peak at ca. 150 °C, which is in the range of desorption of physisorbed CO_2.[245] cG@600 and cG@700 show two desorption peaks at 210 °C and 240 °C which are out of the range of physisorbed CO_2, proving a binding through sites with strong binding energy. cG@800 shows also two desorption peaks but the first at 175 °C and the second at 250 °C confirming the regional decomposition of the C_1N_1 structure when the condensation temperature is raised above 700 °C.

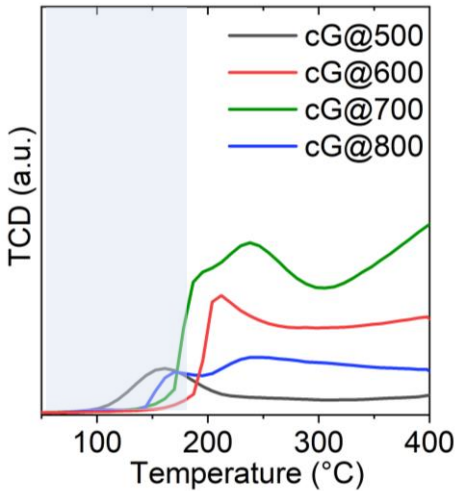

Figure 4.1-8. CO_2 TPD of guanine condensed at different temperatures. Blue background should visualize the temperature range of desorption of physisorbed CO_2.

To further understand these new materials, Kühne et al. performed dynamic simulated annealing using the second-generation Car-Parrinello approach of Kühne et al.[246] as implemented in the CP2K suite programs.[247] They found CO_2 molecules to be oriented orthogonally with respect to the plane of C_1N_1 layers in every second structural pore in every layer as shown in **Figure 4.1-9.** The theoretical energy of adsorption of CO_2 is calculated to be -31 kJ mol^{-1}. This value is below the experimental one presented before. Most likely, this can be explained by a consequence of the perfect AAA stacking in the simulations, which is not present in the synthesized material. This mismatch was already observed for C_2N materials, which have lower energy of adsorption than the new C_1N_1 materials.[143, 248]

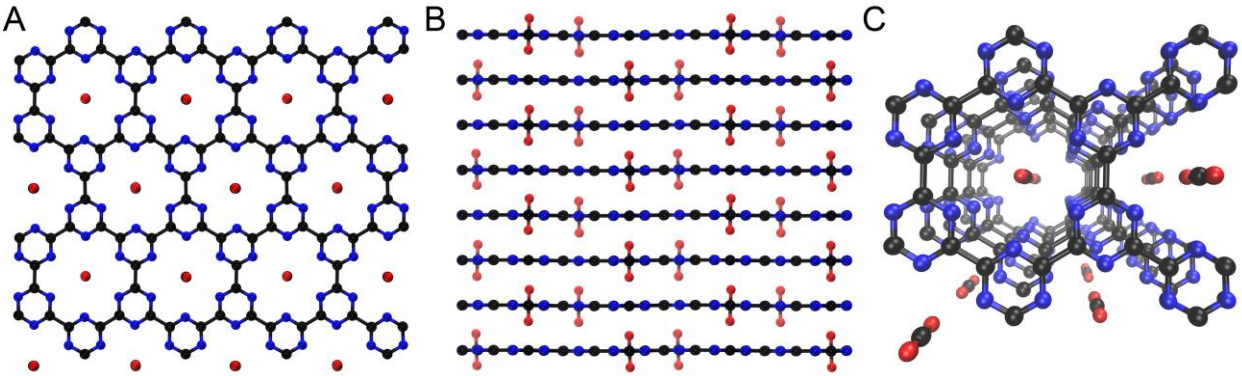

Figure 4.1-9. A) Lowest energy structure of CO_2 molecules adsorbed in a layer of bulk C_1N_1 (black: carbon, blue: nitrogen, red: CO_2). B) Side view of a stack of C_1N_1 layers (only two layers are visible in this cross-section) with CO_2 molecules, C) stereoscopic top view of the CO_2-filled C_1N_1 structure.

In this section, the condensation of guanine at temperatures from 500 °C to 800 °C is presented. Condensation at 500 °C leads to not fully condensed polyguanine without porosity, as shown by FTIR, ssNMR, and nitrogen sorption isotherms. Increasing the condensation temperature to 600 °C, C_1N_1 materials with high stability towards oxidation in air, low surface area but unprecedented CO_2 uptake, as shown by TGA, EA, EDX, and nitrogen and CO_2 adsorption isotherms. Further investigations on the C_1N_1 materials show an outstanding high $IAST_{CO2/N2}$ selectivity up to 100. This, together with high CO_2 heat of adsorption values indicated that the CO_2 sorption process is closer to a highly selective chemisorption than simple physisorption but still reversible under practical conditions. The high CO_2 uptake together with low nitrogen uptake by adsorption, gives evidence for the presence of CO_2 selective cryptopores, as described at the beginning of the section. When heat treating guanine at 800 °C, the C_1N_1 framework is not stable anymore and starts to decompose, resulting in a highly nitrogen-doped carbonaceous material.

4.2 Introduction of Surface Area to Guanine Condensates by Salt Melt Templating and the Potential in Heterogeneous Basic Catalysis[4]

After discovering the simple synthesis of highly valuable and interesting C_1N_1 materials, further development on the materials was investigated. The high CO_2 sorption of the materials gives evidence to assume basic sites being present in the materials and therefore they could be interesting as basic heterogeneous catalysts. However, as described in the introduction, the porosity and surface area of carbonaceous materials as heterogeneous catalyst is very important for the performance of the materials. For the simple reason, that the reacting species must be able to reach the active sides on the material and the more active sides are available, the higher conversion can be achieved.

In the following, the introduction of surface area to guanine condensates with salt melt templating will be presented. Subsequent the potential of the materials as basic heterogeneous catalysts will be shown with the Knoevenagel condensation reaction as a model reaction. Salt melt templating was chosen as the templating method due to the simple and low-cost synthesis without the use of any toxic reagents. Guanine was condensed at different temperatures and with different guanine to salt melt ratios to understand the influence of temperature and dilution to the final product and to further understand the formation of the materials.

The synthetic procedure, sown in **Figure 4.2-1**, is as simple as mixing guanine, NaCl, and $ZnCl_2$ with a pestle and mortar, let it undergo a heat treatment in nitrogen atmosphere, and wash it after cooling down to ambient temperatures. The salt mix of NaCl and $ZnCl_2$ will be called SZ hereafter and the different ratios used will be implemented in the name as a 1, 6, or 10 for a 1:0.5:0.5, 1:3:3, or 1:5:5 ratio of guanine:$ZnCl_2$:NaCl respectively. Therefore, the names will be like cG@500-SZ10

[4] Results of this section are adapted from the original work with permission of the authors:
J. Kossmann, T. Heil, M. Antonietti, N. López-Salas, ChemSusChem, Guanine Derived Porous Carbonaceous Materials: towards C1N1, (2020), 13, 6643.

for 1 g of guanine heat-treated at 500 °C with SZ containing 5 g of NaCl and 5 g of $ZnCl_2$. All names with synthetic details and yields are also listed in **Table S 4.2-1**. After condensation, samples are washed two times with 1M HCl and one time with distilled water to remove the salts. However, after intense washing, some zinc traces can not be removed.

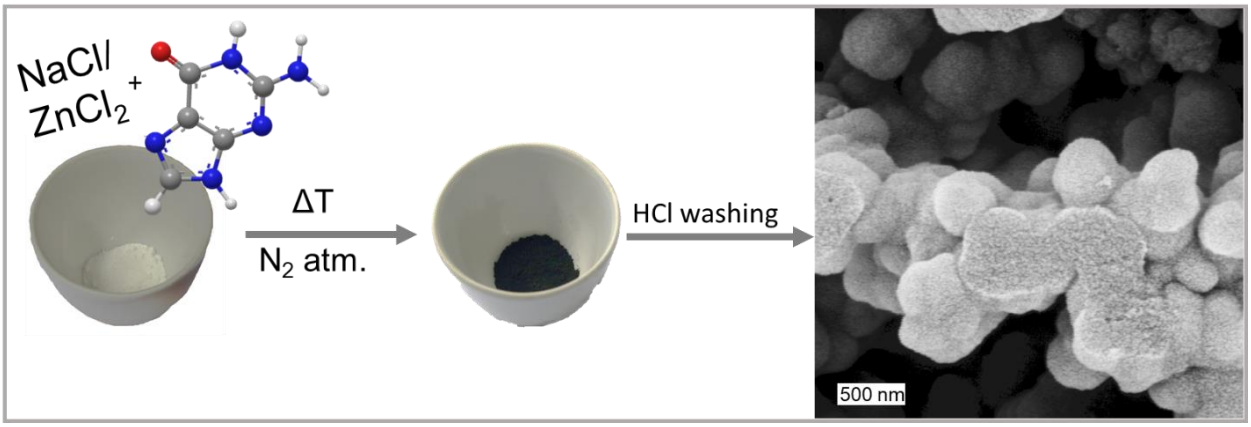

Figure 4.2-1. Schematic illustration of the synthetic procedure followed in this section to obtain porous guanine condensates via salt melt templating.

The composition of the materials was analyzed with EDX and EA analysis, like the materials obtained without salt melt in the previous section. Results are presented in **Table 4.2-1**. The higher oxygen content obtained by EA can again be ascribed to the different analysis conditions. Furthermore, the overall oxygen content is assumed to be from absorbed water on the material. Materials obtained at temperatures from 500 °C to 700 °C show a C_1N_1 composition and with increasing the temperature to 800 °C the C_1N_1 framework decomposes to an NC with a C/N ratio of ca. 7. This trend was already observed for guanine condensates obtained without salt melt templating, confirming the stability of the C_1N_1 structure build from the condensation of guanine at temperatures up to 700 °C. The composition of cG@500-SZ is not influenced by the amount of salt used in the synthesis, whereas at 800 °C the amount of salt strongly influences the nitrogen content of the material (**Table 4.2-1**). With increasing the amount of salt, nitrogen content decreases, and carbon content increases, resulting in a C/N ratio of 3.7 for cG@800-SZ1, 6.1 for cG@800-SZ6, and 7.4 for cG@800-SZ10. Here it is worth to mention, that the sample with the

lowest amount of salts (cG@800-SZ1) has a similar C/N ratio to that of cG@800. SEM-EDX mapping (**Figure S 4.2-1**) shows that carbon and nitrogen are homogeneously distributed over the material.

Carbon yields of the materials decrease with increasing temperatures. Interestingly at 500 °C the amount of salt used does not influence the yield, whereas at 800 °C the yield is increasing with an increasing amount of salt melt (**Table S 4.2-1**). At 800 °C, the C_1N_1 framework is disrupted and interactions of the salt mixture with the reaction phase are stabilizing the leaving groups as reported before.

Table 4.2-1. Yield after condensation and summary of the composition data obtained by EDX and EA analysis.

Sample	Yield	EDX / EA [wt%]				
	[wt%]	C	N	O	H[a]	C/N
cG@500-SZ1	61	41.8/ 40.5	49.1/ 40.2	4.8/ 11.7	2.8	0.9/ 1.0
cG@500-SZ6	64	44.5/ 38.5	42.3/ 37.5	3.6/ 14.7	3.0	1.1/ 1.0
cG@500-SZ10	61	47.7/ 38.0	43.0/ 35.0	3.4/ 14.9	1.6	1.1/ 1.1
cG@600-SZ10	42	51.7/ 38.0	41.0/ 34.0	7.2/ 17.0	3.0	1.3/ 1.1
cG@700-SZ10	33	46.6	42.4	4.4	-	1.1
cG@800-SZ1	16	71.4	19.4	3.1	-	3.7
cG@800-SZ6	20	78.7	12.9	5.7	-	6.1
cG@800-SZ10	22	81.2/ 72.0	11.0/ 12.0	6.7/ 10.8	1.0	7.4/ 6.5

[a] Only by EA

TGA in synthetic air shows that all materials are stable up to ca. 400 °C with a slight increased stability for cG@800-SZ10 (see **Figure 4.2-2 A**). The suggestion of the high amount of oxygen present in the samples caused by water adsorbed is confirmed by TGA without prior degassing (**Figure S 4.2-2 A**). Without degassing, samples show a mass loss of ca. 15 % at 100 °C and with degassing before TGA the mass lass at 100°C decreases dramatically to less than 5 %. TGA of guanine condensed at 500 °C and 800 °C with increasing salt content (**Figure S 4.2-2 B** and **C**) show a slightly decreased stability with increasing salt content and an increased mass loss at 100 °C.

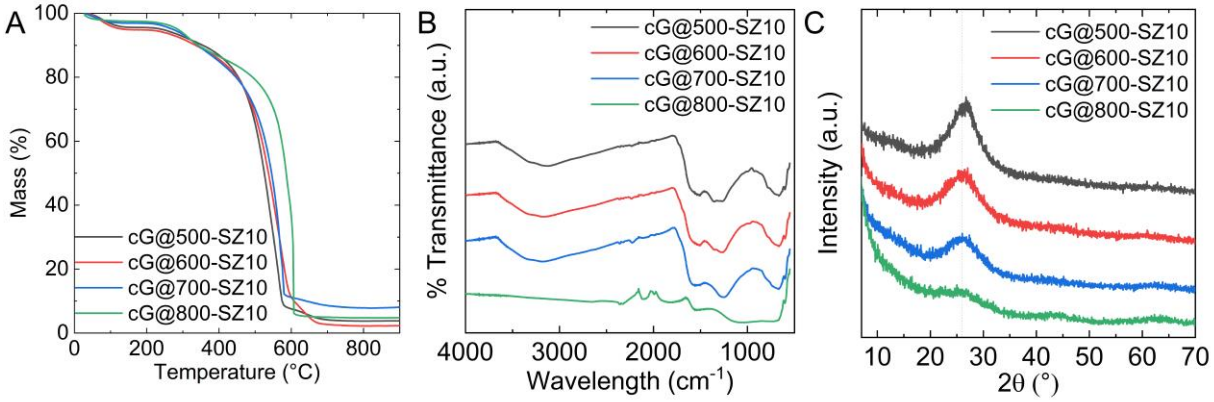

Figure 4.2-2. A) TGA analysis in synthetic air, B) FTIR spectra, and C) PXRD pattern of cG@500-SZ10, cG@600-SZ10, cG@700-SZ10, and cG@800-SZ10. All were measured after 20 hours of degassing at 150 °C under high vacuum.

XPS analysis and deconvolution of cG@500-SZ10, cG@700-SZ10, and cG@800-SZ10 show C1s and N1s (**Figure 4.2-3**) peaks for all materials. Deconvolution of the C1s peak shows the presence of C=C, C-N, and C=O peaks at 284.7 eV, 286.1 eV, and 286.5 eV respectively. While the ratio between the peaks stays approximately the same for cG@500-SZ10 and cG@700-SZ10, the ratio between C=C and C-N increases for cG@800-SZ10. This result goes well along with the increased carbon and decreased nitrogen content for this material, as observed by EDX and EA. N1s spectra can be separated into four peaks: 398.2 - N-pyridinic, 399.7 – N-pyrrolic, 400.5 – N-quarternary, and 405 eV – N-oxide. Also here cG@500-SZ10 and

cG@700-SZ10 peaks look very similar and just for cG@800-SZ10, an increase of the electron-poor signals can be observed.

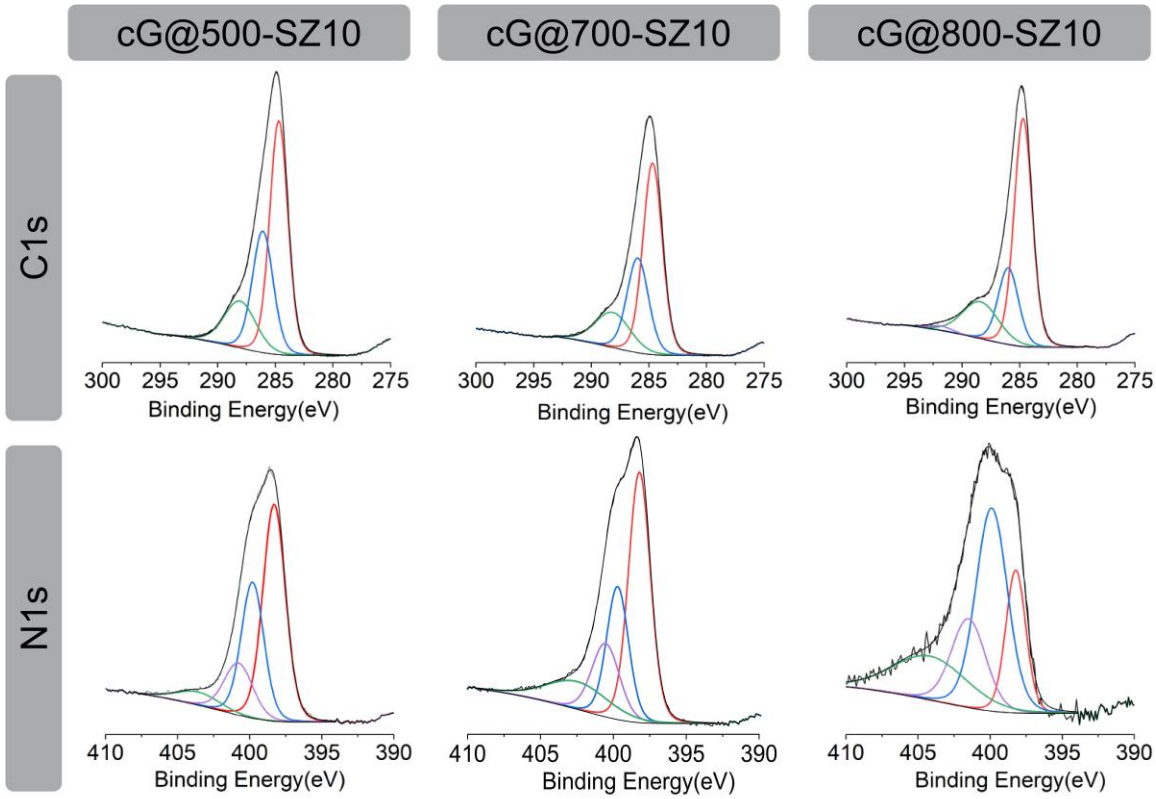

Figure 4.2-3. Deconvoluted C1s and N1s XPS spectra of cG@500-SZ10, cG@700-SZ10, and cG@800-SZ10.

FTIR spectra of the materials **(Figure 4.2-2 B**) are very similar to those of guanine samples without salt melt, shown in the section 4.1. The main difference can be seen in the spectra of the sample condensed at 500 °C. Without salt melt, substile peaks from guanine were observed, indicating the incomplete condensation of guanine, which cannot be seen anymore. With the salt melt, guanine is already fully condensed at 500 °C. The broad peak from 1200 cm^{-1} to 1600 cm^{-1} can be ascribed to the stretching mode of CN heterocycles and the broad band from 2800 cm^{-1} to 3700 cm^{-1} to water deformation. cG@800-SZ10 does not show clear peaks anymore, probably due to the disruption of the C_1N_1 framework. PXRD pattern of the materials in **Figure 4.2-2 C** show that all samples are amorphous materials. The slight decrease of the peak at 26.5° with

increasing temperature indicates the growing amorphous content of the materials with almost no peak for cG800-SZ10 anymore.

SEM micrographs in **Figure 4.2-4** show the expected formation of a xerogel-like network, build up by primary particles with a diameter of ca. 300-1000 nm for all materials. SEM micrographs of samples with an increasing amount of salt melt in the reaction mixture (**Figure S 4.2-3**) show nicely the development of the xerogel-like network. At both temperatures, the lowest salt melt content (guanine to SZ ratio 1:1) is not sufficient to develop colloids and with increasing salt melt content small colloids are formed, which grow with increasing salt content. TEM images show the pore development with increasing temperature. From a not porous primary condensate build at 500 °C to a more defined porous carbonaceous material up to 700 °C. When increasing the temperature further to 800 °C, C_1N_1 is not thermodynamic stable anymore and the disrupted, more stable NC develops. This goes along with shrinking of the particles.

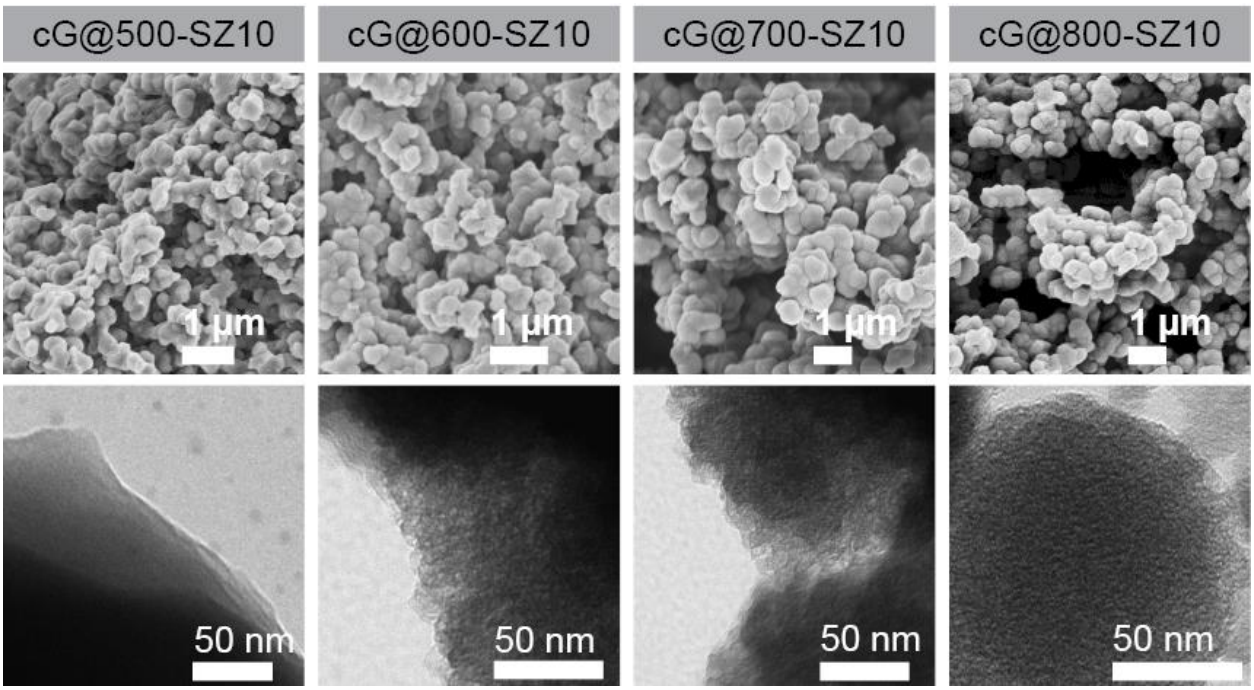

Figure 4.2-4. Upper row: SEM micrographs and down row: TEM micrographs of cG@500-SZ10, cG@600-SZ10, cG@700-SZ10, and cG@800-SZ10.

Pore structure analysis has been performed by nitrogen adsorption/desorption analysis at 77 K. **Figure 4.2-5 A** shows the isotherms (adsorption with filled and desorption with empty symbols) and **Table 4.2-2** presents to resulting surface area according to the BET model and the total pore volume. cG@500-SZ10 shows almost no nitrogen adsorption due to a very limited accessible surface area for nitrogen as it was observed for the sample synthesized without salt melt. This shows that, despite the complete condensation observed with spectroscopic analysis before, the condensation temperature of 500 °C is not sufficient for the material to develop completely and oligomers from precipitation of guanine developed. With increasing temperature, cG@600-SZ10 and cG@700-SZ10 show almost identical type I isotherms indicating microporous materials with a specific BET surface area of 852 $m^2\ g^{-1}$ (calculated with the BET-model). cG@800-SZ10 has a larger nitrogen uptake at very low pressures, indicating a larger micropore volume. Additionally, the presence of mesopores can be seen from the isotherm by an increasing uptake at moderate relative pressure and a small hysteresis. The rupture of the C_1N_1 structure and the vapor pressure of $ZnCl_2$ present in the synthesis can explain the development of a higher micropore volume and mesopores (T_b of $ZnCl_2$: 732 °C). By this, a surface area as high as 1982 $m^2\ g^{-1}$ developed. Nitrogen sorption of cG@800-SZ1 and cG@800-SZ6 (see **Figure S 4.2-4 B**) confirms this. With less salt melt present during the condensation (cG@800-SZ1) the isotherm is more similar to that of cG@700-SZ10 with slightly developed mesopores and with increasing salt melt content the surface area of the material increases.

Pore size analysis of cG@700-SZ10 and cG@800-SZ10 has been done by argon physisorption at 87 K, shown in **Figure S 4.2-5**. Both samples show a narrow PSD in the micropore range with pores of a diameter of 1.3 nm and 1.7 nm respectively and cG@800-SZ10 shows additional mesopores with a diameter of ca. 3.6 nm and 6.6 nm.

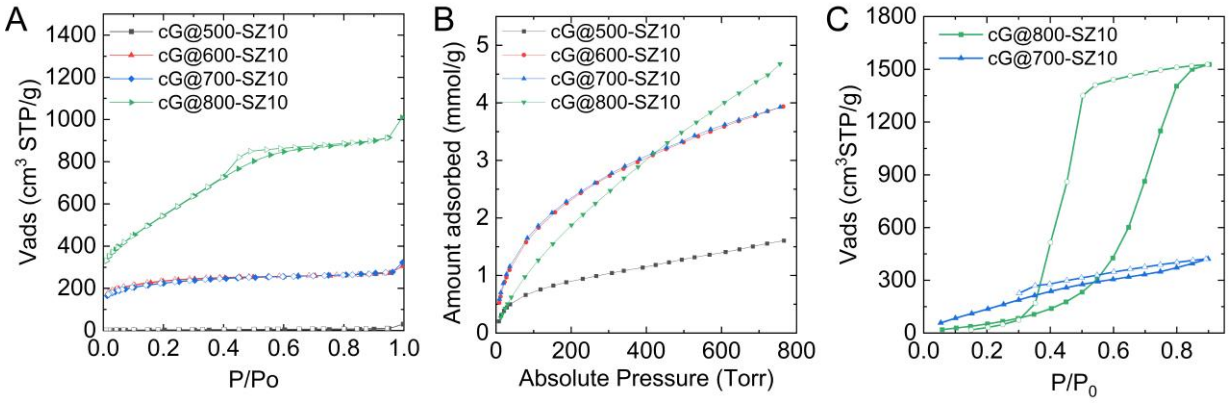

Figure 4.2-5. A) Nitrogen adsorption (filled symbols)/desorption (empty symbols) isotherms at 77 K, B) CO_2 adsorption isotherms at 298 K of cG@500-SZ10, cG@600-SZ10, cG@700-SZ10, and cG@800-SZ10. C) Water vapor isotherms at 298 K of cG@700-SZ10 and cG@800-SZ10.

Table 4.2-2. Data extracted from physisorption analyses. Specific surface area (SSA) obtained by applying BET model and total pore volume (V_T) from nitrogen adsorption isotherms at 77 K and max. CO_2 uptake from CO_2 adsorption at 273 K.

Sample	SSA[a] [m^2g^{-1}]	V_T [b] [cm^3g^{-1}]	max. CO_2 uptake [mmol g^{-1}]
cG@500-SZ10	8	-	1.5
cG@600-SZ10	852	0.41 (0.42)	4.0
cG@700-SZ10	812	0.38 (0.43)	4.0
cG@800-SZ10	1982	1.40 (1.42)	4.7

[a] Obtained by applying the BET method to N_2 adsorption isotherms at 77K; [b] Calculated by DFT, in brackets the result obtained at P/P0=0.95.

CO_2 adsorption isotherm of cG@500-SZ10 (**Figure 4.2-5 B**) shows a remarkable high CO_2 uptake of 1.5 mmol g^{-1} when considering the low nitrogen uptake. Indicating again specific active sites that are not available for nitrogen but for CO_2. The situation is similar for cG@600-SZ10 and cG@700-SZ10. The isotherms are, like the nitrogen isotherms, almost similar and show an uptake of 4 mmol g^{-1} at high relative pressures. The $IAST_{CO2/N2}$ of cG@600-SZ10 and cG@700-SZ10 is 100 and 51 respectively (see **Figure S 4.2-6**). Which is in the same range as for the samples synthesized without salt melt templating (i.e. 97 and 66 respectively), but with a higher CO_2 uptake

(i.e. for cG@600 and cG@700: 2.7 mmol g^{-1}). The significant concave shape at low relative pressures indicates again a strong binding of CO_2. These results proof, that the C_1N_1 structure with CO_2-specific cryptopores is kept even with salt melt templating, further verify the stability of this structure. The CO_2 sorption of cG@800-SZ10 is in line with the previous results. The rupture of the C_1N_1 structure causes the rupture of the CO_2-specific cryptopores. Also, the concave shape of the isotherm is not that strong anymore. However, the CO_2 uptake at high relative pressure is slightly larger than for the C_1N_1 materials (i.e. 4.7 mmol g^{-1}) caused by the higher micropore volume also visible for nitrogen.

As several measurements before (i.e. TGA, FTIR, and EA) presumed, that water is adsorbed in a significant amount, also water vapor sorption was carried out. **Figure 4.2-5 C** shows the isotherms of cG@700-SZ10 and cG@800-SZ10. As before, C_1N_1 material obtained at 700 °C and the NC obtained at 800 °C show very different characteristics. While cG@700-SZ10 shows a continuous water uptake with increasing relative pressure, cG@800-SZ10 shows almost no uptake at low relative pressure but a sharp increase starting at a relative pressure of ca. 0.5. As described in the introduction, the uptake at low relative pressure of cG@700-SZ10 can be translated into a hydrophilic character of the material and the low uptake at low relative pressures with a sharp increase at higher relative pressures with a large hysteresis to a more hydrophobic material with large mesopores volume. In this sense, both samples show unusual water sorption behavior. The C_1N_1 material obtained at 700 °C is very hydrophilic and cG@800-SZ10 shows an extremely high maximum water uptake when compared to other nitrogen-containing carbonaceous materials. The next section will focus on water sorption, therefore it will not be discussed in more detail here. However, I want to point out, that indeed, both samples adsorb a significant amount of water, proofing, that the oxygen detected by EA and EDX might belong to water. The first mass loss at ca. 100 °C in TGA curves and the peaks in FTIR spectra can be ascribed to water in the material.

For further understanding of the basic sites in the material CO_2 TPD measurements were conducted. **Figure 4.2-6 A** shows the TCD signal as a function of the temperature. cG@500-SZ10 has the most intense signal with two broad CO_2 desorption peaks at ca. 200 °C and 330 °C indicating that CO_2 binds through two binding sites with very high binding energies. cG@700-SZ10 shows a similar curve but with a shoulder at 150-200 °C indicating the coexistence of micropores in the material. cG@800-SZ10 has a significantly lower signal and an additional peak at ca. 130 °C, which can be ascribed to physisorbed CO_2 to the material. The lower signal of cG@800-SZ10 and the additional physisorbed CO_2 is in line with the rupture of the C_1N_1 material causing the loss of CO_2-specific cryptopores and sorption more similar to common NCs.

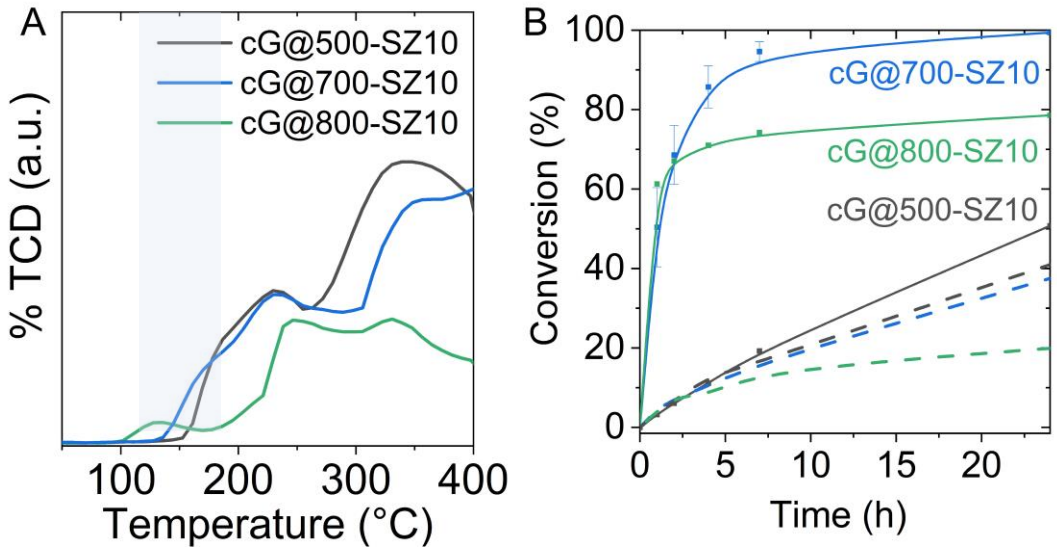

Figure 4.2-6. A) CO_2 TPD of cG@500-SZ10, cG@700-SZ10, and cG@800-SZ10. Blue background should visualize the desorption range of physisorbed CO_2. B) Time dependent results of Knoevenagel condensation reaction using cG@500-SZ10, cG@700-SZ10, and cG@800-SZ10 as catalyst. Solid lines stand for materials used after degassing at 150 °C for 20 h and dashed lines stands for materials used without degassing.

Finally, the materials were tested as a heterogeneous catalyst using the Knoevenagel condensation reaction as a model reaction. As shows, benzaldehyde and malononitrile were chosen as reagents. As shown before, materials adsorb water under ambient conditions, therefore it was necessary to degas all materials at 150 °C for 20 hours before using them as catalyst. **Figure 4.2-6 B** shows the conversion of benzaldehyde as a function of time. In dashed lines, the results without degassing are presented, confirming the immediacy of the degassing step to activate the samples. After degassing cG@500-SZ10 shows slow kinetics due to the not accessible active sites. With an increased condensation temperature to cG@700-SZ10, the development of micropores makes the active sites available and a conversion of 99 % after 24 hours is reached. After two hours a conversion of already 68 % shows fast kinetics of cG@700-SZ10. With cG@800-SZ10 as catalyst, also a conversion of 67 % is reached after two hours but increases just to 78 % after 24 hours. The use of other substrates, namely benzaldehyde with chloro- or methyl- in 4 position, give a conversion of 85 % and 68 % respectively, showing that an increasing size of the substrate lowers the conversion. With furfural as substrate, a conversion of only 46 % was achieved, which can be ascribed to the change of polarity of the substrate. However, all reactions show a selectivity towards 2-benzylidenemalononitrile of 99 % according to NMR.

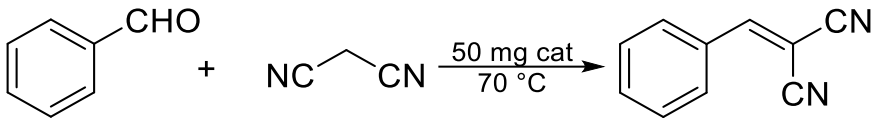

Figure 4.2-7. Knoevenagel condensation reaction of Benzaldehyde with malononitrile followed in this thesis.

As mentioned before, the Knoevenagel condensation reaction was chosen as a model reaction to evaluate the potential of the materials as basic heterogeneous catalyst. This approach was also used before and a look into reported results shows, that C_1N_1 materials are under the best performing materials. As is can be seen in **Table S 4.2-2** most reported materials are pre-treated

with strong bases to activate the base functionalities, while just simple degassing is needed to activate guanine-derived materials. Furthermore, not many materials report a conversion of 99 % with a selectivity of 99 %. These results indicate that the design of a basic heterogeneous catalyst depends on its composition and pore structure. cG@700-SZ10 has a high nitrogen content as well as a sufficient surface area with accessible pores for the substrates, which makes it a highly active and selective catalyst.

In this section, the preparation of porous carbonaceous materials derived from guanine with simple salt melt templating was presented. The formation of the materials with increasing condensation temperature and the influence of the amount of salt melt was examined. Results are in line with the results of the condensation of guanine without salt melt, described in the previous section. At 500 °C a non-porous polyguanine with a C/N ratio of 1 is obtained and with increasing temperature, a microporous C_1N_1 material develops. When heating up to 800 °C this framework is not stable anymore, and a highly nitrogen-doped porous carbonaceous material is obtained. The materials have been tested as basic heterogeneous catalysts in a Knoevenagel condensation reaction and cG@700-SZ-10 shows the highest activity with a conversion of 99 % after 24 hours. Furthermore, sorption experiments show that CO_2 binds strongly to C_1N_1 materials with a high selectivity, as also observed in the previous section. These findings further proofs the high stability if C_1N_1 materials and also demonstrates the potential of the material as basic heterogeneous catalyst.

4.3 Hydrophilic Porous Carbonaceous Materials derived from Uric Acid[5]

As mentioned in the previous section, guanine-derived materials show an unusual water sorption behavior. As described in the introduction, ordinary carbon materials are intrinsically hydrophobic. However, it is reported that nitrogen doping and pore size adjustment can tune the hydrophilicity and water uptake of carbonaceous materials. Hydrophilic carbonaceous materials are, for example, interesting candidates to use as adsorbents in heat transformation applications like TDCs and AHCs. Due to the low production costs and the possibility of large-scale synthesis from biomass-derived precursors, hydrophilic carbonaceous materials could potentially substitute the currently used zeolites or silica gels and thus improve the performance and economy of TDCs and AHCs. The incorporation of nitrogen into carbon networks can introduce surface polarity and thus, tune the hydrophilicity and allow water uptake at lower relative pressures. Literature also reports about an increase of water uptake at low relative pressures caused by micropores in the material while mesopores improve the maximum water uptake at higher relative pressures.[250, 277, 276, 183] In this section, the water adsorption behavior of uric acid-derived nitrogen-containing carbonaceous materials is analyzed.

Uric acid is a degradation product of purine nucleobases and remains a high structural similarity to nucleobases. Due to its similarity to guanine, it was chosen as precursor to prove the validity of the concepts described above. TGA in nitrogen atmosphere (**Figure 4.3-1 A**) shows that the mass loss of uric acid starts at 400 °C and ends at ca. 800 °C, similar to guanine, but with a shoulder at ca. 500 °C. Since condensation of guanine at 600 °C and 700 °C results in almost the

[5] Results of this section are adapted from the original work with permission of the authors:
J. Kossmann, R. Rothe, T. Heil, M. Antonietti, N. López-Salas, Journal of Colloid and Interface Science, Ultrahigh water sorption on highly nitrogen doped carbonaceous materials derived from uric acid, (2021), 602, 880-888.

same material, as described in section 4.1 and 4.2, while a temperature increase to 800 °C results in a very different product, uric acid was condensed at 500 °C, 700 °C, 750 °C, 800 °C, and 900 °C. The salt melt of NaCl and $ZnCl_2$ was chosen again to introduce porosity and used in a ratio of uric acid to NaCl to $ZnCl_2$ of 1:5:5. After heat treatment of the uric acid/NaCl/$ZnCl_2$ mixture and HCl washing, a black powder was obtained as product (**Figure 4.3-1 B**). Samples will be named UA-500-SZ, where UA stands for uric acid, 500 for the condensation temperature of 500 °C, and SZ for the salt melt NaCl/$ZnCl_2$. Differential thermal analysis of SZ in nitrogen atmosphere, shown in **Figure 4.3-1** proves that the salt melts before uric acid starts to condensate and thus the system is suitable for salt melt templating.

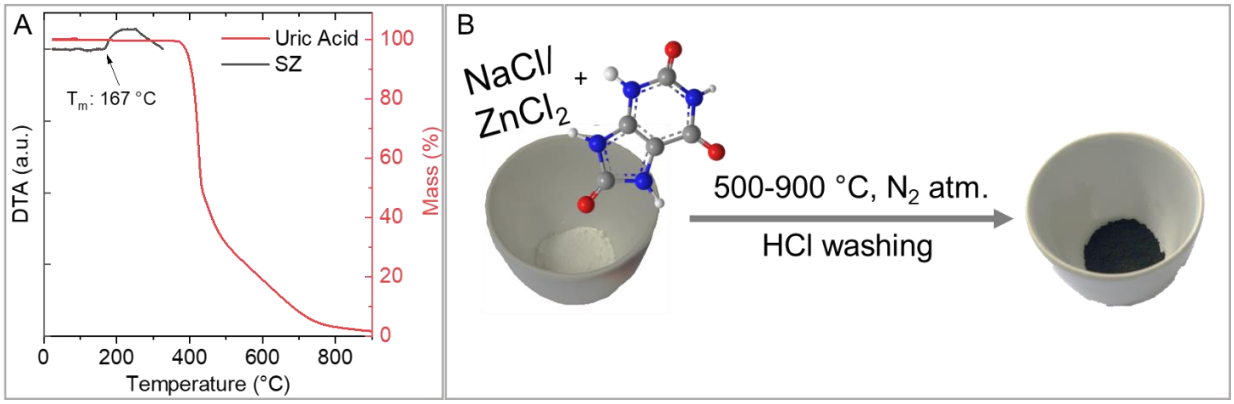

Figure 4.3-1. A) TGA in nitrogen atmosphere of uric acid (red) and differential thermal analysis (DTA) signal of NaCl/$ZnCl_2$ (SZ) (black). B) Schematic illustration of the synthetic procedure followed in this section.

EDX coupled to SEM was used to analyze the composition of the materials (spectra are shown in **Figure S 4.3-1**) and the C/N ratio was further verified by EA. The results are listed in **Table 4.3-1**. Carbon content increases and nitrogen content decreases with increasing temperature. At 500 °C the material consists of 49 at% carbon and 46 at% nitrogen resulting in a C_1N_1 material. At 700 °C the nitrogen content already decreases to 30 at% while the carbon content increases to 67 at% resulting in a C/N ratio of 2.2. The nitrogen content further decreases to a C/N ratio of 3.0, 5.9, and 6.4 for UA-750-SZ, UA-800-SZ, and UA-900-SZ respectively.

Deconvolution of C1s and N1s XPS spectra (see **Figure S 4.3-2**) gives further information about the binding of carbon and nitrogen. C1s deconvolution shows, that carbon is present in the form of C=C (284.4 eV), C-N (285.7 eV), and C-O (288.1 eV). With increasing temperature, the C-N content decreases. N1s deconvoluted spectra shows that nitrogen is present in form of pyridinic-N (398 eV), and pyrrolic-N (400 eV) in all materials. At higher temperatures, a peak at 401 eV appears which can be ascribed to quaternary-N, indicating the beginning of graphitization.[111] TGA in synthetic air of the samples in **Figure 4.3-2 A** shows a first mass loss at ca. 100 °C of

Table 4.3-1. Composition according to SEM-EDX in atomic%, C/N ratio according to EA in atomic%, and zinc content in weight% according to ICP-MS.

Sample	Composition according to SEM-EDX (at%)				C/N (EA)	Zn (wt%)
	C	N	O	C/N		
UA-500-SZ	49	46	5	1.1	1.1	1.4
UA-700-SZ	67	30	2	2.2	1.8	2.8
UA-750-SZ	73	24	3	3.0	2.6	0.8
UA-800-SZ	83	14	2	5.9	6.2	1.0
UA-900-SZ	82	13	5	6.4	-	0.6

ca. 5 %, which can be ascribed to adsorbed water. The mass loss is minor because the samples have been degassed at 150 °C for 20 h under high vacuum before the measurement. The rationale for this was also described in section 4.1 and 4.2. Furthermore, TGA shows that samples are stable up to ca. 400 °C in oxygen atmosphere, proofing their noble character. FTIR spectra in **Figure 4.3-2 B** show a broad band at 3100 cm^{-1} for samples UA-500-SZ, UA-700-SZ, and UA-750-SZ. This band can be ascribed to OH-stretching from water. The peaks at 1580 cm^{-1} and 1245 cm^{-1} can be assigned to conjugated nitrogen-containing rings.[249] It is worth mentioning, that the spectra of UA-500-SZ, UA-700-SZ, and UA-750-SZ are almost the same, whereas the peaks

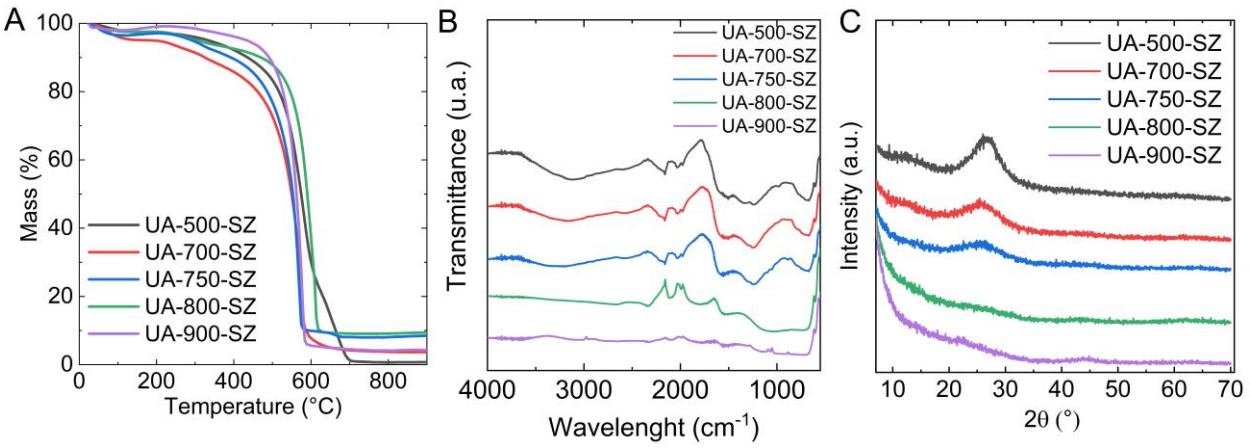

Figure 4.3-2. A) TGA in synthetic air, B) FTIR spectra, and C) PXRD pattern of UA-500-SZ, UA-700-SZ, UA-750-SZ, UA-800-SZ, and UA-900-SZ. Prior to all measurements, samples were degassed at 150 °C for 20 h under vacuum.

getting more undefined when increasing the temperature to 800 °C and almost disappear when going to 900 °C. PXRD spectra of the samples (**Figure 4.3-2 C**) show a broad peak at 26.5°, which is typical for graphitic stacking of condensed covalent structures. The intensity of this peak increases from UA-500-SZ to UA-750-SZ and is not detectable for UA-800-SZ and UA-900-SZ anymore, indicating a growing amorphous phase with temperature. **Figure 4.3-3** shows SEM micrographs of the materials. All samples have, as typical for salt melt templating, a colloidal structure with an increasing colloid size with increasing temperature. BF-STEM and HAADF-STEM images in **Figure S 4.3-3** of UA-800-SZ further shows mainly amorphous materials with small nanoscale domains with structural order. HAADF-STEM shows the porous structure of the material with a mesopores size of ca. 7 nm.

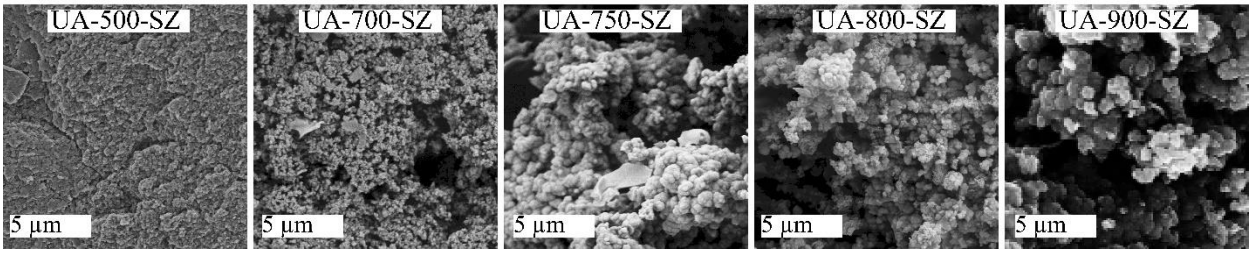

Figure 4.3-3. SEM micrographs of uric acid condensed at different temperatures with salt melt.

For surface area and pore structure analysis, nitrogen adsorption/desorption isotherms at 77 K (**Figure 4.3-4 A**) are measured and the resulting surface area according to BET model, micropore volume, mesopores volume, and total pore volume are given in **Table 4.3-2**. UA-500-SZ has almost no nitrogen uptake, indicating a very low surface area and a not developed pore structure. This was already observed for guanine condensed at 500 °C. At 700 °C a mostly microporous material with a type I isotherm was formed, with a SSA of 770 m^2 g^{-1}. Increasing the temperature to 750 °C results in the development of mesopores, indicated by a combination of a type I and II isotherm for UA-750-SZ and an increased micropore volume with a SSA of 1547 m^2 g^{-1}. DFT pore size distribution of UA-750-SZ (**Figure 4.3-4 B**) shows mesopores with a size of 3-4 nm and a cumulative pore volume of 0.76 cm^3 cm^{-1}. By increasing the temperature to 800 °C more mesopores develop, shown by a type IV isotherm with an H1 hysteresis and a SSA of 2590 m^2 g^{-1}. PSD shows a pore size of ca. 4-5 nm for UA-800-SZ with a cumulative pore volume of 1.75 cm^3 g^{-1}. Further increasing the temperature to 900 °C leads to slightly fewer micro- and mesopores than for UA-800-SZ, probably due to graphitization with a similar SSA of 2425 m^2 g^{-1}. **Figure 4.3-4 C** illustrates the corresponding CO_2 adsorption isotherms at 273 K.

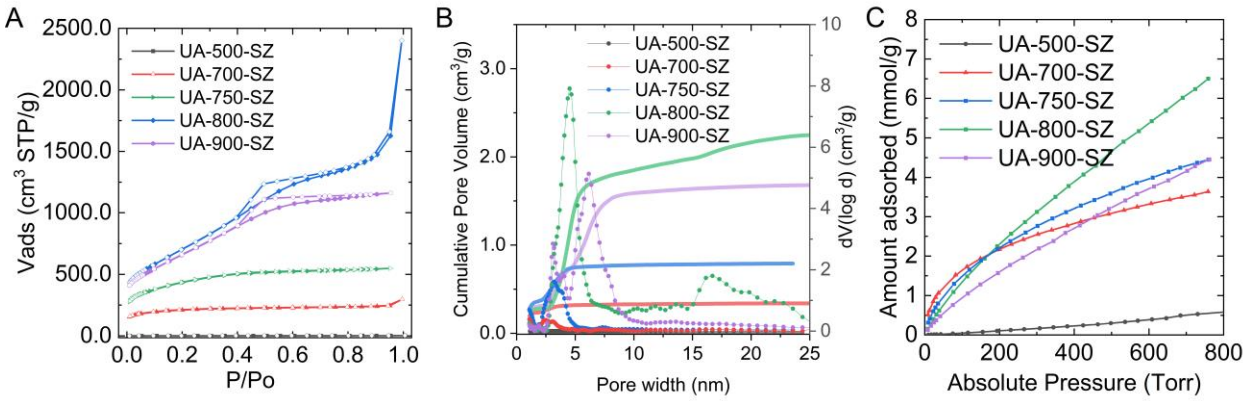

Figure 4.3-4. A) Nitrogen adsorption(filled symbols) and desorption (empty symbols) isotherms at 77 K, B) DFT pore size distribution applied to N_2 adsorption isotherms, and C) CO_2 adsorption isotherms at 273 K of uric acid condensates at 500°C – 900°C.

As expected from nitrogen sorption, UA-500-SZ does not show a significant CO_2 uptake. However, the CO_2 uptake increases drastically with increasing condensation temperature to 6.5 mmol g^{-1} at high pressures for UA-800-SZ. At this point, it is also worth pointing out the low-pressure region of the isotherms. As described in section 4.1 and 4.2, the shape of the CO_2 adsorption isotherm can give an idea about the strength of the CO_2 uptake and therefore about the polarity of the material. UA-700-SZ and UA-750-SZ show a strong concave shape, which decreases with increasing temperature, indicating a stronger polar character of UA-700-SZ and UA-750-SZ compared to UA-800-SZ and UA-900-SZ.

Table 4.3-2. Specific surface area (SSA) obtained by applying BET model, micropore volume (V_{Micro}), mesopore volume (V_{Meso}), and total pore volume (V_T) determined by nitrogen adsorption isotherms at 77 K; Maximum water uptake and water uptake at p/p_0 0.3 from water vapor isotherms at 298 K.

Sample	SSA[a]	V_{Micro}[b]	V_{Meso}[c]	V_T[d]	max. uptake H_2O	uptake H_20 at p/p_0 0.3
	[$m^2\,g^{-1}$]	[$cm^3\,g^{-1}$]	[$cm^3\,g^{-1}$]	[$cm^3\,g^{-1}$]	[g g^{-1}]	[g g^{-1}]
UA-500-SZ	1	0.06	0.00	0.00	0.18	0.10
UA-700-SZ	770	0.24	0.32	0.46	0.30	0.14
UA-750-SZ	1547	0.33	0.76	0.85	0.69	0.18
UA-800-SZ	2590	0.38	1.75	3.72	1.38	0.07
UA-900-SZ	2425	0.32	1.40	1.70	1.13	0.05

[a] Obtained using QSDFT method applied to N_2 adsorption isotherm at 77 K; [b] Obtained from CO_2 adsorption isotherms at 273 K using DFT model; [c] Obtained from N_2 adsorption isotherms at 77 K using DFT model and pores until pore width 7 nm; [d] at p/p_0 = 0.96 for pores with a diameter smaller than 60.0 nm.

As described before, uric acid-derived materials were synthesized to explore their water sorption behavior and thus their potential as adsorbents for TDCs and AHPs. **Figure 4.3-5 A** shows the water vapor adsorption/desorption isotherms at 298 K. UA-500-SZ and UA-700-SZ appear in a type I isotherm with a progressively increasing water vapor uptake starting from very low relative pressures, indicating a strong water-adsorbent interaction. The higher uptake of UA-700-SZ compared to UA-500-SZ correlates with its higher pore volume. UA-750-SZ shows a type IV isotherm. Water vapor uptake increases with a slightly concave shape starting at low relative pressures. The hysteresis loop appearing with desorption shows water condensed in the mesopores.[183, 250] When increasing the condensation temperature further to 800 °C, a type V isotherm can be seen with a sharp increase of adsorbed water at a relative pressure of ca. 0.4. The low uptake at low relative pressures indicates weaker water-adsorbent interactions due to larger pores with less nitrogen content. The broader hysteresis loop can be ascribed to a larger mesopore volume developed at higher temperatures. Despite the weaker interaction between water and the material, the maximum water uptake at high relative pressures is remarkably high for carbonaceous materials. The water uptake of 1.38 g g^{-1} is in the range of reported MOFs. **Figure 4.3-5 B** shows a magnification to the low relative pressures area of the isotherms to obtain a closer look at the hydrophilicity of the materials. Due to the large water uptake of 0.10 g g^{-1} to 0.18 g g^{-1} at a relative pressure of 0.3, UA-500-SZ, UA-700-SZ, and UA-750-SZ can be classified as hydrophilic materials, which are comparable to MIL-101-Cr (ca. 0.1 g g^{-1} at p/p_0 0.3).[168, 176] UA-800-SZ has the lowest uptake at low relative pressures, indicating a less polar character of the material. **Figure 4.3-5 B** also shows that all hydrophilic materials have a concave shape against the Y-axes and all hydrophobic materials a convex shape. The changes in hydrophilicity can be correlated with the nitrogen content in the material. When nitrogen content drops from UA-750-SZ to UA-800-SZ, hydrophilicity changes. **Figure 4.3-5 C** shows the micropore volume and water uptake at low relative pressure as a function of the C/N ratio. With increasing micropore

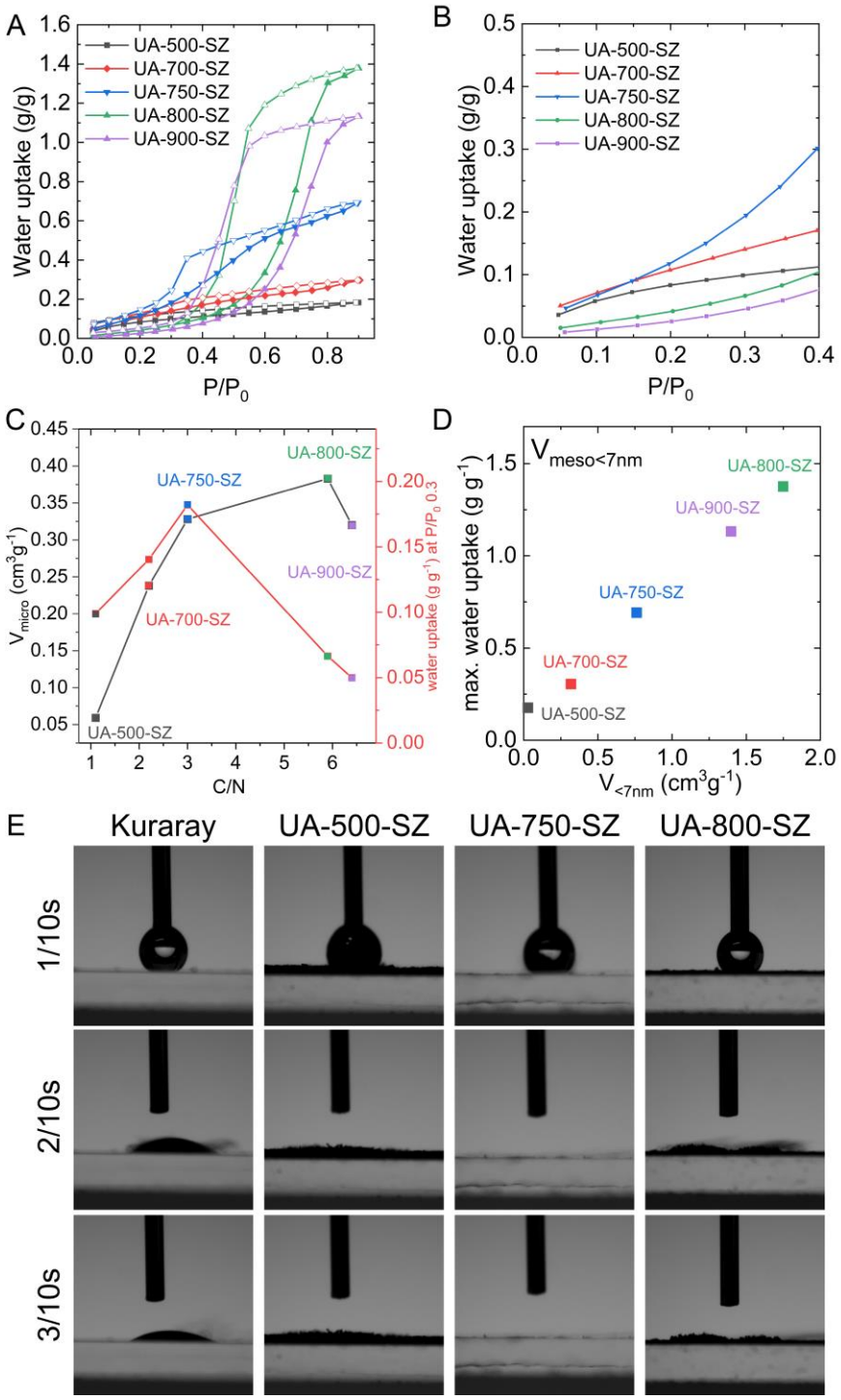

Figure 4.3-5. A) Water vapor adsorption and desorption (filled and empty symbols) isotherms at 298 K. B) Water uptake at low relative pressure. C) Volume of micropores calculated from CO_2 isotherms at 273 K using DFT model and water uptake at a relative pressure of 0.3 vs. C/N ratio. D) Volume of mesopores smaller than 7 nm calculated from nitrogen isotherms applying DFT model vs. maximum water uptake. E) Snapshots every 1/10 s of videos recorded during water contact angle experiments.

volume caused by increasing condensation temperature, the water uptake at low relative pressures increases. This correlation can be overserved until the C/N ratio increases drastically from UA-750-SZ to UA-800-SZ, indicating that both, micropore volume and nitrogen content, are critical for water uptake at low relative pressure. In **Figure 4.3-5 D,** the mesopores volume is plotted as a function of the maximum water uptake, showing a linear correlation.

Dynamic contract angle measurements, shown in **Figure 4.3-5 E** further show the hydrophilicity of the materials. Water adsorption of the material occurs faster than on commercial carbon (Kuraray). The detection limit of 1/10 of a second is too high to measure the contact angle of the materials. On Kuraray, the drop stays more than 3/10 of a second, while the impregnation on the uric acid-derived materials is faster than 1/10 of a second.

Within this study, not only the relation between pore structure, nitrogen content, and water uptake at different pressures have been explained, but also materials with outstanding water uptake have been presented. As mentioned before, common carbon materials are hydrophobic, but it is known that nitrogen doping, and pore structure adjustment can improve the water uptake. However, to the best of my knowledge, such hydrophilic carbonaceous materials have not been reported before. In addition, the ultra-high maximum water uptake of UA-800-SZ of 1.38 g g^{-1} is above the range of carbonaceous materials and shows a performance like zeolitic imidazolate framework-derived porous carbon materials, positioning itself in the range of the best performing metal-organic frameworks (**Table S 4.3-1**). This class of materials could indeed be used in TDCs and AHPs with water as refrigerant and thus improve the system's efficiency by using a cheap and sustainable sorption material like the present uric acid-derived materials. First cycle stability tests UA-750-SZ and UA-800-SZ (**Figure S 4.3-4**) show stability of both materials over five cycles without any degassing step in between. UA-750-SZ shows just a 14 % loss after two cycles but stabilizes afterwards while UA-800-SZ does not show any loss over all five cycles.

5. Cu(II)/Cu(I) Based Nanoclusters Decorate N-Doped Carbonaceous Materials for Oxygen Reduction Reaction[6]

To further validate the wide applicability of the design of porous highly nitrogen-doped carbonaceous materials by salt melt templating and a smart chosen, simple molecular precursor, a Cu(II)/Cu(I) nanocluster decorated porous carbonaceous material and its application as electrocatalyst for ORR will be presented in the following. The IL 1-butyl-4-methylpyridinium tricyanomethanide (BTCN) was chosen due to its high nitrogen content and the expected stabilization during condensation due to the cyano-group.

The preparation of the materials is graphically shown in **Figure 5-1**. BTCN as a carbon precursor was mixed with KCl/$ZnCl_2$ as solvent and porogen (in a BTCN:KCl:$ZnCl_2$ weight ratio of 1:5:5) at 800 °C in nitrogen atmosphere. Subsequent washing with HCl leads to the porous, nitrogen-doped carbonaceous support (see **Figure 5-1 A**), which will be named BTCN-Cu0 in the following. BTCN-Cu0 is obtained with a yield of 24 wt% and a high nitrogen content of 20 at%, according to SEM-EDX (**Table 5-1**). Despite intensive HCl washing, ca. 1.5 wt% of zinc was still detected by ICP-OES, as also reported for prior materials.

Copper loading was performed by stirring BTCN-Cu0 with a solution of copper (II) acetate in acetonitrile for 2 h. After drying off the solvent, the impregnated BTCN-Cu0 was heated to 350 °C in air (**Figure 5-1 B**). Different copper loadings of the final product were achieved by adjusting the copper (II) acetate solution concentration. In the following, samples will be named according to their copper loading (i.e. BTCN-Cu1 was synthesized with 1 wt% copper load). ICP-OES analysis confirmed the copper contents to be 0.8 wt%, 2.2 wt%, and 3.7 wt% for BTNC-Cu1, BTCN-Cu2, and BTCN-Cu4 respectively, which are in the range of the initially loaded amounts.

[6] Results of this section are adapted from the original work with permission of the authors:
J. Kossmann, M. L. Ortíz Sánchez-Manjavacas, H. Zschiesche, N. Tarakina, M. Antonietti, J. Albero, N. López-Salas, J. Mater. Chem. A, Cu^{II}/Cu^{I} decorated N-doped noble carbonaceous electrocatalysts for the oxygen reduction reaction, (2022).

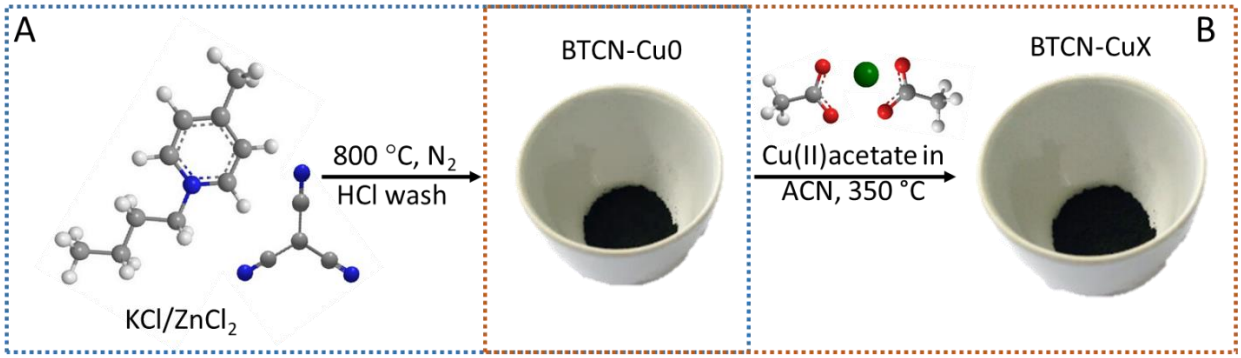

Figure 5-1. Schematic illustration of the synthetic procedure described in this section. A) 1-butyl-4-methylpyridinium tricyanomethanide (BTCN) and the salt melt are mixed and heat-treated at 800 °C under nitrogen atmosphere and subsequently washed with HCl. B) The product (BTCN-Cu0) is further used as support for copper loading: BTCN-Cu0 is added to a solution of copper (II) acetate in acetonitrile and stirred for 2 h. After removing acetonitrile, the copper-BTCN-Cu0 mixture is heated to 350 °C in air. The obtained product is a black powder.

Investigations on the composition of the materials were performed by SEM-EDX analysis and results are shown in **Table 5-1**. Carbon and nitrogen contents decrease slightly with increasing copper content, while the C/N ratio remains approximately constant, which points again at the stability of the carbonaceous material. The increase in oxygen content of 5.0 at%, 9.7 at%, 12.3 at%, and 11.4 at% of BTCN-Cu0, BTCN-Cu1, BTCN-Cu2, and BTCN-Cu4 respectively might be ascribed to the introduction of oxygen functionalities by the copper (II) acetate salt during the calcination. To ensure that the increased oxygen content is not caused by the oxidation of BTCN-Cu0 during the calcination procedure, BTCN-Cu0 has also been submitted to calcination at 350 °C. SEM-EDX analysis of the sample does not show a significant change in composition (**Table S 5-1**).

Table 5-1. Yields and composition in at% according to SEM-EDX (with standard deviation in brackets), copper content according to ICP-OES analysis, and S_{BET} from nitrogen adsorption isotherms at 77 K.

Sample	Yield	SEM-EDX [at%]				ICP-OES [wt%]	S_{BET}[d]
	wt%	C	N	O	C/N[c]	Cu	[m^2g^{-1}]
BTCN-Cu0	24[a]	74.0 (2)	20.4 (2)	5.0 (1)	3.6 (0.4)	-	1643
BTCN-Cu1	90[b]	72.3 (3)	18.0 (2)	9.7 (1)	4.0 (0.5)	0.8	1615
BTCN-Cu2	88[b]	68.1 (4)	19.6 (3)	12.3 (3)	3.5 (0.6)	2.2	1522
BTCN-Cu4	85[b]	72.1 (1)	16.5 (1)	11.4 (1)	4.4 (0.3)	3.7	1358

[a] BTCN to BTCN-Cu0; [b] BTCN-Cu0 to copper decorated material; [c] propagation of error from standard deviation of carbon and nitrogen content; [d] obtained using QSDFT method applied to N_2 adsorption isotherms at 77 K.

TGA in synthetic air (**Figure 5-2 A**) shows the thermal stability in oxygen containing atmosphere of all materials. Interestingly, a slight decrease with increasing copper loading can be identified. While BTCN-Cu0 is stable up to 600 °C, a shift of ca. 25 °C to BTCN-Cu1 to 575 °C and a further shift of ca. 25 °C of BTCN-Cu2 to 550 °C can be seen. The shift of BTCN-Cu2 to BTCN-Cu4 of ca. 50 °C to 500 °C is in line with this.

Nitrogen adsorption/desorption isotherms at 77 K are shown in **Figure 5-2 B**. All isotherms are very similar and type I, indicating mainly microporous materials with a small amount of mesopores. A slight decrease of nitrogen adsorption with increasing copper loading can be seen and is further confirmed by the calculated SSA_{BET} shown in **Table 5-1**. The slight SSA_{BET} decrease from 1643 $m^2\,g^{-1}$ for BTCN-Cu0 to 1615 $m^2\,g^{-1}$, 1522 $m^2\,g^{-1}$, and 1358 $m^2\,g^{-1}$ for BTCN-Cu1, BTCN-Cu2, and BTCN-Cu4 respectively might be ascribed to deposition of the copper species causing a small percentage of pore blocking in the material.

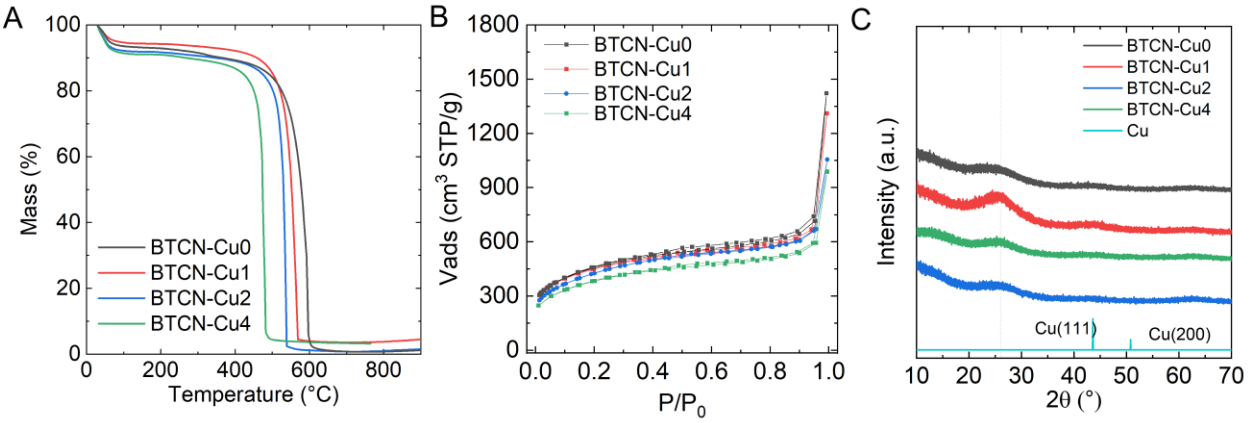

Figure 5-2. A) TGA in synthetic air, B) nitrogen adsorption/desorption isotherms at 77 K, and (C) PXRD pattern of BTCN Cu0, BTCN-Cu1, BTCN-Cu2, and BTCN-Cu4.

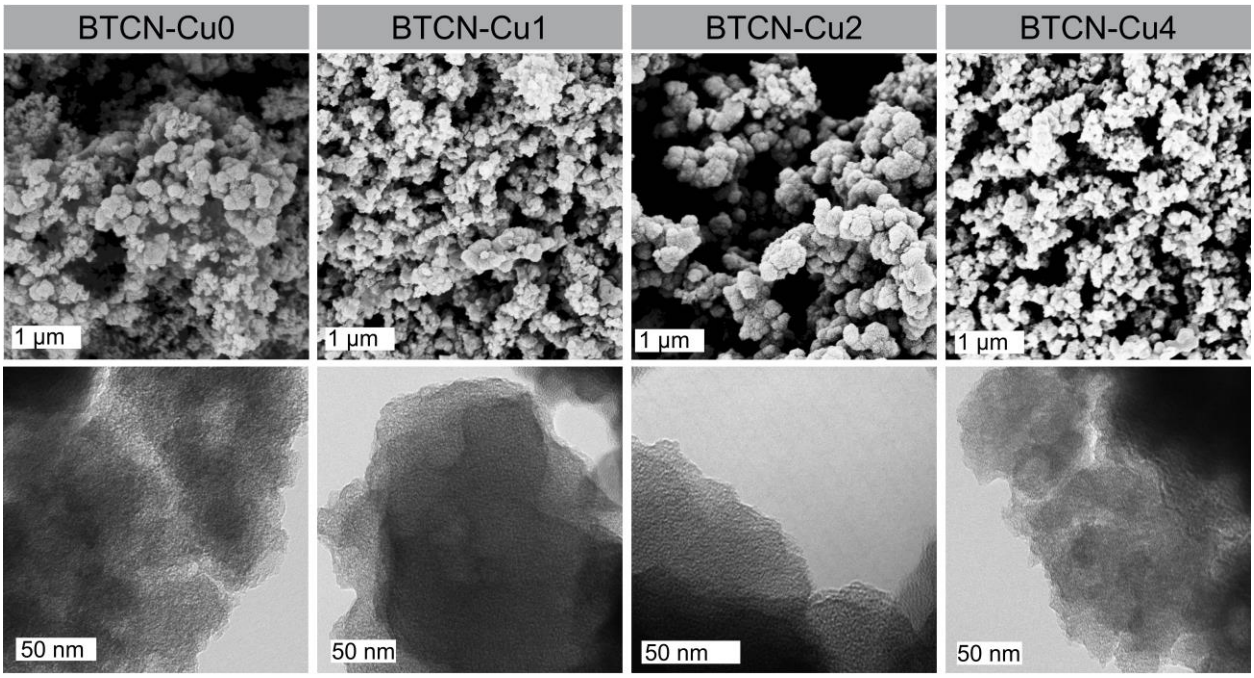

Figure 5-3. Up SEM and down TEM micrographs of BTCN-Cu0, BTCN-Cu1, BTCN-Cu2 and BTCN-Cu4.

First investigations on how copper is present in the materials have been performed by PXRD analysis. PXRD patterns of the materials (**Figure 5-2 C**) show no diffraction peaks of copper crystals (shown in light blue) for any of the materials, indicating the absence of copper nanoparticles. The broad diffraction peak at 27 ° is typical for nitrogen-doped carbonaceous materials and can be ascribed to graphitic stacking of the carbonaceous support. SEM and TEM

micrographs are presented in **Figure 5-3.** SEM micrographs show a colloidal carbon structure as typically obtained with salt melt templating with primary carbon particles smaller than 200 nm. TEM micrographs show a sheet-like structure of the materials. All samples, independent of the copper loading, appear similar with both techniques, further confirming the stability of the material during copper loading process, which is in line with previously presented results. Furthermore, as expected after PXRD measurements, no copper nanoparticles or bigger clusters can be seen by TEM micrographs on the surface of the materials, indicating a finer distribution of copper. This is confirmed by HAADF-STEM images shown in **Figure 5-4.** The carbonaceous support appears grayish with higher intensity in thicker regions. Elements with a higher mass appear as bright spots indicating the presence of single atom or atom-cluster metallic sites. Therefore, it can be assumed that these spots originate from zinc or copper in these materials. This hypothesis is additionally supported by the micrograph of BTCN-Cu0, which shows the presence of zinc (**Figure 5-4**). Anyway, the number of bright spots per projected area increases with copper loading, giving reason for the assumption of homogeneously distributed copper atoms or clusters on the material.

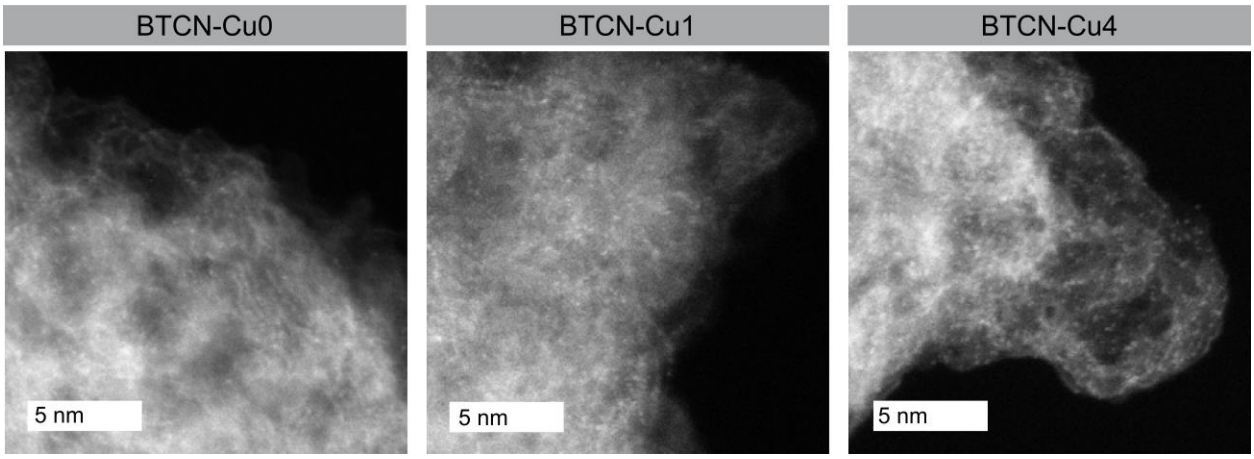

Figure 5-4. HAADF-STEM images of BTCN-Cu0, BTCN-Cu1, and BTCN-Cu4.

XPS spectra help to understand the chemical nature of copper in the material and possible chemical changes with copper loading. Cu2p spectra of BTCN-Cu1, BTCN-Cu2, and BTCN-Cu4 are shown in **Figure 5-5**. All spectra show peaks at 954.2 eV and 934.4 eV, which can be ascribed to Cu(II). Interestingly, with increasing copper loading, two additional peaks at 951.7 eV and 931.7 eV appear which can be ascribed to Cu(I).[187, 202, 218, 251] In the spectra of BTCN-Cu1 these peaks are almost not visible, while the spectra of BTCN-Cu2 already show clear peaks and for BTCN-Cu4 these peaks are as intensive as the Cu(II) peaks. A Cu(II)/Cu(I) ratio of 3.5, 2, and 1 can be identified for BTCN-Cu1, BTCN-Cu2, and BTCN-Cu4 respectively. Such a formation of Cu(II) and Cu(I) has been reported for nitrogen and oxygen based ligands in molecular compounds and ascribed to copper redox valence tautomerism.[251-252] In this context, the formation of Cu(I) has been reported to be stabilized by electron withdrawing from the ligands.[253] The here presented materials exhibit a high content of nitrogen, which can be electron withdrawing and thus stabilize the copper(I) centers.

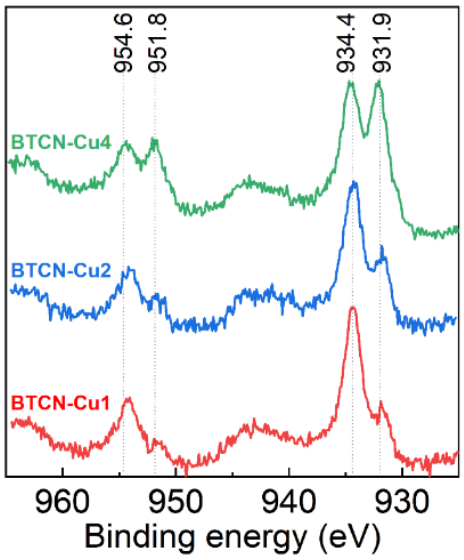

Figure 5-5. Cu2p XPS spectra of BTCN-Cu1 (red), BTCN-Cu2 (blue), and BTCN-Cu4 (green).

The deconvoluted N1s and C1s XPS spectra of the samples, shown in **Figure 5-6**, confirm this assumption. The most drastic change can be seen from the sample without copper (BTCN-Cu0)

to the sample after copper treatment (BTCN-Cu1). The C1s spectra is the result of adding up signals from C=C bonds (284.7 eV), C-N bonds (286.1 eV), and a third peak at 288 eV, which is ascribed to electron poor C-N bonds. The C-N to C=C ratio increases from BTCN-Cu0 to BTCN-Cu1 and stays approximately stable with further increase of copper loading. Interestingly, the peak at 288 eV becomes more defined with increasing copper loading, which shows the formation of electron poor conjugated C-N bonds. The N1s spectra is the sum of four species centered at 398.5 eV, 400.0 eV, 401.2 eV, and 404 eV, which are typically ascribed to N-pyridinic, N-pyrrolic, N-pyridonic, and in-plane N-quaternary respectively. Interestingly, the electron poor N-pyridonic signal at 401.2 eV increases with the introduction of copper to the material, which also points to the electron withdraw of nitrogen to stabilize copper(I) sites.

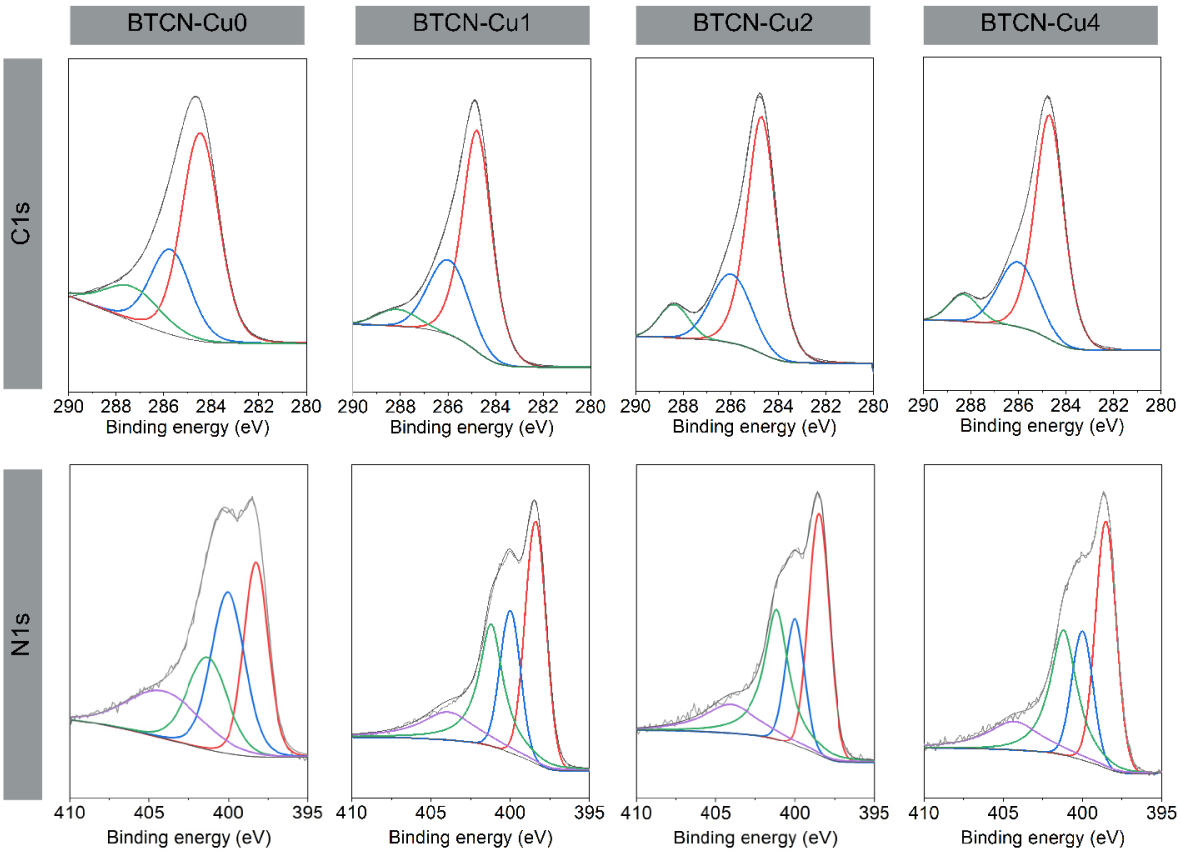

Figure 5-6. Deconvoluted C1s and N1s XPS spectra of BTCN-Cu0, BTCN-Cu1, BTCN-Cu2, and BTCN-Cu4.

Evaluation of the obtained materials as electrocatalyst for the ORR has been performed by rotating disk electrode (RDE) and rotating ring disk electrode (RRDE) measurements in a three-electrode setup using 0.1 M KOH as electrolyte. A Pt-wire was used as counter electrode and an $Ag/AgCl_{(sat.\ KCl)}$ as reference electrode. The working electrode was prepared by dropping 10 µl of the freshly prepared ink on the glassy carbon tip of the RDE/ RRDE and drying at room temperature. The ink was prepared by five minutes sonication of a mixture of isopropyl alcohol, distilled water, Nafion, and the catalyst. To have a comparison with a benchmark catalyst, the measurements were also performed with a commercial carbon/Pt 20% powder as catalyst under similar conditions. CV measurements in nitrogen-saturated electrolyte (**Figure S 5-1**) show a rectangular shape, indicating that no reaction takes place under these conditions. Whereas CV curves in oxygen saturated electrolyte show a clear reduction peak, showing the activity of the catalysts towards oxygen reduction (see **Figure S 5-1**). To further determine the performance of the catalysts, LSV curves at 1600 rpm were recorded in oxygen-saturated electrolyte, shown in **Figure 5-7 A**. These curves give the onset potential (E_{Onset}), the half-wave potential ($E_{1/2}$), and the limiting current density (J_L) of each material. The values are listed in **Table 5-2**. Interestingly, the onset potential (E_{Onset}) decreases with the introduction of copper from 0.93 V for BTCN-Cu0 to 0.81 V for BTCN-Cu1 but then increases with the loading of more copper to 0.91 V and 0.94 V for BTCN-Cu2 and BTCN-Cu4 respectively. The half-wave potential ($E_{1/2}$) follows the same trend reaching a value of 0.86 V for BTCN-Cu4. Overall, the onset and half-wave potentials of BTXCN-CuX materials are below the obtained values with carbon/Pt 20%. But interestingly, all limiting current densities (J_l) observed for BTCN-CuX materials are larger than that obtained for the benchmark carbon/Pt 20% catalyst.

Table 5-2. Summary of data obtained by LSV curves in 0.1 M KOH, a scanning rate of 10 mV s^{-1}, and a rotation speed of 1600 rpm using a rotating ring electrode. Limiting current density at 0.5 V vs. RHE.

Sample	E_{Onset} V vs. RHE	$E_{1/2}$ V vs. RHE	J_l^a mA cm^{-2}	Tafel slope mV/dec
BTCN-Cu0	0.93	0.83	-7.0	131
BTCN-Cu1	0.81	0.78	-7.4	128
BTCN-Cu2	0.91	0.83	-5.1	99
BTCN-Cu4	0.94	0.86	-7.0	87
Carbon/Pt 20%	1.00	0.92	-6.5	113

Next, it was investigated whether the catalysts induce oxygen reduction undergoes a two- or four-electron transfer. Therefore, LSV curves at different rotation rated were measured (**Figure 5-2**) and analyzed by the Koutecky-Levich equation. This equation can be used to obtain *n* (*n* being the number of electrons transferred) in the ORR mechanism. For further explanation of the Koutecky-Levich equation and all other equations used in the following see method part 8.2. As shown in **Figure 5-7 B**, all presented materials catalyze the ORR in the desired four-electron mechanism. To further validate the four-electron transfer and exclude any hydrogen peroxide production, additional RRDE measurements of BTCN-Cu0, BTCN-Cu4, and the bare glassy carbon were performed. An RRDE is built of a disk, where the reduction takes place and an additional ring where subsequent oxidation of any reaction products can take place. In the case of ORR, in a two-electron mechanism, hydrogen peroxide would be produced at the disk and oxidized at the ring. If the reaction goes in a four-electron path, no reaction takes place at the ring. As shown in **Figure 5-7 C**, the electron transfer number of four is validated and no hydrogen peroxide production can be detected for BTCN-Cu0 and BTCN-Cu4. Whereas the glassy carbon gives an electron transfer number of two and a hydrogen peroxide yield of 70-90 %.

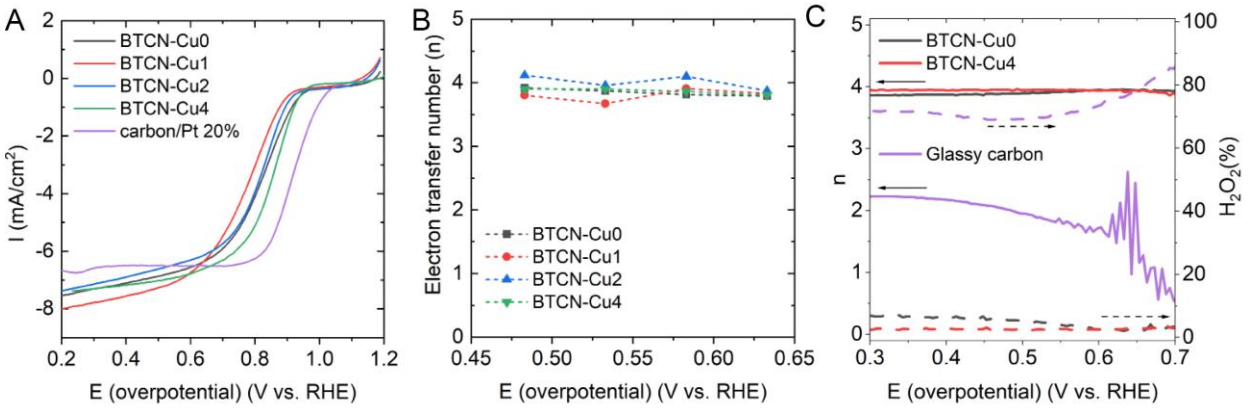

Figure 5-7. A) LSV curves with a rotation speed of 1600 rpm. B) Number of transferred electrons (*n*) at potentials from 0.45 V to 0.65 V (vs. RHE) obtained using the Koutecky-Levich equation and C) electron transfer number (lines) and H_2O_2 yields (dashed lines) of ORR in 0.1 M KOH solution with a scan rate of 10 mV s^{-1} and a stirring rate of 1000 rpm with a ring potential of 0.3 V vs. $Ag/AgCl_{(sat.\ KCl)}$ using an RRDE with BTCN-Cu0 and BTCN-Cu4 in comparison the glassy carbon.

Tafel plots give insights into the kinetics of the reaction (i.e. a smaller slope means the reaction happens faster). **Figure 5-8 A** shows the Tafel plots and the obtained slopes for the BTCN-CuX materials as well as for the carbon/Pt 20% catalyst. Interestingly, the slope decreases with the introduction of copper from 131 mV dec^{-1} for BTCN-Cu0 128 mV dec^{-1} for BTCN-Cu1. By further increasing copper loading, the slope also further decreases to 99 mV dec^{-1} for BTCN-Cu2, and to

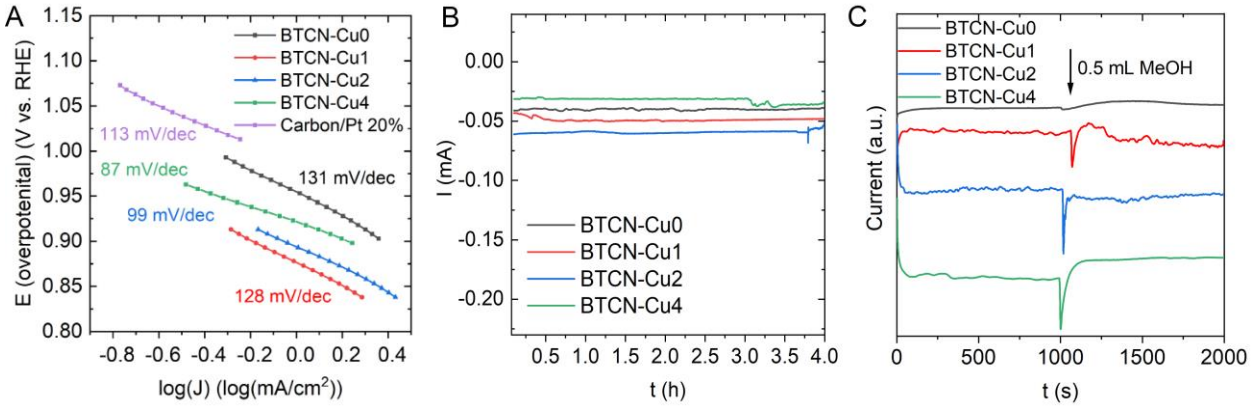

Figure 5-8. A) Calculated Tafel plots with slopes of BTCN-Cu0, BTCN-Cu1, BTCN-Cu2, and BTCN-Cu4.C) Chronoamperometrie at 0.15 V vs. $Ag/AgCl_{(sat.\ KCl)}$ over 4 hours and C) chronoamperometrie curves at 0.15 V vs. $Ag/AgCl_{(sat.\ KCl)}$ and injecting 0.5 mL MeOH after 1000s.

87 mV dec^{-1} for BTCN-Cu4. This value is much lower than the obtained Tafel slope for carbon/Pt 20% with 113 mV dec^{-1}, showing that the reaction goes faster with BTCN-Cu4. According to XPS results, BTCN-Cu4 has the larger Cu(I) amount. Interestingly, Chidsey, Stack, and coworkers reported in 2007 about copper complexes with 1,10-phenanthroline ligands and the responsibility of Cu(I) for the adsorption of O_2.[254] According to their findings, the reduction of Cu(II) to Cu(I) is the limiting step of the reaction. This was confirmed in 2011 by Langermann and Hetterscheid, who used copper(II) tris(2-pyridylmethyl)amine complexes and reported that the coordination of O_2 to Cu(I) presents the rate-limiting step.[255] Therefore, the faster oxygen reduction by BTCN-Cu4 can be explained by the higher amount of Cu(I) centers in BTCN-Cu4 compared to BTCN-Cu1. The Cu(I) centers of BTCN-Cu4 are stabilized due to the high amount of nitrogen being present in the carbonaceous support.

To evaluate the durability of the electrocatalyst, chronoamperometry measurements over four hours were performed with a stable potential of 0.15 V vs. $Ag/AgCl_{(sat.\ KCl)}$. **Figure 5-8 B** shows that all materials are stable without any current loss over the tested time. The stability of copper on the support was confirmed by ICP measurements, with a negligible loss of copper below 0.03 wt%. In addition, the stability against methanol crossover was tested. Therefore, 0.5 ml of methanol was added after 1000 s of a chronoamperometry measurement. As it can be seen in **Figure 5-8 C**, BTCN-Cu0 does not show any significant current change when adding methanol. BTCN-CuX materials show a current peak when adding methanol but a stabilization back to the initial current after 50 seconds, proving the stability of the materials in presence of methanol.

The lower Tafel slope together with the large stability and activity of BTCN-Cu4 compared to the benchmark catalyst carbon/Pt 20%, makes the material a very promising electrocatalyst for the ORR. A literature comparison with other Cu-NCs for ORR is shown in **Table S 5-2**. It illustrates that the performance of BTCN-Cu4 regarding stability and activity are among the best reported

values in literature and highlights the potential of BTCN-Cu4 to be used in FCs and replace rare platinum based catalysts. Overall, in this section, the simple and cost-efficient synthesis of a highly nitrogen-doped carbonaceous material by condensation of an IL by salt melt templating is presented. By smart choice of the precursor, a large nitrogen content can be obtained without any post treatment. Further utilization of the high nitrogen content is shown by subsequent Cu(II)/Cu(I) nanocluster decoration. The high nitrogen content does not just stabilize the metal active species but also stabilizes copper centers in Cu(I) state, which further enhances the efficiency of the catalyst.

6. Summary, Conclusions, and Perspectives

The central aim of this thesis is the simple condensation of smart chosen molecular precursors to obtain highly nitrogen-doped carbonaceous materials with controllable porosity. The presented research contributed to the expansion of knowledge about carbonaceous materials, their synthesis, and structure-performance relation to make them more attractive for industrial applications and thus contribute to the use of less metals and hazardous materials. The synthesized carbonaceous materials obtained from stable precursors show a high thermal and chemical stability, a wide range of nitrogen contents, and are shown to be excellent sorbents for carbon dioxide and water as well as active catalysts.

In chapter 4, the sorption behavior of the materials played a central role. Section 4.1 presents the synthesis of C_1N_1 materials with structural porosity stable up to 700 °C via simple condensation of guanine. The high affinity to CO_2 of C_1N_1 materials in combination with a low nitrogen uptake results in an $IAST_{CO2/N2}$ selectivity value of 97. Because of the high selectivity combined with a heat of adsorption of 59 kJ mol^{-1}, which is well above the usual physisorption of CO_2, these structural porosity was called cryptopores (crypto=hidden). Cryptopores are highly attractive to one gas (i.e. CO_2) but hidden for other molecules (i.e. nitrogen). Applying a condensation temperature above 700 °C breaks this structure, resulting in a nitrogen-depleted material. In section 4.2 surface area of guanine condensates was increased by adding a salt melt to the synthesis as template and solvent. Analysis of the obtained materials shows the stability of C_1N_1 materials obtained from guanine are also stable under these synthetic conditions. At a condensation temperature above 700 °C, the structure breaks, as it has been observed without the salt melt in section 4.1 and a popped-up, nitrogen-doped carbonaceous material with a high surface area is obtained. The obtained C_1N_1 materials show almost the same selectivity as presented before but with an increased CO_2 uptake due to formed micropores. The high affinity towards CO_2 gives evidence for the assumption of basic sites on the surface of the material.

Therefore, the materials are also tested as basic heterogeneous catalysts in a model reaction, showing also great potential in this field of application.

As indicated by TGA measurements and the necessary degassing before catalytic tests, materials obtained in section 4.2 adsorb a high amount of water. Therefore, investigations on the water sorption of uric acid-derived materials are presented in section 4.3. Even though uric acid is a degradation product of guanine, the behavior upon condensation is slightly different. The C_1N_1 structure breaks already before 700 °C, giving a C_2N composition at 700 °C. For the discussed materials from uric acid, a wide range of different nitrogen contents and pore volumes were obtained, giving the opportunity to discuss the water sorption behavior in relation to nitrogen content and pore structure. Results show that the hydrophilicity is dependent on the nitrogen content as well as on micropores, and the water capacity depends on the mesopores volume. Even though carbonaceous materials are known to be rather hydrophobic, section 4.3 presents highly hydrophilic materials and a water uptake, which is in the range of best performing MOFs, however without containing metals. These findings open the utilization of carbonaceous materials as adsorbents in heat transformation applications.

Chapter 5 describes the use of IL-derived N-doped carbonaceous materials as support for copper nanocluster. The choice of the precursor results in a high nitrogen content, which stabilizes the metal active sites, and the salt melt synthesis gives a highly porous support. The materials with different copper loadings are used as catalysts for the oxygen reduction reaction. Results show a high selectivity towards the four-electron mechanism, fast kinetics, and high stability of the catalyst. XPS shows that the composition of the clusters changes from 3.5 to 1 Cu(II)/Cu(I) when the copper loading changes from 1 wt% to 4 wt%, which enables the oxygen binding during the ORR. The synthesized material outperforms the tested commercial carbon/platinum 20%

benchmark catalyst in terms of stability against methanol crossover and kinetics, emphasizing the high potential to replace rare platinum-based catalysts in fuel cells.

Further investigations on the new bulk C_1N_1 materials are ongoing. The mechanistic understanding of the formation is a topic of interest to transfer the gained knowledge to other precursors and materials. Especially the synthesis of a bulk crystalline C_1N_1 material and the examination of theoretical predicted properties could lead to a new high-performance material. Furthermore, the described sorption of carbon dioxide and water should be investigated more intensively and transferred to experiments that are closer to the real applications. Concerning the results presented in section 5, it is obvious that the coordination of copper needs more investigations to understand the interactions on the material. Furthermore, the performance in a real fuel cell should be examined.

7. References

[1] K. S. Novoselov, A. K. Geim, S. V. Morozov, D. Jiang, Y. Zhang, S. V. Dubonos, I. V. Grigorieva, A. A. Firsov, *Science* **2004**, *306*, 666-669.

[2] M. Antonietti, M. Oschatz, *Advanced Matererials,* **2018**, *30*, 1706836.

[3] N. N. Greenwood, A. Earnshaw, *Chemistry of the Elements*, Elsevier, **2012**.

[4] Y. Gogotsi, V. Presser, *Carbon nanomaterials*, CRC press, **2013**.

[5] R. E. Jelley, A. G. Blackman, *Nature chemistry,* **2019**, *11*, 751-756.

[6] E. Riedel, C. Janiak, *Anorganische Chemie*, de Gruyter, **2011**.

[7] F. Wöhler, *Annalen der Physik,* **1828**, *88*, 253-256.

[8] J. Shorter, *Chemical Society Reviews,* **1978**, *7*, 1-14.

[9] H. Sicius, *Kohlenstoffgruppe: Elemente der vierten Hauptgruppe: eine Reise durch das Periodensystem*, Springer-Verlag, **2015**.

[10] E. A. Müller, L. F. Rull, L. F. Vega, K. E. Gubbins, *The Journal of Physical Chemistry,* **1996**, *100*, 1189-1196.

[11] R. Taylor, D. R. Walton, *Nature,* **1993**, *363*, 685-693.

[12] E. T. Thostenson, Z. Ren, T.-W. Chou, *Composites science and technology,* **2001**, *61*, 1899-1912.

[13] W. S. Hummers Jr, R. E. Offeman, *Journal of the american chemical society,* **1958**, *80*, 1339-1339.

[14] C. Bao, L. Song, W. Xing, B. Yuan, C. A. Wilkie, J. Huang, Y. Guo, Y. Hu, *Journal of Material Chemistry,* **2012**, *22*, 6088-6096.

[15] M.-M. Titirici, R. J. White, N. Brun, V. L. Budarin, D. S. Su, F. del Monte, J. H. Clark, M. J. MacLachlan, *Chemical Society Reviews,* **2015**, *44*, 250-290.

[16] J. R. Holst, A. I. Cooper, Wiley Online Library, **2010**.

[17] L. Borchardt, M. Oschatz, S. Kaskel, *Materials Horizons* **2014**, *1*, 157-168.

[18] L. Dai, D. W. Chang, J. B. Baek, W. Lu, *small* **2012**, *8*, 1130-1166.

[19] S. H. Joo, S. J. Choi, I. Oh, J. Kwak, Z. Liu, O. Terasaki, R. Ryoo, *Nature,* **2001**, *412*, 169-172.

[20] Y. Liang, Y. Li, H. Wang, J. Zhou, J. Wang, T. Regier, H. Dai, *Nature materials,* **2011**, *10*, 780-786.

[21] R. E. Morris, P. S. Wheatley, *Angewandte Chemie Int. Ed.,* **2008**, *47*, 4966-4981.

[22] L. Wei, M. Sevilla, A. B. Fuertes, R. Mokaya, G. Yushin, *Advanced Energy Materials,* **2011**, *1*, 356-361.

[23] P. Zhang, J. Yuan, T. P. Fellinger, M. Antonietti, H. Li, Y. Wang, *Angewandte Chemie,* **2013**, *125*, 6144-6148.

[24] A. Ahmadpour, D. Do, *Carbon,* **1996**, *34*, 471-479.

[25] F. Rodríguez-Reinoso, *Handbook of porous solids,* **2002**, 1766-1827.

[26] M. Molina-Sabio, M. T. Gonzalez, F. Rodriguez-Reinoso, A. Sepúlveda-Escribano, *Carbon,* **1996**, *34*, 505-509.

[27] F. Caturla, M. Molina-Sabio, F. Rodríguez-Reinoso, *Carbon,* **1991**, *29*, 999-1007.

[28] J. Wang, S. Kaskel, *Journal of Material Chemistry,* **2012**, *22*, 23710-23725.

[29] T. Otowa, R. Tanibata, M. Itoh, *Gas separation & purification,* **1993**, *7*, 241-245.

[30] M. Molina-Sabio, F. Rodrıguez-Reinoso, *Colloids and Surfaces A: Physicochemical and Engineering Aspects,* **2004**, *241*, 15-25.

[31] K. Kaneko, *Journal of Membrane Science,* **1994**, *96*, 59-89.

[32] T. Kyotani, *Carbon,* **2000**, *38*, 269-286.

[33] M. Gilbert, J. Knox, B. Kaur, *Chromatographia,* **1982**, *16*, 138-146.

[34] C. G. Göltner, M. C. Weißenberger, *Acta Polymerica,* **1998**, *49*, 704-709.

[35] M. R. Benzigar, S. N. Talapaneni, S. Joseph, K. Ramadass, G. Singh, J. Scaranto, U. Ravon, K. Al-Bahily, A. Vinu, *Chemical Society Review,* **2018**, *47*, 2680-2721.

[36] J. Lee, J. Kim, T. Hyeon, *Advanced Materials,* **2006**, *18*, 2073-2094.

[37] X.-Y. Yang, L.-H. Chen, Y. Li, J. C. Rooke, C. Sanchez, B.-L. Su, *Chemical Society Review,* **2017**, *46*, 481-558.

[38] Y. Xia, Z. Yang, R. Mokaya, *Nanoscale* **2010**, *2*, 639-659.

[39] C. Liang, Z. Li, S. Dai, *Angewandte Chemie Int. Ed.,* **2008**, *47*, 3696-3717.

[40] H. Nishihara, T. Kyotani, *Advanced Materials,* **2012**, *24*, 4473-4498.

[41] F. Schüth, *Angewandte Chemie Int. Ed,* **2003**, *42*, 3604-3622.

[42] A.-H. Lu, F. Schüth, *Advanced Materials,* **2006**, *18*, 1793-1805.

[43] Z. Yang, Y. Lu, Z. Yang, *Chemical Communications,* **2009**, 2270-2277.

[44] R. Ryoo, S. H. Joo, S. Jun, *The Journal of Physical Chemistry B* **1999**, *103*, 7743-7746.

[45] T. Kyotani, T. Nagai, S. Inoue, A. Tomita, *Chemistry of Materials,* **1997**, *9*, 609-615.

[46] J. N. Hart, F. Claeyssens, N. L. Allan, P. W. May, *Physical Review B,* **2009**, *80*.

[47] H. Itoi, H. Nishihara, T. Kogure, T. Kyotani, *Journal of the American Chemical Society,* **2011**, *133*, 1165-1167.

[48] C. T. Kresge, M. E. Leonowicz, W. J. Roth, J. C. Vartuli, J. S. Beck, *Nature,* **1992**, *359*, 710-712.

[49] D. Zhao, J. Feng, Q. Huo, N. Melosh, G. H. Fredrickson, B. F. Chmelka, G. D. Stucky, *Science,* **1998**, *279*, 548-552.

[50] Y. Sakamoto, M. Kaneda, O. Terasaki, D. Y. Zhao, J. M. Kim, G. Stucky, H. J. Shin, R. Ryoo, *Nature,* **2000**, *408*, 449-453.

[51] R. Ryoo, J. M. Kim, C. H. Ko, C. H. Shin, *The Journal of Physical Chemistry,* **1996**, *100*, 17718-17721.

[52] C. Liang, K. Hong, G. A. Guiochon, J. W. Mays, S. Dai, *Angewandte Chemie Int. Ed.,* **2004**, *43*, 5785-5789.

[53] Y. Meng, D. Gu, F. Zhang, Y. Shi, H. Yang, Z. Li, C. Yu, B. Tu, D. Zhao, *Angewandte Chemie Int. Ed.,* **2005**, *44*, 7053-7059.

[54] C. Liang, S. Dai, *Journal of the American Chemical Society,* **2006**, *128*, 5316-5317.

[55] F. Zhang, Y. Meng, D. Gu, Yan, C. Yu, B. Tu, D. Zhao, *Journal of the American Chemical Society,* **2005**, *127*, 13508-13509.

[56] L. Chuenchom, R. Kraehnert, B. M. Smarsly, *Soft Matter,* **2012**, *8*, 10801-10812.

[57] F. Rodriguez-Reinoso, M. Molina-Sabio, M. Munecas, *The Journal of Physical Chemistry,* **1992**, *96*, 2707-2713.

[58] N. Fechler, T. P. Fellinger, M. Antonietti, *Advanced Matererials,* **2013**, *25*, 75-79.

[59] N. Díez, A. B. Fuertes, M. Sevilla, *Energy Storage Materials,* **2021**.

[60] J. Zhu, K. Sakaushi, G. Clavel, M. Shalom, M. Antonietti, T.-P. Fellinger, *Journal of the American Chemical Society,* **2015**, *137*, 5480-5485.

[61] X. Liu, N. Fechler, M. Antonietti, *Chemical Society Review,* **2013**, *42*, 8237-8265.

[62] R. Yan, M. Antonietti, M. Oschatz, *Advanced Energy Materials,* **2018**, *8*, 1800026.

[63] D. Yu, E. Nagelli, F. Du, L. Dai, *The Journal of Physical Chemistry Letters,* **2010**, *1*, 2165-2173.

[64] X. Wang, J. S. Lee, Q. Zhu, J. Liu, Y. Wang, S. Dai, *Chemistry of Materials,* **2010**, *22*, 2178-2180.

[65] Y. Shao, X. Wang, M. Engelhard, C. Wang, S. Dai, J. Liu, Z. Yang, Y. Lin, *J. Power Sources,* **2010**, *195*, 4375-4379.

[66] L. Zhao, L. Z. Fan, M. Q. Zhou, H. Guan, S. Qiao, M. Antonietti, M. M. Titirici, *Advanced Materials,* **2010**, *22*, 5202-5206.

[67] M. Sevilla, P. Valle-Vigón, A. B. Fuertes, *Advanced Functional Materials,* **2011**, *21*, 2781-2787.

[68] X. Hao, X. An, A. M. Patil, P. Wang, X. Ma, X. Du, X. Hao, A. Abudula, G. Guan, *ACS Applied Materials & Interfaces,* **2021**, *13*, 3738-3747.

[69] R. J. White, M. Antonietti, M.-M. Titirici, *Journal of Materials Chemistry,* **2009**, *19*, 8645-8650.

[70] X. Zhao, J. Zhu, L. Liang, C. Li, C. Liu, J. Liao, W. Xing, *Applied Catalysis B: Environmental,* **2014**, *154-155*, 177-182.

[71] J. Deng, M. Li, Y. Wang, *Green Chemistry* **2016**, *18*, 4824-4854.

[72] N.-L. Liu, S. Dutta, R. R. Salunkhe, T. Ahamad, S. M. Alshehri, Y. Yamauchi, C.-H. Hou, K. C.-W. Wu, *Scientific reports* **2016**, *6*, 1-7.

[73] K. Shen, X. Chen, J. Chen, Y. Li, *Acs Catalysis* **2016**, *6*, 5887-5903.

[74] J. Hwang, R. Walczak, M. Oschatz, N. V. Tarakina, B. V. Schmidt, *Small* **2019**, *15*, 1901986.

[75] Z. Xiang, D. Wang, Y. Xue, L. Dai, J.-F. Chen, D. Cao, *Scientific reports* **2015**, *5*, 1-8.

[76] K. Yuan, T. Hu, Y. Xu, R. Graf, L. Shi, M. Forster, T. Pichler, T. Riedl, Y. Chen, U. Scherf, *Materials Chemistry Frontiers* **2017**, *1*, 278-285.

[77] M. Inagaki, N. Ohta, Y. Hishiyama, *Carbon* **2013**, *61*, 1-21.

[78] J. Ding, Z. Li, K. Cui, S. Boyer, D. Karpuzov, D. Mitlin, *Nano Energy* **2016**, *23*, 129-137.

[79] L. Wei, M. Sevilla, A. B. Fuertes, R. Mokaya, G. Yushin, *Advanced Functional Materials* **2012**, *22*, 827-834.

[80] J. He, J. W. To, P. C. Psarras, H. Yan, T. Atkinson, R. T. Holmes, D. Nordlund, Z. Bao, J. Wilcox, *Advanced Energy Materials* **2016**, *6*, 1502491.

[81] J. W. To, Z. Chen, H. Yao, J. He, K. Kim, H.-H. Chou, L. Pan, J. Wilcox, Y. Cui, Z. Bao, *ACS central science* **2015**, *1*, 68-76.

[82] J. P. Paraknowitsch, A. Thomas, *Macromolecular Chemistry and Physics* **2012**, *213*, 1132-1145.

[83] S. Rondeau-Gagné, J.-F. Morin, *Chemical Society Reviews* **2014**, *43*, 85-98.

[84] W. Yang, T.-P. Fellinger, M. Antonietti, *Journal of the American Chemical Society* **2011**, *133*, 206-209.

[85] J. Maruyama, I. Abe, *Chemical Communications* **2007**, 2879-2881.

[86] J. Maruyama, N. Fukui, M. Kawaguchi, I. Abe, *J. Power Sources* **2009**, *194*, 655-661.

[87] J. S. Lee, X. Wang, H. Luo, S. Dai, *Advanced Materials* **2010**, *22*, 1004-1007.

[88] J. P. Paraknowitsch, J. Zhang, D. Su, A. Thomas, M. Antonietti, *Advanced Materials* **2010**, *22*, 87-92.

[89] Z. L. Xie, D. S. Su, *European Journal of Inorganic Chemistry* **2015**, *2015*, 1137-1147.

[90] S. Zhang, K. Dokko, M. Watanabe, *Materials Horizons* **2015**, *2*, 168-197.

[91] M. Inagaki, M. Toyoda, Y. Soneda, T. Morishita, *Carbon* **2018**, *132*, 104-140.

[92] Y. Deng, Y. Xie, K. Zou, X. Ji, *Journal of Materials Chemistry A* **2016**, *4*, 1144-1173.

[93] J. Liebig, *Annalen der Physik* **1834**, *107*, 321-336.

[94] M. L. Cohen, *Physical Review B* **1985**, *32*, 7988.

[95] X. Wang, K. Maeda, X. Chen, K. Takanabe, K. Domen, Y. Hou, X. Fu, M. Antonietti, *Journal of the American Chemical Society* **2009**, *131*, 1680-1681.

[96] X. Wang, K. Maeda, A. Thomas, K. Takanabe, G. Xin, J. M. Carlsson, K. Domen, M. Antonietti, *Nature Materials* **2009**, *8*, 76-80.

[97] S. Mazzanti, A. Savateev, *ChemPlusChem* **2020**, *85*, 2499 - 2517.

[98] L. Zhou, H. Zhang, H. Sun, S. Liu, M. O. Tade, S. Wang, W. Jin, *Catalysis Science & Technology* **2016**, *6*, 7002-7023.

[99] N. Rono, J. K. Kibet, B. S. Martincigh, V. O. Nyamori, *Critical Reviews in Solid State and Materials Sciences* **2020**, 1-29.

[100] Z. Zhao, Y. Sun, F. Dong, *Nanoscale* **2015**, *7*, 15-37.

[101] S. Muhl, J. M. Méndez, *Diamond Relatated Materials* **1999**, *8*, 1809-1830.

[102] A. Mishra, A. Mehta, S. Basu, N. P. Shetti, K. R. Reddy, T. M. Aminabhavi, *Carbon* **2019**, *149*, 693-721.

[103] N. Fechler, N. P. Zussblatt, R. Rothe, R. Schlögl, M.-G. Willinger, B. F. Chmelka, M. Antonietti, *Advanced Materials* **2016**, *28*, 1287-1294.

[104] J. Mahmood, E. K. Lee, M. Jung, D. Shin, I.-Y. Jeon, S.-M. Jung, H.-J. Choi, J.-M. Seo, S.-Y. Bae, S.-D. Sohn, N. Park, J. H. Oh, H.-J. Shin, J.-B. Baek, *Nature Communications* **2015**, *6*, 6486.

[105] Z. Tian, N. López-Salas, C. Liu, T. Liu, M. Antonietti, *Advanced Science*, *n/a*, 2001767.

[106] B. He, J. Shen, Z. Tian, *Physical Chemistry Chemical Physics* **2016**, *18*, 24261-24269.

[107] X. Li, W. Zhong, P. Cui, J. Li, J. Jiang, *The journal of physical chemistry letters* **2016**, *7*, 1750-1755.

[108] S. Tian, J. Wu, X. Zhang, K. K. Ostrikov, Z. Zhang, *Chemical Engineering Journal* **2020**, *380*, 122514.

[109] S. Hu, K. Xie, X. Zhang, S. Zhang, J. Gao, H. Song, D. Chen, *Chemical Engineering Journal* **2020**, *384*, 123317.

[110] A. Alabi, L. Cseri, A. Al Hajaj, G. Szekely, P. Budd, L. Zou, *Journal of Membrane Science* **2020**, *594*, 117457.

[111] Z. Tian, N. Fechler, M. Oschatz, T. Heil, J. Schmidt, S. Yuan, M. Antonietti, *Journal of Materials Chemistry A* **2018**, *6*, 19013-19019.

[112] R. Walczak, B. Kurpil, A. Savateev, T. Heil, J. Schmidt, Q. Qin, M. Antonietti, M. Oschatz, *Angewandte Chemie Int. Ed.* **2018**, *57*, 10765-10770.

[113] Z. Tian, F. Lai, T. Heil, S. Cao, M. Antonietti, *Science China Materials***2020**, *63*, 748-757.

[114] R. Yan, E. Josef, H. Huang, K. Leus, M. Niederberger, J. P. Hofmann, R. Walczak, M. Antonietti, M. Oschatz, *Advanced Functional Materials* **2019**, *29*, 1902858.

[115] R. Yan, K. Leus, J. P. Hofmann, M. Antonietti, M. Oschatz, *Nano Energy* **2020**, *67*, 104240.

[116] J. Xu, J. Mahmood, Y. Dou, S. Dou, F. Li, L. Dai, J. B. Baek, *Advanced Materials* **2017**, *29*, 1702007.

[117] S. S. Shinde, C. H. Lee, J.-Y. Yu, D.-H. Kim, S. U. Lee, J.-H. Lee, *ACS Nano* **2018**, *12*, 596-608.

[118] Z. Guan, C.-S. Lian, S. Hu, S. Ni, J. Li, W. Duan, *The Journal of Physical Chemistry C* **2017**, *121*, 3654-3660.

[119] S. Yang, W. Li, C. Ye, G. Wang, H. Tian, C. Zhu, P. He, G. Ding, X. Xie, Y. Liu, *Advanced Materials* **2017**, *29*, 1605625.

[120] T. C. King, P. D. Matthews, J. P. Holgado, D. A. Jefferson, R. M. Lambert, A. Alavi, D. S. Wright, *Carbon* **2013**, *64*, 6-10.

[121] X. Li, L. Zhu, Q. Xue, X. Chang, C. Ling, W. Xing, *ACS Applied Materials & Interfaces* **2017**, *9*, 31161-31169.

[122] X. Ma, L. Li, Z. Zeng, R. Chen, C. Wang, K. Zhou, C. Su, H. Li, *Chemical Engineering Journal* **2019**, *363*, 49-56.

[123] W. Xu, C. Chen, C. Tang, Y. Li, L. Xu, *Scientific Reports* **2018**, *8*, 5661.

[124] Y. Zhou, G. Gao, J. Kang, W. Chu, L.-W. Wang, *Journal of Materials Chemistry A* **2019**, *7*, 12050-12059.

[125] J. Xu, J. Mahmood, Y. Dou, S. Dou, F. Li, L. Dai, J.-B. Baek, *Advanced Materials* **2017**, *29*, 1702007.

[126] L. Tan, C. Nie, Z. Ao, H. Sun, T. An, S. Wang, *Journal of Materials Chemistry A* **2021**, *9*, 17-33.

[127] J. Wang, X. Li, Y. You, X. Yang, Y. Wang, Q. Li, *Nanotechnology* **2018**, *29*, 365401.

[128] Y. Xu, H. Xu, L. Wang, J. Yan, H. Li, Y. Song, L. Huang, G. Cai, *Dalton Transactions* **2013**, *42*, 7604-7613.

[129] J. Zhang, T. Xu, D. Yuan, J. Tian, D. Ma, *Journal of CO2 Utilization* **2021**, *43*, 101367.

[130] A. Bafekry, M. Ghergherehchi, S. F. Shayesteh, F. Peeters, *Chemical Physics* **2019**, *526*, 110442.

[131] J. Partington, in *A History of Chemistry*, Springer, **1964**, pp. 233-264.

[132] G. Gay-Lussac, *Ann. Phys.* **1816**, *53*, 1-62.

[133] H. Delbrück, *Journal für Praktische Chemie* **1847**, *41*, 161-180.

[134] L. Bircumshaw, F. Tayler, D. Whiffen, *Journal of the Chemical Society (Resumed)* **1954**, 931-935.

[135] J. Chen, M. Labes, *Macromolecules* **1986**, *19*, 1528-1530.

[136] J. Chen, M. Labes, *Macromolecules* **1985**, *18*, 827-828.

[137] J. Chen, M. Labes, *Journal of Polymer Science: Polymer Chemistry Edition* **1985**, *23*, 517-523.

[138] M. M. Labes, J. H. Chen*, Vol. 4649038*, Temple University (Philadelphia, PA) United States, **1987**.

[139] J. Li, C. Cao, J. Hao, H. Qiu, Y. Xu, H. Zhu, *Diamond Relatated Materials* **2006**, *15*, 1593-1600.

[140] H. Yin, Q. Guo, D. He, J. Li, S. Sun, *RSC Advances* **2017**, *7*, 44001-44008.

[141] J. Feng, M. Li, *Advanced Functional Materials* **2020**, *30*, 2001502.

[142] J. Zeng, Z. Chen, X. Zhao, W. Yu, S. Wu, J. Lu, K. P. Loh, J. Wu, *ACS Applied Nano Materials* **2019**, *2*, 7969-7977.

[143] R. Walczak, A. Savateev, J. Heske, N. V. Tarakina, S. Sahoo, J. D. Epping, T. D. Kühne, B. Kurpil, M. Antonietti, M. Oschatz, *Sustainable Energy & Fuels* **2019**, *3*, 2819-2827.

[144] M. Oschatz, M. Antonietti, *Energy & Environmental Science* **2018**, *11*, 57-70.

[145] G.-P. Hao, W.-C. Li, S. Wang, S. Zhang, A.-H. Lu, *Carbon* **2010**, *48*, 3330-3339.

[146] L. Li, P. A. Quinlivan, D. R. Knappe, *Carbon* **2002**, *40*, 2085-2100.

[147] Global Carbon Project. (12. Dezember, **2020**.

[148] B. Dutcher, M. Fan, A. G. Russell, *ACS applied materials & interfaces* **2015**, *7*, 2137-2148.

[149] C. Gouedard, D. Picq, F. Launay, P.-L. Carrette, *International Journal of Greenhouse Gas Control* **2012**, *10*, 244-270.

[150] Q. Wang, J. Luo, Z. Zhong, A. Borgna, *Energy & Environmental Science* **2011**, *4*, 42-55.

[151] S. M. Auerbach, K. A. Carrado, P. K. Dutta, *Handbook of zeolite science and technology*, CRC press, **2003**.

[152] Y. Belmabkhout, V. Guillerm, M. Eddaoudi, *Chemical Engineering Journal* **2016**, *296*, 386-397.

[153] P. Nugent, Y. Belmabkhout, S. D. Burd, A. J. Cairns, R. Luebke, K. Forrest, T. Pham, S. Ma, B. Space, L. Wojtas, M. Eddaoudi, M. J. Zaworotko, *Nature* **2013**, *495*, 80-84.

[154] Y. Zhao, L. Zhao, K. X. Yao, Y. Yang, Q. Zhang, Y. Han, *Journal of Materials Chemistry* **2012**, *22*, 19726-19731.

[155] Y. Zhao, X. Liu, K. X. Yao, L. Zhao, Y. Han, *Chemistry of Materials* **2012**, *24*, 4725-4734.

[156] J. Wei, D. Zhou, Z. Sun, Y. Deng, Y. Xia, D. Zhao, *Advanced Functional Materials* **2013**, *23*, 2322-2328.

[157] X. Fan, L. Zhang, G. Zhang, Z. Shu, J. Shi, *Carbon* **2013**, *61*, 423-430.

[158] X. Ma, M. Cao, C. Hu, *Journal of Materials Chemistry A* **2013**, *1*, 913-918.

[159] J. Gong, H. Lin, M. Antonietti, J. Yuan, *Journal of Materials Chemistry A* **2016**, *4*, 7313-7321.

[160] M. Sevilla, J. B. Parra, A. B. Fuertes, *ACS applied materials & interfaces* **2013**, *5*, 6360-6368.

[161] L. Wang, R. T. Yang, *The Journal of Physical Chemistry C* **2012**, *116*, 1099-1106.

[162] K. V. Kumar, K. Preuss, L. Lu, Z. X. Guo, M. M. Titirici, *The Journal of Physical Chemistry C* **2015**, *119*, 22310-22321.

[163] A. Muelleman, J. Schell, S. Glazer, R. Glaser, *C* **2016**, *2*, 18.

[164] L. Pérez-Lombard, J. Ortiz, C. Pout, *Energy and buildings* **2008**, *40*, 394-398.

[165] C. A. Balaras, G. Grossman, H.-M. Henning, C. A. I. Ferreira, E. Podesser, L. Wang, E. Wiemken, *Renewable and sustainable energy reviews* **2007**, *11*, 299-314.

[166] A. Karmakar, V. Prabakaran, D. Zhao, K. J. Chua, *Applied Energy* **2020**, *269*, 115070.

[167] C. Janiak, S. K. Henninger, *CHIMIA International Journal for Chemistry* **2013**, *67*, 419-424.

[168] J. Ehrenmann, S. K. Henninger, C. Janiak, *European Journal of Inorganic Chemistry* **2011**, *2011*, 471-474.

[169] F. Jeremias, D. Fröhlich, C. Janiak, S. K. Henninger, *New Journal of Chemistry* **2014**, *38*, 1846-1852.

[170] M. Sohail, Y.-N. Yun, E. Lee, S. K. Kim, K. Cho, J.-N. Kim, T. W. Kim, J.-H. Moon, H. Kim, *Crystal Growth & Design* **2017**, *17*, 1208-1213.

[171] B. Dawoud, Y. Aristov, *Int. J. Heat Mass Transfer* **2003**, *46*, 273-281.

[172] S. K. Henninger, F. Jeremias, H. Kummer, P. Schossig, H.-M. Henning, *Energy Procedia* **2012**, *30*, 279-288.

[173] S. Izmailova, E. Vasiljeva, I. Karetina, N. Feoktistova, S. Khvoshchev, *Journal of Colloid and Interface Science* **1996**, *179*, 374-379.

[174] H. Pastore, S. Coluccia, L. Marchese, *Annual Review of Materials Research* **2005**, *35*, 351-395.

[175] X. Liu, X. Wang, F. Kapteijn, *Chemical Reviews* **2020**, *120*, 8303-8377.

[176] A. Khutia, H. U. Rammelberg, T. Schmidt, S. Henninger, C. Janiak, *Chemistry of Materials* **2013**, *25*, 790-798.

[177] S. M. Towsif Abtab, D. Alezi, P. M. Bhatt, A. Shkurenko, Y. Belmabkhout, H. Aggarwal, Ł. J. Weseliński, N. Alsadun, U. Samin, M. N. Hedhili, M. Eddaoudi, *Chem* **2018**, *4*, 94-105.

[178] F. Jeremias, A. Khutia, S. K. Henninger, C. Janiak, *Journal of Materials Chemistry,* **2012**, *22*, 10148-10151.

[179] D. J. Miles, S. V. Shelton, *Applied Thermal Engineering* **1996**, *16*, 389-394.

[180] L. Gordeeva, Y. Aristov, *Applied Energy* **2014**, *117*, 127-133.

[181] C. S. Dewey, P. K. Lefforge, G. L. Cabot, *Industrial & Engineering Chemistry* **1932**, *24*, 1045-1050.

[182] J. W. McBain, J. Porter, R. Sessions, *Journal of the American Chemical Society* **1933**, *55*, 2294-2304.

[183] L. Liu, S. Tan, T. Horikawa, D. D. Do, D. Nicholson, J. Liu, *Adv. Colloid Interface Science* **2017**, *250*, 64-78.

[184] E.-P. Ng, S. Mintova, *Microporous Mesoporous Materials* **2008**, *114*, 1-26.

[185] M. Thommes, J. r. Morell, K. A. Cychosz, M. Fröba, *Langmuir* **2013**, *29*, 14893-14902.

[186] D. Wang, C. Ao, X. Liu, S. Fang, Y. Lin, W. Liu, W. Zhang, X. Zheng, L. Zhang, T. Yao, *ACS Applied Energy Materials* **2019**, *2*, 6497-6504.

[187] F. Li, G.-F. Han, H.-J. Noh, S.-J. Kim, Y. Lu, H. Y. Jeong, Z. Fu, J.-B. Baek, *Energy & Environmental Science* **2018**, *11*, 2263-2269.

[188] H. A. Gasteiger, S. S. Kocha, B. Sompalli, F. T. Wagner, *Applied Catalysis B: Environmental* **2005**, *56*, 9-35.

[189] J. Greeley, I. Stephens, A. Bondarenko, T. P. Johansson, H. A. Hansen, T. Jaramillo, J. Rossmeisl, I. Chorkendorff, J. K. Nørskov, *Nature chemistry* **2009**, *1*, 552-556.

[190] C. Cui, L. Gan, M. Heggen, S. Rudi, P. Strasser, *Nature materials* **2013**, *12*, 765-771.

[191] L. Cui, L. Cui, Z. Li, J. Zhang, H. Wang, S. Lu, Y. Xiang, *Journal of Materials Chemistry A* **2019**, *7*, 16690-16695.

[192] S. Mondal, C. R. Raj, *The Journal of Physical Chemistry C* **2018**, *122*, 18468-18475.

[193] L. Dai, Y. Xue, L. Qu, H.-J. Choi, J.-B. Baek, *Chemical Reviews* **2015**, *115*, 4823-4892.

[194] G. Wu, P. Zelenay, *Accounts of Chemical Research* **2013**, *46*, 1878-1889.

[195] M. K. Debe, *Nature* **2012**, *486*, 43-51.

[196] K. Gong, F. Du, Z. Xia, M. Durstock, L. Dai, *Sci. Technol. Weld. Joining* **2009**, *323*, 760-764.

[197] H.-W. Liang, X. Zhuang, S. Brüller, X. Feng, K. Müllen, *Nature communications* **2014**, *5*, 1-7.

[198] J. Duan, S. Chen, M. Jaroniec, S. Z. Qiao, *Acs Catalysis* **2015**, *5*, 5207-5234.

[199] Y. Jiao, Y. Zheng, M. Jaroniec, S. Z. Qiao, *Chemical Society Reviews* **2015**, *44*, 2060-2086.

[200] D.-W. Wang, D. Su, *Energy & Environmental Science* **2014**, *7*, 576-591.

[201] X. Ge, A. Sumboja, D. Wuu, T. An, B. Li, F. T. Goh, T. A. Hor, Y. Zong, Z. Liu, *Acs Catalysis* **2015**, *5*, 4643-4667.

[202] E. Chen, M. Bevilacqua, C. Tavagnacco, T. Montini, C.-M. Yang, P. Fornasiero, *Catal. Today* **2019**.

[203] C. Zhu, Q. Shi, B. Z. Xu, S. Fu, G. Wan, C. Yang, S. Yao, J. Song, H. Zhou, D. Du, S. P. Beckman, D. Su, Y. Lin, *Advanced Energy Materials* **2018**, *8*, 1801956.

[204] H. Terrones, R. Lv, M. Terrones, M. S. Dresselhaus, *Reports on Progress in Physics* **2012**, *75*, 062501.

[205] S. Campisi, C. E. Chan-Thaw, A. Villa, *Applied Sciences* **2018**, *8*, 1159.

[206] M. B. Gawande, P. Fornasiero, R. Zbořil, *ACS Catalysis* **2020**, *10*, 2231-2259.

[207] S. Mitchell, E. Vorobyeva, J. Pérez-Ramírez, *Angewandte Chemie Int. Ed.* **2018**, *57*, 15316-15329.

[208] Z. Li, S. Ji, Y. Liu, X. Cao, S. Tian, Y. Chen, Z. Niu, Y. Li, *Chemical Reviews* **2020**, *120*, 623-682.

[209] L. Liu, A. Corma, *Chemical Reviews* **2018**, *118*, 4981-5079.

[210] T. W. van Deelen, C. H. Mejía, K. P. de Jong, *Nature Catalysis* **2019**, *2*, 955-970.

[211] D. W. Ma, Q. Wang, X. Yan, X. Zhang, C. He, D. Zhou, Y. Tang, Z. Lu, Z. Yang, *Carbon* **2016**, *105*, 463-473.

[212] X. Cui, W. An, X. Liu, H. Wang, Y. Men, J. Wang, *Nanoscale* **2018**, *10*, 15262-15272.

[213] X. Zhang, A. Chen, Z. Zhang, M. Jiao, Z. Zhou, *Journal of Materials Chemistry A* **2018**, *6*, 11446-11452.

[214] G. Han, Y. Zheng, X. Zhang, Z. Wang, Y. Gong, C. Du, M. N. Banis, Y.-M. Yiu, T.-K. Sham, L. Gu, Y. Sun, Y. Wang, J. Wang, Y. Gao, G. Yin, X. Sun, *Nano Energy* **2019**, *66*, 104088.

[215] Y. Wang, R. Shi, L. Shang, G. I. Waterhouse, J. Zhao, Q. Zhang, L. Gu, T. Zhang, *Angewandte Chemie Int. Ed.* **2020**, *59*, 13057-13062.

[216] X. Song, N. Li, H. Zhang, L. Wang, Y. Yan, H. Wang, L. Wang, Z. Bian, *ACS Applied Materials & Interfaces* **2020**, *12*, 17519-17527.

[217] K. Iwase, T. Yoshioka, S. Nakanishi, K. Hashimoto, K. Kamiya, *Angewandte Chemie Int. Ed.* **2015**, *54*, 11068-11072.

[218] H. Wu, H. Li, X. Zhao, Q. Liu, J. Wang, J. Xiao, S. Xie, R. Si, F. Yang, S. Miao, X. Guo, G. Wang, X. Bao, *Energy & Environmental Science* **2016**, *9*, 3736-3745.

[219] Y. M. Zhao, G. Q. Yu, F. F. Wang, P. J. Wei, J. G. Liu, *Chemistry–A European Journal* **2019**, *25*, 3726-3739.

[220] A. Bhagi-Damodaran, M. A. Michael, Q. Zhu, J. Reed, B. A. Sandoval, E. N. Mirts, S. Chakraborty, P. Moënne-Loccoz, Y. Zhang, Y. Lu, *Nature chemistry* **2017**, *9*, 257-263.

[221] E. I. Solomon, D. E. Heppner, E. M. Johnston, J. W. Ginsbach, J. Cirera, M. Qayyum, M. T. Kieber-Emmons, C. H. Kjaergaard, R. G. Hadt, L. Tian, *Chemical Reviews* **2014**, *114*, 3659-3853.

[222] W. He, C. Jiang, J. Wang, L. Lu, *Angewandte Chemie***2014**, *126*, 9657-9661.

[223] H. Kohlmann, *European Journal of Inorganic Chemistry* **2019**, *2019*, 4174-4180.

[224] K. Sakaushi, S. J. Yang, T. P. Fellinger, M. Antonietti, *Journal of Materials Chemistry A* **2015**, *3*, 11720-11724.

[225] K. Elumeeva, N. Fechler, T.-P. Fellinger, M. Antonietti, *Materials Horizons* **2014**, *1*, 588-594.

[226] J. Shui, M. Wang, F. Du, L. Dai, *Science advances* **2015**, *1*, e1400129.

[227] J. Pampel, T.-P. Fellinger, *Advanced Energy Materials* **2016**, *6*, 1502389.

[228] J. Zhang, Z. Zhao, Z. Xia, L. Dai, *Nature nanotechnology* **2015**, *10*, 444-452.

[229] L. Li, A. Manthiram, *Advanced Energy Materials* **2014**, *4*, 1301795.

[230] J. Shui, F. Du, C. Xue, Q. Li, L. Dai, *ACS nano* **2014**, *8*, 3015-3022.

[231] Z. H. Xue, J. T. Han, W. J. Feng, Q. Y. Yu, X. H. Li, M. Antonietti, J. S. Chen, *Angewandte Chemie***2018**, *130*, 2727-2731.

[232] Y. Wang, J. Yao, H. Li, D. Su, M. Antonietti, *Journal of the American Chemical Society* **2011**, *133*, 2362-2365.

[233] J. Pampel, A. Mehmood, M. Antonietti, T. P. Fellinger, *Materials Horizons* **2017**, *4*, 493-501.

[234] S. Lin, Y. Zhang, W. Cao, X. Wang, L. Qin, M. Zhou, H. Wei, *Dalton Transactions* **2019**, *48*, 1993-1999.

[235] S. O. Kang, J. M. Llinares, V. W. Day, K. Bowman-James, *Chemical Society Reviews* **2010**, *39*, 3980-4003.

[236] P. Kuhn, A. Forget, D. Su, A. Thomas, M. Antonietti, *Journal of the American Chemical Society* **2008**, *130*, 13333-13337.

[237] G. Tuci, M. Pilaski, H. Ba, A. Rossin, L. Luconi, S. Caporali, C. Pham-Huu, R. Palkovits, G. Giambastiani, *Advanced Functional Materials* **2017**, *27*, 1605672.

[238] O. Buyukcakir, S. H. Je, S. N. Talapaneni, D. Kim, A. Coskun, *ACS Applied Materials & Interfaces* **2017**, *9*, 7209-7216.

[239] P. Kuhn, M. Antonietti, A. Thomas, *Angewandte Chemie Int. Ed. Engl.* **2008**, *47*, 3450-3453.

[240] X. Wang, K. Maeda, A. Thomas, K. Takanabe, G. Xin, J. M. Carlsson, K. Domen, M. Antonietti, *Nature Materials* **2008**, *8*, 76.

[241] X. Ren, H. Li, J. Chen, L. Wei, A. Modak, H. Yang, Q. Yang, *Carbon* **2017**, *114*, 473-481.

[242] Y. K. Kim, G. M. Kim, J. W. Lee, *Journal of Materials Chemistry A* **2015**, *3*, 10919-10927.

[243] S. K. Das, X. Wang, M. M. Ostwal, Z. Lai, *Separation and Purification Technology* **2016**, *170*, 68-77.

[244] M. Saleh, S. B. Baek, H. M. Lee, K. S. Kim, *The Journal of Physical Chemistry C* **2015**, *119*, 5395-5402.

[245] J. Gong, M. Antonietti, J. Yuan, *Angewandte Chemie Int. Ed.* **2017**, *56*, 7557-7563.

[246] T. D. Kühne, M. Krack, F. R. Mohamed, M. Parrinello, *Physical Review Letters* **2007**, *98*, 066401.

[247] T. D. Kühne, M. Iannuzzi, M. D. Ben, V. V. Rybkin, P. Seewald, F. Stein, T. Laino, R. Z. Khaliullin, O. Schütt, F. Schiffmann, D. Golze, J. Wilhelm, S. Chulkov, M. H. Bani-Hashemian, V. Weber, U. Borštnik, M. Taillefumier, A. S. Jakobovits, A. Lazzaro, H. Pabst, T. Müller, R. Schade, M. Guidon, S. Andermatt, N. Holmberg, G. K. Schenter, A. Hehn, A. Bussy, F. Belleflamme, G. Tabacchi, A. Glöß, M. Lass, I. Bethune, C. J. Mundy, C. Plessl, M. Watkins, J. VandeVondele, M. Krack, J. Hutter, *The Journal of Chemical Physics* **2020**, *152*, 194103.

[248] L. Zhu, Q. Xue, X. Li, T. Wu, Y. Jin, W. Xing, *Journal of Materials Chemistry A* **2015**, *3*, 21351-21356.

[249] R. C. Dante, P. Martín-Ramos, P. Chamorro-Posada, S. Meejoo-Smith, J. Vázquez-Cabo, Ó. Rubiños-López, L. Lartundo-Rojas, F. M. Sánchez-Árevalo, J. Trakulmututa, D. Rutto, *Material Chemical Physics* **2019**, *221*, 397-408.

[250] K. V. Kumar, K. Preuss, Z. X. Guo, M. M. Titirici, *The Journal of Physical Chemistry C* **2016**, *120*, 18167-18179.

[251] T. Ivanova, K. Maslakov, A. Sidorov, M. Kiskin, R. Linko, S. Savilov, V. Lunin, I. Eremenko, *Journal of Electron Spectroscopy and Related Phenomena* **2020**, *238*, 146878.

[252] G. Speier, Z. Tyeklar, P. Toth, E. Speier, S. Tisza, A. Rockenbauer, A. Whalen, N. Alkire, C. Pierpont, *Inorganic chemistry* **2001**, *40*, 5653-5659.

[253] S. Haaf, E. Kaifer, H. Wadepohl, H.-J. Himmel, *Chemistry – A European Journal* **2021**, *27*, 959-970.

[254] C. C. McCrory, X. Ottenwaelder, T. D. P. Stack, C. E. Chidsey, *The Journal of Physical Chemistry A* **2007**, *111*, 12641-12650.

[255] M. Langerman, D. G. Hetterscheid, *Angewandte Chemie Int. Ed.* **2019**, *58*, 12974-12978.

[256] M. Thommes, K. Kaneko, A. V. Neimark, J. P. Olivier, F. Rodriguez-Reinoso, J. Rouquerol, K. S. W. Sing, *Pure Applied Chemistry* **2015**, *87*, 1051-1069.

[257] F. Rouquerol, J. Rouquerol, K. S. Sing, P. Llewellyn, G. Maurin, **2014**.

[258] V. Cornette, J. Villarroel-Rocha, K. Sapag, R. Delgado Mons, J. P. Toso, R. H. López, *Carbon* **2020**, *168*, 508-514.

[259] M. Thompson, *Handbook of inductively coupled plasma spectrometry*, Springer Science & Business Media, **2012**.

[260] J. W. To, J. He, J. Mei, R. Haghpanah, Z. Chen, T. Kurosawa, S. Chen, W.-G. Bae, L. Pan, J. B.-H. Tok, *Journal of the American Chemical Society* **2016**, *138*, 1001-1009.

[261] S. N. Talapaneni, J. H. Lee, S. H. Je, O. Buyukcakir, T. w. Kwon, K. Polychronopoulou, J. W. Choi, A. Coskun, *Advanced Functional Materials* **2017**, *27*, 1604658.

[262] G.-P. Hao, W.-C. Li, D. Qian, G.-H. Wang, W.-P. Zhang, T. Zhang, A.-Q. Wang, F. Schüth, H.-J. Bongard, A.-H. Lu, *Journal of the American Chemical Society* **2011**, *133*, 11378-11388.

[263] Y. Zhao, K. X. Yao, B. Teng, T. Zhang, Y. Han, *Energy & Environmental Science* **2013**, *6*, 3684-3692.

[264] Y.-J. Heo, S.-J. Park, *Green chemistry* **2018**, *20*, 5224-5234.

[265] S. Gu, J. Guo, Q. Huang, J. He, Y. Fu, G. Kuang, C. Pan, G. Yu, *Macromolecules* **2017**, *50*, 8512-8520.

[266] S. K. Das, X. Wang, M. M. Ostwal, Y. Zhao, Y. Han, Z. Lai, *Chemical Engineering Science* **2016**, *145*, 21-30.

[267] X. Zhu, C. Tian, G. M. Veith, C. W. Abney, J. r. m. Dehaudt, S. Dai, *Journal of the American Chemical Society* **2016**, *138*, 11497-11500.

[268] N. D. Shcherban, P. Mäki-Arvela, A. Aho, S. A. Sergiienko, P. S. Yaremov, K. Eränen, D. Y. Murzin, *Catalysis Science & Technology* **2018**, *8*, 2928-2937.

[269] B. Mi, X. Chen, C. Jiang, J. Wang, X. Chen, B. Zhang, X. Liu, Z. Liu, B. Fei, *Catalysts* **2018**, *8*, 232.

[270] H. Kaper, A. Grandjean, C. Weidenthaler, F. Schüth, F. Goettmann, *Chemistry – A European Journal* **2012**, *18*, 4099-4106.

[271] R. Demir-Cakan, P. Makowski, M. Antonietti, F. Goettmann, M. M. Titirici, *Catal. Today* **2010**, *150*, 115-118.

[272] F. Su, M. Antonietti, X. Wang, *Catalysis Science and Technology* **2012**, *2*, 1005-1009.

[273] S.-i. Fujita, A. Katagiri, H. Watanabe, S. Asano, H. Yoshida, M. Arai, *ChemCatChem* **2015**, *7*, 2965-2970.

[274] R. Walczak, B. Kurpil, A. Savateev, T. Heil, J. Schmidt, Q. Qin, M. Antonietti, M. Oschatz, *Angew Chem Int Ed Engl* **2018**, *57*, 10765-10770.

[275] T. Horikawa, N. Sakao, T. Sekida, J. i. Hayashi, D. D. Do, M. Katoh, *Carbon* **2012**, *50*, 1833-1842.

[276] E. Zhang, G.-P. Hao, M. E. Casco, V. Bon, S. Grätz, L. Borchardt, *Journal of Materials Chemistry A* **2018**, *6*, 859-865.

[277] G. P. Hao, G. Mondin, Z. Zheng, T. Biemelt, S. Klosz, R. Schubel, A. Eychmüller, S. Kaskel, *Angewandte Chemie Int. Ed.* **2015**, *54*, 1941-1945.

[278] L. Huber, P. Ruch, R. Hauert, S. K. Matam, G. Saucke, S. Yoon, Y. Zhang, M. M. Koebel, *RSC Advances* **2016**, *6*, 80729-80738.

[279] L. Huber, P. Ruch, R. Hauert, G. Saucke, S. K. Matam, B. Michel, M. M. Koebel, *RSC Advances* **2016**, *6*, 25267-25278.

[280] J. Fujiki, K. Yogo, *Applied Surface Science* **2019**, *492*, 776-784.

[281] M. Yuan, M. Gao, Q. Shi, J. Dong, *Chemical Engineering Journal* **2020**, *379*.

[282] L. Huber, S. B. Hauser, E. Brendlé, P. Ruch, J. Ammann, R. Hauert, R. N. Widmer, C. J. Ubert, S. K. Matam, S. Yoon, Y. Zhang, M. M. Koebel, *Microporous and Mesoporous Materials* **2019**, *276*, 239-250.

[283] S. Gadipelli, C. A. Howard, J. Guo, N. T. Skipper, H. Zhang, P. R. Shearing, D. J. L. Brett, *Advanced Energy Materials* **2020**, *10*.

[284] M. Thommes, J. Morell, K. A. Cychosz, M. Froba, *Langmuir* **2013**, *29*, 14893-14902.

[285] M. Nakamura, T. Ohba, P. Branton, H. Kanoh, K. Kaneko, *Carbon* **2010**, *48*, 305-308.

[286] B. P. Biswal, S. Kandambeth, S. Chandra, D. B. Shinde, S. Bera, S. Karak, B. Garai, U. K. Kharul, R. Banerjee, *Journal of Materials Chemistry A* **2015**, *3*, 23664-23669.

[287] S. Hug, L. Stegbauer, H. Oh, M. Hirscher, B. V. Lotsch, *Chemistry of Materials* **2015**, *27*, 8001-8010.

[288] A. J. Rieth, S. Yang, E. N. Wang, M. Dinca, *ACS Central Science* **2017**, *3*, 668-672.

[289] Y. Qu, Z. Li, W. Chen, Y. Lin, T. Yuan, Z. Yang, C. Zhao, J. Wang, C. Zhao, X. Wang, F. Zhou, Z. Zhuang, Y. Wu, Y. Li, *Nature Catalysis* **2018**, *1*, 781-786.

[290] Z. Yang, B. Chen, W. Chen, Y. Qu, F. Zhou, C. Zhao, Q. Xu, Q. Zhang, X. Duan, Y. Wu, *Nature Communications* **2019**, *10*, 3734.

8. Appendix

8.1 List of Abbreviations

(HR)TEM	(high-resolution) transmission electron microscopy
AHP	adsorption hat pump
at%	atomic percentage
BET	Brunauer–Emmett–Teller method
BJH	Barrett-Joyner-Halenda
BTCN	1-Butyl-4-methylpyridinium tricyanomethanide
CMK	carbon mesostructured by KAIST
CTF	covalent triazine framework
CV	cyclo voltammetry
DTA	differential thermal analysis
EA	elemental analysis
EDX	energy dispersive X-ray spectroscopy
EELS	electron energy loss spectroscopy
FC	fuel cell
FFT	fast fourier transform
FTIR	fourier-transform infrared spectroscopy
HAADF-STEM	high-angular annular-dark field scanning electron microscopy
HER	hydrogen evolution reaction
ICP-OES	inductively coupled plasma – optical emission spectrometry
IL	ionic liquid
IUPAC	international Union of Pure and Applied Chemistry
LSV	linear sweep voltammetry
MOF	metal-organic framework
µm	micrometer
MPIKG	Max-Planck-Institut für Kolloid- und Grenzflächenforschung

NC	nitrogen-doped carbon
NLDFT	nonlocal density functional theory
nm	nanometer
OER	oxygen evolution reaction
ORR	oxygen reduction reaction
PEMFC	polymer electrolyte fuel cell
PSD	pore size distribution
PXRD	powder X-ray diffraction
QSDFT	quenched-solid density functional theory
Q_{st}	specific heat of adsorption
RDE	rotating disc electrode
RHE	reversible hydrogen electrode
RRDE	rotating ring disc electrode
SE-STEM	secondary electron scanning electron microscopy
SEM	scanning electron microscopy
SSA	specific surface area
(ss)NMR	(solid state) nuclear magnetic resonance
STEM	scanning transmission electron microscopy
SZ	$NaCl/ZnCl_2$
TDC	thermally driven adsorption chillers
TGA-MS	thermogravimetric analysis - coupled with mass spectrometry
TPD	temperature programmed desorption
V_{meso}	mesopore volume
V_{micro}	micropore volume
V_t	total pore volume
wt%	weight percentage
XPS	X-ray photoelectron spectroscopy

8.2 Applied Methods

Gas/Vapor Physisorption Measurements

The term adsorption, in general, describes the enrichment of one or more components at the interface between a solid (the adsorbent) and a fluid. The fluid in the free state is called adsorptive and in the adsorbed state adsorbate. In general, it is distinguished between chemisorption and physisorption. With chemisorption, the formation of covalent bonds takes place and thus a higher enthalpy is involved. Physisorption involves attractive dispersion forces, short-range repulsive forces, and specific molecular interactions. Physisorption is widely used as an analytical tool for the characterization of porous solids and powders.

Nitrogen and Argon Physisorption

Commonly, nitrogen is used as test gas and measured at 77 K and atmospheric pressure, ensuring weak van der Waals interactions and enables multilayer formation. This allows the qualitative and quantitative determination of the surface area, pore volume, and pore size. In a typical measurement, the adsorbate is dosed into a sample cell and the gas uptake is recorded in dependence of the relative pressure. The relative pressure is increased up to $p/p_0=1$ to obtain the adsorption isotherm and then the pressure is lowered to get the desorption isotherm. The obtained isotherms are classified according to IUPAC recommendations[256] and the types give information about the pore size of the material with:

micropores < 2nm, 2 nm > mesopores < 50 nm, macropores > 50 nm

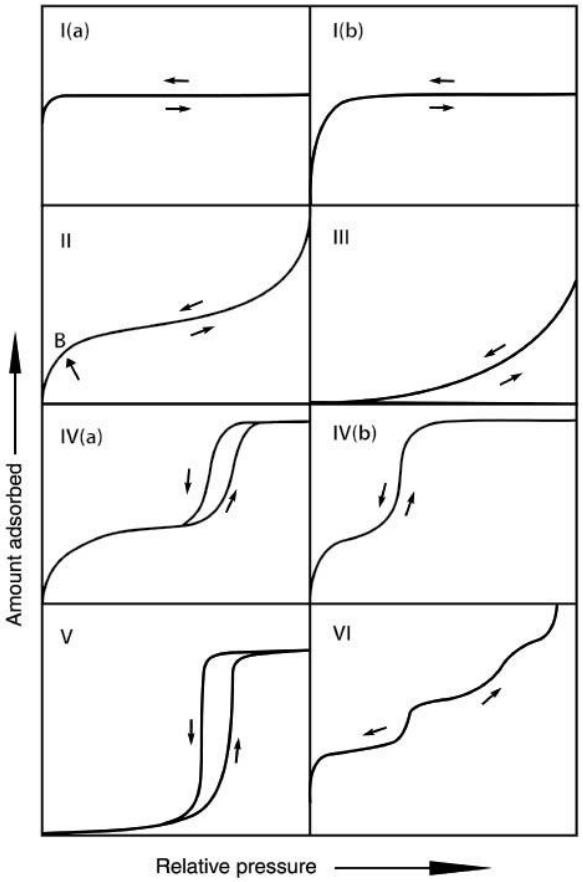

Figure A1. Classification of physisorption isotherms according to IUPAC recommendations (®De Gruyter, 2015[256]).

Figure A1 shows the different isotherms. A type I isotherm is typical for microporous materials with subdivision into type I(a) for the filling of ultramicropores (approximately < 0.7 nm) and type I(b) for supermicropores (0.7 – 2 nm). The steep uptake at low relative pressures is a consequence of enhanced solid-gas interactions in the micropores. A type II isotherm can be seen for non-porous or macroporous materials. It shows unrestricted monolayer-multilayer adsorption up to high relative pressures. Point B describes the point when the monolayer is completed. If this point is more gradual, a simultaneous monolayer and multilayer formation takes place. Type III isotherms occur if a weak adsorbent-adsorbate interaction is present. The adsorption is based on clustering of the adsorbate around favorable sites on the surface. Mesoporous materials show type IV isotherms. A subdivision is made depending on the presence

of a hysteresis. If a hysteresis is present it is a type IV(a) isotherm. The hysteresis is a consequence of capillary condensation in pores wider than ~4 nm. The vapor-liquid phase transition is delayed due to nucleation, which does not occur in the desorption. If the mesopores are smaller this effect does not occur and a type IV(b) isotherm is obtained. A type V isotherm indicates a not entirely covered surface. Small amounts are adsorbed at low relative pressures and more filling is happening at higher relative pressures by nucleation growth.

Evaluation of the surface area of porous materials is commonly performed by the Brunauer-Emmett-Teller (BET) model by transforming the physisorption isotherm into a "BET-plot" and applying the BET-equation (Equation 8.1).

$$\frac{\frac{p}{p_o}}{V_{ads}(1-\frac{p}{p_o})} = \frac{1}{V_{mono}C} + \frac{C-1}{V_{mono}C}(p/p_0) \tag{8.1}$$

With V_{ads} being the total adsorbed volume, V_{mono} the monolayer volume, and C the adsorption constant. V_{mono} is obtained by a linear relation. The range is usually restricted to a part of the isotherm within p/p_0 ~0.05 – 0.3 where monolayer formation is assumed. In the case of microporous materials, this range may vary due to a different mechanism i.e. micropore filling and monolayer adsorption overlap. In this case, the criteria for the proper selection of the range to consider are as follow: (1) the adsorbed amount of gas has to increase with increasing relative pressure, and (2) a positive intercept of the linear region.

The specific BET surface area (S_{BET}) is then calculated following equation 8.2.

$$SSA_{BET} = \frac{V_{mono}\sigma_{N_2}N_A}{m} \tag{8.2}$$

With σ_{N2} being the cross-section of a nitrogen molecule (~0.162 nm^2), N_A the Avogadro constant, and m as the mass of adsorbent.

The isotherms serve also information about the pore size distribution. Mesopore size analysis with the Barrett-Joyner-Halenda (BJH) method is one of the basic methods. It is based on the

Kelvin equation (Equation 8.3), which correlates the relative pressure, at which pore condensation in a cylindrical pore occurs and the radius r of the meniscus of the condensed liquid.

$$\ln\left(\frac{p}{p_0}\right) = -\frac{2\gamma V_m \cos\varphi}{rRT} \tag{8.3}$$

With γ as the surface tension of the bulk fluid, V_m as the ideal gas volume, φ the wetting angle, R the ideal gas constant, and T the temperature. This method is restricted to cylindrical pores with a diameter above 2.5 nm and is not valid for narrow mesopores. Other methods like the semi-empirical Dubinin-Radushkevich or Horvath-Kawazoe method for the determination of the micropore size and distribution were developed. However, these methods are not applicable when also mesopores are present. Another method is the t-plot method. Within this method, the adsorbed volume is plotted as a function of the film thickness, and every deviation from the point of origin is ascribed to the presence of micropores. The α_a-method further extends this method by a non-porous reference. The most recent model is the density functional theory (DFT). It shows to be suitable for the determination of micro- and mesoporous materials and overcome the limitations of the BHJ-method.[257]

It is important to highlight here, that all gas sorption results are derived from idealized theoretical models and the obtained values might contain errors. The theories are based on carbon materials, which should cause attention when applying the models to the materials in the present thesis, which contain a high amount of nitrogen.

Before all physisorption experiments, the samples were degassed at 150 °C for 20 hours under high vacuum. Nitrogen physisorption experiments were performed at 77 K on a Quadrasorb apparatus (Quantachrome Instruments). The surface area was determined by using multipoint BET model in the relative pressure below 0.2 using the Rouquerol criteria. The values were obtained after applying the method in the linear region with the best correlation.

CO_2 Physisorption

As described before, nitrogen sorption is suitable for micro-, meso-, and macropore analysis but not suitable for the analysis of narrow micropores due to kinetic restrictions and diffusion issues. Using CO_2 as test gas can be a useful alternative for micropore analysis. The kinetic diameter of CO_2 is 0.330 nm (kinetic diameter of nitrogen: 0.364 nm). On the other hand, CO_2 has a quadrupole moment and thus interacts with polar functionalities. In the case of pure carbon materials this is usually no issue. However, for the materials presented in this thesis, containing a high amount of nitrogen, the existing models can not be applied.[258] Still, the isotherms can give useful information about the micropores and polarity of the materials.

The strength of the adsorbate- adsorbent interactions can be expressed by the heat of adsorption (Q_{st}), which is obtained by CO_2 sorption measurements at two different temperatures (usually 273 K and 298 K) and applying the Clausius-Clapeyron equation (Equation 8.4) for a specific amount adsorbed.

$$ln\frac{p_2}{p_1} = \frac{(T_2 - T_1)Q_{st}}{RT_1T_2} \tag{8.4}$$

With p for the pressure and T for temperature (i.e. T_1=273 K and T_2=298 K), and R for the universal gas constant.

When considering the material for gas sorption, also the selectivity to adsorb a gas in common conditions, i.e. CO_2 diluted in nitrogen (like in air), needs to be considered. The ideal adsorbed solution theory (IAST) is commonly used as a selectivity parameter. CO_2 and N_2 isotherms at 298 K are measured and the adsorbed amounts at specific pressures are used to calculate the $IAST_{CO2/N2}$ with Equation 8.5.

$$S_{IAST} = \frac{q_{CO2}/q_{N2}}{p_{CO2}/p_{N2}} \tag{8.5}$$

With q for the amount adsorbed at pressure (p). To imitate a more realistic situation the commonly used pressure for N_2 is 0.85 kPa and for CO_2 15 kPa. As the name already implies this method is

also based on idealization and assumptions are, that the solution is ideal and in equilibrium with the gas phase.

CO_2 sorption experiments in this thesis were performed on the Quadrasorb apparatus at 273 K and 298 K. Before each measurement, samples were degassed at 150 °C for 20 h under vacuum.

Vapor Adsorption

Water vapor sorption experiments can be used to obtain information on the hydrophilicity of the surface of materials. Due to the high dipole moment of water it has higher interactions with higher enthalpy with polar surfaces. Measurements in this thesis were performed on a Quantachrome Autosorb IQ apparatus at 25 °C. Before each measurement, the sample was degassed at 150 °C for 20 h under vacuum.

Elemental Analysis (EA)

With elemental analysis, the qualification and quantification of C, H, N, and S in a sample can be performed. EA is a combustion method where the sample is burned in oxygen atmosphere up to ca. 1000 °C and the decomposition products such as CO_2, H_2O, NO, N_2 and SO_2 are detected.

EA measurements in this thesis were performed using a vario MICRO cube CHNOS Elemental Analyzer in the CHNS mode. Antje Voelkel from MPIKG performed the measurements.

Inductively Coupled Plasma – Optical Emission Spectroscopy (ICP-OES)

For the qualification and quantification of other elements than C, H, N, and S, such as metals, Inductively Coupled Plasma – Optical Emission Spectroscopy (ICP-OES) can be used. Within this method, an inductively coupled plasma is used as an excitation source and argon is passed through it continuously. The electrically conducting ionized gas can reach temperatures up to 10000 K. The sample is usually in an aqueous solution. The solution is converted into fine droplets by a nebulizer and the aerosol is injected into the argon flow. At 7500 K the sample is atomized

and the atoms become excited and ionized. The intensity of element-specific radiation is detected. Quantification can be made by comparison with a previously measured calibration.[259]

ICP-OES measurements in this thesis were conducted using an ICP-OES Optima 8000 Perkin Elmar. Multi-Element-Standards have been used for calibration. Samples are dissolved in aqua regia before the measurement. Jessica Brandt from MPIKG performed the measurements in this thesis.

Fourier Transform Infrared spectroscopy (FTIR)

Infrared spectroscopy measurements are based on the adsorption of specific wavelengths by molecules, which are irradiated with electromagnetic radiation, which corresponds to the energy required for a transition. Here the electromagnetic radiation is in the mid-IR range from 4000 to 400 cm^{-1}. Vibrational and vibrational-rotational transitions can be detected if the requirements of a change in dipole are fulfilled. With this technique, structural clarification and quantitative evaluation can be performed. The spectra is shown as the transmission of the radiation in dependence of the wavenumber. A signal occurs if the substance absorbs light due to a transition. In an FTIR setup, a beam of many frequencies is coupled into a Michaelson interferogram, and data is obtained by processing through applying Fourier transformation.

Measurements in this thesis have been performed on a Thermo Scientific Nicolet iD5 spectrometer.

Powder X-ray Diffraction (PXRD)

PXRD measurements are based on the interaction between an X-ray beam and electrons of atoms in the sample. It is a widely used characterization method for crystalline materials. The X-rays are generated in an X-ray tube upon bombardment of copper with high energy electrons. This results in the radiation of a continuous X-ray spectrum. The generated monochromatic X-rays are directed towards the sample. At the sample elastic and inelastic interactions occur. Inelastic

interactions cause coherent scattering, which represents the basis for all diffraction experiments. If the wavelength (λ) of the radiation is in the range of the distance of the diffraction lattice diffraction occurs. Positive interference exists only for specific diffractions angles (θ). The Bragg´s Law (Equation 8.6) gives the mathematical description of the interlayer spacing (d_{hkl}) of the atomic planes and the wavelength (λ) with respect to θ.

$$n\lambda = 2d_{hkl}sin\theta \tag{8.6}$$

Positive interferences (positive n) leads to reflections in the diffractogram, giving characteristic diffraction patterns of the material.

PXRD pattern in this thesis were performed using a Bruker D8 Advance diffractometer with Cu-Kα radiation (λ=1.5418 Å) between 5° and 70° 2θ with 1625 steps and 1 step per time.

X-ray Photoelectron Spectroscopy (XPS)

XPS is a non-destructive surface analysis (sample depth ca. 3 nm – 10 nm) technique. The analysis takes place in ultra high vacuum. It gives element identification and information about the chemical state of the elements, their relative composition, and the structure of the valence band. In a typical experiment, the sample is irradiated with X-ray photons (of energy h*υ*) and an electron from the core level is ejected with the kinetic energy (K.E.). This phenomenon is called the photoelectric effect. The Einstein equation (Equation 8.7) gives the correlation to the binding energy (B.E.) of the ejected electron.

$$K.E. = h\nu - B.E. - \phi \tag{8.7}$$

With Φ as work function and B.E. as the binding energy of the ejected electron, which is characteristic for each element. Additional information about the specific chemical binding motifs can be obtained due to the dependency of the fine structure of the element on its surrounding.

XPS measurements in this thesis were performed on a ThermoScientific Escalab 250 Xi. A micro focused, monochromated Al Kα X-ray source (1486.68 eV) and a 400 µm spot size were used in the analysis. Samples were prepared using carbon tape. LiCl was added to each sample in order to calibrate the binding energies towards Li. ThermoScientific Avantage software was used to analyze the resulting spectra. Measurements were performed by Dr. Johannes Schmidt (TU Berlin).

Electron Microscopy

Electron microscope measurements are based on the interaction between an electron beam and the sample in high vacuum. The electrons are generated in an electron gun, accelerated by an electromagnetic field, and focused through a series of electromagnetic lenses onto the sample. When the electron beam hits the sample, different types of interactions shown in **Figure A2** are happening. With the different electron microscope techniques, different interactions are important and detected.

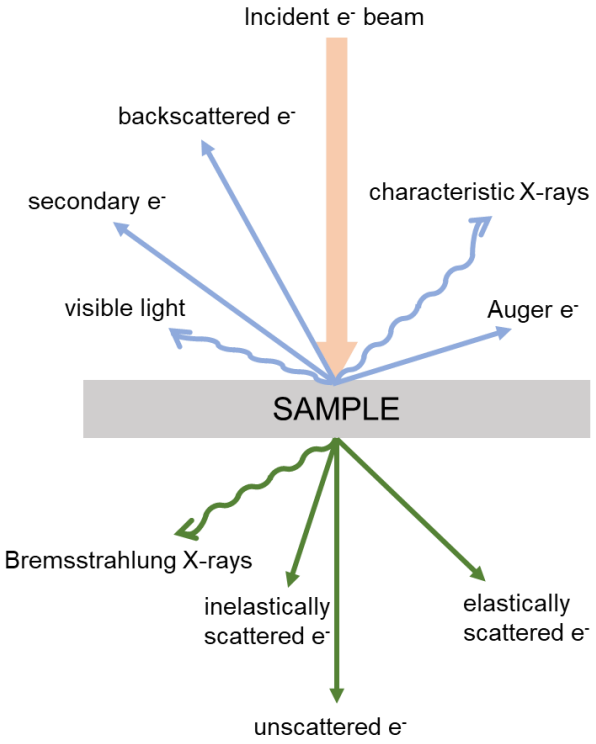

Figure A2. Different types of interactions between the electron beam and a sample.

Scanning Electron Microscopy with Energy Dispersive X-ray Spectroscopy (SEM-EDX)

When SEM measurements are performed, the secondary and backscattered electrons are detecting for imaging. The secondary electrons are important for the analysis of the morphology and topography of the samples. They are emitted close to the surface and are low in energy. Backscattered electrons are higher in energy and emitted from a deeper region of the sample. When imaging backscattered electrons, heavier atoms appear brighter in the image. SEM coupled to EDX is used to analyze the composition of a sample. By interaction of the incident beam, an electron from an inner shell is ejected and the vacancy is filled by an electron from an outer shell. This induces the generation of an element specific X-ray which can be used for qualitative and quantitative analysis. The energy of the released X-ray photons corresponds to the energy difference between the two electron states.

The data presented in this thesis was recorded on an LEO 1550-Gemini microscope operating at 3.00 kV to 20.00 kV. All samples were sputtered with an approximately 10 nm thick film of an 80% gold/20% palladium mixture to increase the conductivity of the surface. EDX measurements are recorded with a Link ISIS-300 system (Oxford Microanalysis Group) equipped with a Si(Li) detector and an energy resolution of 133 eV.

Transmission Electron Microscopy (TEM)

In TEM measurements, the electrons that are transmitted through a very thin film (preferably, less than 100 nm) of the sample are detected. TEM and STEM modes of the microscope use different condenser lenses settings: in TEM mode the illumination is parallel whereas in STEM mode the beam is finely focused and scans across the specimen. Aberration correctors improve the resolution, making HRTEM or HR-STEM imaging at atomic scale possible, which is, for example, crucial for studying materials with single atoms and nanoclusters to prove their presence.

By processing HRTEM images and applying FFT, one can learn about the local crystallographic structure of the materials at the atomic and nanoscale by choosing different areas of the sample during image processing. On the other hand, selected area electron diffraction (SAED) is obtained from large areas of the specimen and is used for determining the average crystallographic structure of the materials.

Since in STEM mode the beam scans the sample, it is possible to detect several signals simultaneously, for example, by bright-field (BF), high angle annular dark-field, and secondary electron (SE) detectors. Detection of unscattered (transmitted) electrons in this mode results in bright-field-STEM (BF-STEM) images, where darker regions in the image correspond to heavier elements containing regions and/or more crystalline/ordered ones. Detection of high angle scattered electrons results in HAADF-STEM images, the origin of the contrast in these images is the Z-contrast (metal single atoms, clusters, nanoparticles on carbon/carbonaceous materials, for instance). Therefore, this imaging method enables unambiguous identification of elements depending on their Z number elements – heavier elements appear brighter in the image. In addition to this, SE-STEM images provide information about the morphology and topography of the specimen analogously to SEM.

Besides all the imaging capabilities, TEM is also an analytic technique. Energy-dispersive spectrometry (EDS) and EELS give qualitative and quantitative information about chemical elements present in the material. In EDS, characteristic X-rays are detected and in EELS inelastically scattered electrons. EELS is also sensitive to different chemical bonding present in the structure.

Before TEM and STEM observations, samples were sonicated in ethanol for 15 min and the obtained suspension was drop-casted to a Cu grid with lacey carbon support and dried for 15 min. Studies were performed using a double Cs corrected JEOL JEM-ARM200F (S)TEM operated

at 80 kV and equipped with a cold-field emission gun, a high-angle silicon drift Energy Dispersive X-ray (EDX) detector (solid angle up to 0.98 steradians with a detection area of 100 mm^2) and a Gatan Quantum GIF spectroscopy system. HAADF-STEM images were collected at a probe convergence semi-angle of 41.7 mrad. All electron energy loss spectra were collected at dispersion of 0.25 eV ch 1 in order to resolve C K, N K and, O K ionization edges.

Thermogravimetrical Analysis Coupled with Mass Spectroscopy (TGA-MS)

TGA is a combustion method to obtain information about the stability and the transition state of a material. The decomposition in inert or oxygen atmosphere is recorded in the dependence of the temperature. If the TGA is coupled with a mass spectrometer, the released decomposition products can also be identified.

TGA in this thesis was performed from 25 °C to 1000 °C in a NETZSCH TG 209 F1 Libra device using either nitrogen or synthetic air as carrier gas and a heating rate of 10 K min^{-1} in a Pt crucible. TGA-MS measurements were performed using a thermo microbalance TG 209 F1 Libra (Netzsch, Selb, Germany) coupled with a Thermostar MS (Pfeiffer Vacuum; Asslar/Germany) with an ionization energy of 75 eV. A platinum crucible was used for the measurement of 10 mg of the samples. Samples were heated at 10 K min^{-1} to 910 °C in a helium flow of 10 ml min^{-1} and a purge flow of 10 ml min^{-1}. Data were recorded and analyzed by the Proteus (6.0.0 to 8.0.0) and Quadstar (7.03, MID modus) software package.

Carbon dioxide temperature-programmed desorption (CO_2-TPD)

With TPD measurements, the interaction between adsorbed molecules and a surface can be monitored. After purging the sample with an inert gas at higher temperatures the sample is loaded with the test gas, here CO_2. When the material is loaded with the test gas, the temperature is raised and desorption of the test gas, here CO_2, is detected. Depending on the temperature of desorption, conclusions about the binding strength can be made.

TPD experiments in the thesis were performed with a Micromeritics Autochem II 2920 analyzer. The sample (0.1 g) in a quartz micro reactor was pretreated with He (40 cm^3min^{-1}) at 423 K for 60 min, cooled down to 323 K and the CO_2 sorption were taken place in 20 consecutive pulses (25 vol% CO_2/He mixture, 1 cm^3STP per pulse). After purging with He (10 $cm^3STPmin^{-1}$) for 90 min, desorption was monitored until 673 K with a heating rate of 10 K min^{-1} and a He flow of 25 $cm^3STPmin^{-1}$.

Nuclear Magnetic Resonance Spectroscopy (NMR)

NMR analysis gives a tool for the complete analysis of the structure, the content, and purity of chemical compounds, by the characteristic spin of the nuclei of many element isotopes. The most common measured isotopes are ^1H, ^{13}C, ^{19}F, ^{31}P, among others. The sample is placed into an external magnetic field, which induces the energy levels to split up. The resulting energy gap equals a frequency of radiation, which depends on the strength of the magnetic field as well as on the magnetic properties of the isotope. The magnetic field is affected by electron shielding of the nuclei. This results in different resonance frequencies for different chemical environments and serves information for structural analysis. NMR is a widely used and powerful analysis technique.

^1H-NMR measurements in this thesis were performed on a Bruker Ascend 400 (400MHz) spectrometer. Chemical shifts (δ) are reported in ppm and adjusted to the internal standard of the residual proton signal of the deuterated solvent (i.e. Chloroform-d1). The spectra are measured at room temperature.

Solid-state ^{13}C (100.73 MHz) CPMAS NMR (ssNMR) spectra have been obtained on a Bruker AV WB 400 spectrometer at 300 K using a 4 mm triple channel probe head. Samples were carefully packed in a 4-mm diameter cylindrical zirconia rotor with Kel-F end-caps. Operating conditions involved 2.75 ms 90 ^1H pulses and decoupling, field strength of 90.9 kHz by TPPM sequence. Typical acquisition parameters for ^{13}C CPMAS were: spectral width, 35 kHz; recycle delay, 4 s;

acquisition time, 29 ms; contact time, 4 ms; and spin rate, 10 kHz. ^{13}C spectra were originally referenced to an adamantine sample and then the chemical shifts were recalculated to the Me4Si (for the CH_2 atom d(adamantane) ¼ 29.5 ppm). Measurements were performed by Dr. Maria Jose de la Mata (Universidad Autónoma de Madrid).

Catalytic Tests

The Knoevenagel condensation reaction in section 4.2 was performed by adding 50 mg of catalyst into 10 ml of acetonitrile solution containing 1 mmol of aldehyde and 2 mmol of malononitrile (or ethylcyanacetate). The reaction mixture was stirred at 70 °C in an oil bath for 24 h, with sample extraction after 1 h, 2 h, 4 h, 7 h, and 24 h. Evaluation of the reaction was performed by ^{1}H NMR spectroscopy and GC-MS analysis. The product was identified by GC-MS (GC: HP-5MS column, inner diameter=0.25 mm, length=30 m, film=0.25 μm and MS: Agilent GC 6890, Agilent MSD 5975). The percentage of conversion was calculated by ^{1}H NMR spectroscopy.

Electrochemical Methods

A common tool to analyze the ORR activity is the use of a rotating ring electrode (RDE). The rotation allows the controlled mixing of the electrolyte. A typical RDE setup consists of a rotating working electrode, a reference electrode, and a counter electrode as shown in **Figure A3 A**.

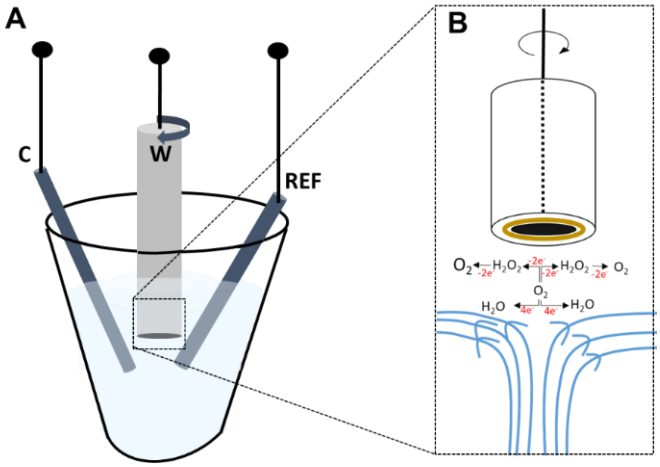

Figure A3. A) Schematic illustration of a typical RDE/RRDE setup with counter electrode (C) reference electrode (REF) and rotating working electrode (W). B) RRDE electrode and the oxygen reduction at the disk (black) and hydrogen peroxide oxidation at the ring (yellow).

Catalytic activity towards ORR is usually tested by cyclic voltammetry (CV) and determined by linear sweep voltammetry (LSV) at different rotation rates. When measuring CV curves, the potential is repeatedly swept back and forth between two boundary values, and the current is measured. LSV measurements are very similar. A potential is swept at a constant sweep rate from an initial potential to a final potential and also the current is measured. For determination of the ORR activity, the LSV starts at a cathodic potential where no reaction takes place and thus no current is measured. When going to a negative potential a current will appear as soon as the potential is negative enough to introduce the reduction of oxygen. By further increasing the negative potential, a limiting current will be reached. At this potential, every oxygen molecule is immediately reduced and the current is determined by the mass transport of oxygen towards the electrode. By repeating this measurement at various rotation speeds and applying the Koutecký-Levich equation (Equation 8.8) the electron transfer number (*n*) can be determined.

$$\frac{1}{j} = \frac{1}{J_L} + \frac{\nu^{1/6}}{0.620 \cdot n \cdot F \cdot A \cdot C_{O_2} \cdot D_{O_2}{}^{2/3}} \frac{1}{\omega^{1/2}} \tag{8.8}$$

With *j* as the measured current density, J_L as the kinetic limiting current density, ω as the angular velocity of the disk, F is the Faraday constant (96485 C mol^{-1}), ν is the kinetic viscosity (0.01004 cm^2 s^{-1}), C_O is the oxygen concentration in the electrolyte (1.39 x 10-3 mol l^{-1}), and D_O is the diffusion coefficient of oxygen in the electrolyte (1.9 x 10-5 cm^2 s^{-1}).

The plot of the reciprocal measured current j^{-1} vs. the reciprocal angular rotation rate ω^{-1} gives a straight line and the slope of the line can then be used to calculate *n*. In addition to the calculation of the electron transfer number, compare parameters like the onset potential (E_{Onset}), the half-wave potential ($E_{1/2}$), and the limiting current (J_L) can be obtained from the LSV curve. Commonly the measurement at 1600 rpm is used to report the mentioned parameter.

A further expansion of the RDE is the rotation ring disk electrode (RRDE) (**Figure A3 B**). A platinum ring electrode is placed around the disk and connected to a second potentiostat and a constant positive potential is applied. The overall axial flow of the electrolyte brings oxygen first to the disk electrode and the outward radial flow subsequent brings then the molecules to the ring. With this method, the product evolving at the disk can be in situ detected and quantified at the ring. In case of the ORR hydrogen peroxide, which might evolve due to a two-electron transfer, can be oxidized at the ring and a current from the ring can be measured. For quantification, first, the collection efficiency (N) of the RRDE needs to be determined. Then the disk current and the ring current during the experiment are collected and by applying Equation 8.9. and 8.10. the yield of hydrogen peroxide and the electron transfer number *n* can be determined.

$$n = 4 * \frac{I_d}{\frac{I_d + I_r}{N}} \tag{8.9}$$

$$\% H_2O_2 = 200 * \frac{\left(\frac{I_r}{N}\right)}{(I_d + I_r)/N} \tag{8.10}$$

With I_d and I_r as the disk current and ring current respectively, N as the collection efficiency.

All electrochemical tests were performed in a typical three-electrode setup with platinum as counter electrode, an $Ag/AgCl_{(sat.\ KCl)}$ reference electrode, and 0.1 M KOH as electrolyte. As working electrode, an RDE/RRDE electrode from PINE with 10 µl of the as prepared ink on the glassy carbon was used. The ink was prepared by mixing 50 µl Nafion, 500 µl distilled water, 250 µl isopropyl alcohol, and 5 mg catalyst and subsequent 5 min of sonication. The ink was dried at room temperature on the glassy carbon. As a reference, the same ink was prepared with commercial carbon/platinum 20% and used as catalyst. The measurements were conducted on an Interface 1000 from Gamry and for RRDE experiments two potentiostats were synchronized. Potentials in this thesis are converted into RHE overpotential according to Equation 8.11.

$$E_{RHE} = E_{Ag/AgCl} + 0.197\,V + 0.089 * pH - 1.23 \tag{8.11}$$

CV measurements are commonly used for investigations of electrochemical processes. The current is measured in dependence on the applied potential. It can be used to identify electrochemical processes like redox reactions and adsorption phenomena like double layer formation. To test the ORR activity in this thesis CV measurements are first performed in nitrogen saturated electrolyte and subsequent in oxygen saturated electrolyte with a scan rate of 10 mV s^{-1}.

In this thesis, measurements are performed in oxygen saturated 0.1 M KOH with a scan rate of 10 mV s^{-1}, a step size of 10 mV and rotation speeds of 0-1600 rpm. The electron transfer number *n* is calculated from RDE measurements according to the Koutecký–Levich equation 8.8. at various rotation speeds (with: *F* is the Faraday constant (96485 C mol^{-1}), *v* is the kinetic viscosity (0.01004 $cm^2\ s^{-1}$), C_O is the oxygen concentration in the electrolyte (1.39 x 10^{-3} mol l^{-1}), and D_O is the diffusion coefficient of oxygen in the electrolyte (1.9 x $10^{-5}\ cm^2\ s^{-1}$). Additionally, RRDE measurements were performed under the same conditions. The potential at the ring was kept at 0.3 V vs. $Ag/AgCl_{(sat.\ KCl)}$. Hydrogen peroxide yield and *n* were calculated according to equations 8.9. and 8.10. Before RRDE measurements the collection efficiency (N=30%) was determined from the reduction of $K_3Fe(CN)_6$.

Stability tests of the catalyst were implemented by chronoamperometrie measurements for 4 h in oxygen saturated 0.1 M KOH with a potential of -0.15 V vs. $Ag/AgCl_{(sat.\ KCl)}$. Methanol stability tests were performed by adding 0.5 ml methanol after 1000 s to a chronoamperometrie measurement.

8.3 Experimental Section

8.3.1 List of Used Chemicals

Substance	Chemical formula	Supplier	Purity grade
Guanine	$C_5H_5N_5O$	Merck	99%
Uric acid	$C_5H_4N_4O_3$	Roth	≥ 99%
Sodium chloride	NaCl	Merck / Alfa Aesar	≥ 99.5 %
Zinc chloride	$ZnCl_2$	Merck / Alfa Aesar	≥ 98%
Hydrochloric acid	HCl	Merck	37%
Malonotrile	$C_3H_2N_2$	Acros Organics	99%
Benzaldehyde	C_7H_6O	Merck	≥ 99 %
Acetonitrile	C_2H_3N	Honeywell	≥ 99.9 %
1-Butyl-4-methylpyridinium tricyanomethanide	$C_{14}H_{16}N_4$	IOLITEC	<98 %
Potassium chloride	KCl	Fisher chemical	>=99%
Potassium hydroxide	KOH	Fisher chemical	85.8%
Copper (II) acetate	$Cu(CH_3COO)_2$	Sigma-Aldrich	98%
Nafion	$C_7HF_{13}O_5S \cdot C_2F_4$	Sigma-Aldrich	5 wt% in lower aliphatic alcohols and water (15-20 % water)
Platinum on graphitized carbon	Carbon/platinum 20%	Aldrich	20 wt. % Pt loading

8.3.2 Materials Synthesis

Synthesis of cG@T (section 4.1)

Guanine condensates were synthesized by heat treatment of guanine under nitrogen atmosphere. 1 g of guanine was placed into a ceramic crucible and covered with a ceramic lid. The oven with the sample was purged for 20 minutes with nitrogen and then heated until the desired temperature (500 °C, 600 °C, 700 °C, or 800 °C for cG@500, cG@600, cG@700, and cG@800 respectively) with a heating rate of 1 °C min^{-1} with constant nitrogen flow. The final temperature was held for 2 h. After cooling down to ambient temperatures, the crucible was removed and the product was obtained as a black powder.

Synthesis of cG@T-SZx (section 4.2)

Porous guanine condensates were synthesized by salt melt templating of guanine. 1 g of guanine was ground with the desired amount of NaCl and $ZnCl_2$ (see **Table S 4.2-1**) with a pestle and a mortar. The mixture was put into a ceramic crucible with a lid and placed into an oven. The oven was purged for 20 min with nitrogen and then heated until the desired temperature (500 °C, 600 °C, 700 °C, or 800 °C for cG@500-SZX, cG@600-SZ10, cG@700-SZ10, and cG@800-SZX respectively) under constant nitrogen flow with a heating rate of 1 °C min^{-1}. The final temperature was held for 2 h. After cooling down to ambient temperatures, the crucible was removed and the samples were washed in 300 ml of 1 M HCl two times and 1 time with distilled water and dried at 70 °C for 3 hours.

Synthesis of UA-T-SZ (section 4.3)

Uric acid-derived condensates were synthesized similar to cG@T-SZX samples. 1 g of uric acid was ground with a pestle and a mortar with 5 g of NaCl and 5 g of $ZnCl_2$, transferred into a ceramic crucible with a lid, and placed into an oven. After purging for 20 min with nitrogen the oven was heated under constant nitrogen flow and a heating rate of 1 °C min^{-1} to the desired final

temperature (500 °C, 700 °C, 750 °C, 800 °C, or 900 °C for UA-500-SZ, UA-700-SZ, UA-750-SZ, UA-800-SZ, and UA-900-SZ respectively). The final temperature was kept for 2 h and after cooling down to ambient temperatures the samples were washed 2 times in 1 M HCl and one time in distilled water. After drying at 70 °C for 3 hours the black powder was obtained.

Synthesis of BTCN-Cu0 (section 5)

1 g of 1-Butyl-4-methylpyridinium tricyanomethanide (BTCN) was ground with 5 g potassium chloride and 5 g zinc chloride with a mortar and a pestle. The mixture was transferred into a ceramic crucible with a lid and placed in an oven. After purging for 20 min with nitrogen the sample was heated under constant nitrogen flow with a heating rate of 1 °C min^{-1} up to 250 °C, held there for 2 hours, and heated up to the final temperature of 800 °C. After cooling down to room temperature, the obtained product was washed two times in 300 ml 1 M HCl and one time in distilled water. The obtained black powder is dried at 70 °C for 3 hours.

Synthesis of BTCN-CuX (section 5)

For metal decoration of BTCN-Cu0 a solution of copper (II) acetate in acetonitrile is prepared (the exact amounts of copper (II) acetate can be found in the table below) and 200 mg of BTCN-Cu0 has been added to the copper solution and stirred for 1 hour at room temperature. Subsequently, acetonitrile is evaporated at 70 °C and the powder is transferred into a ceramic crucible with a lid and heated to 350 °C with 1 °C min^{-1} under air atmosphere. After keeping 350 °C for 2 hours, the oven is cooled down to room temperature and BTCN-CuX, where X stands for the amount of copper, is obtained.

BTCN-Cu0	1g BTCN + 5g KCl + 5g $ZnCl_2$
BTCN-Cu1	199 mg BTCN-Cu0 + 5.7 mg copper (II) acetate
BTCN-Cu2	195 mg BTCN-Cu0 + 11.4 mg copper (II) acetate
BTCN-Cu4	199 mg BTCN-Cu0 + 23 mg copper (II) acetate

8.4 Supporting Figures and Tables

Supporting Information for section 4.1

Direct Condensation of Guanine to C_1N_1 Materials for Efficient and Selective Carbon Dioxide Capture

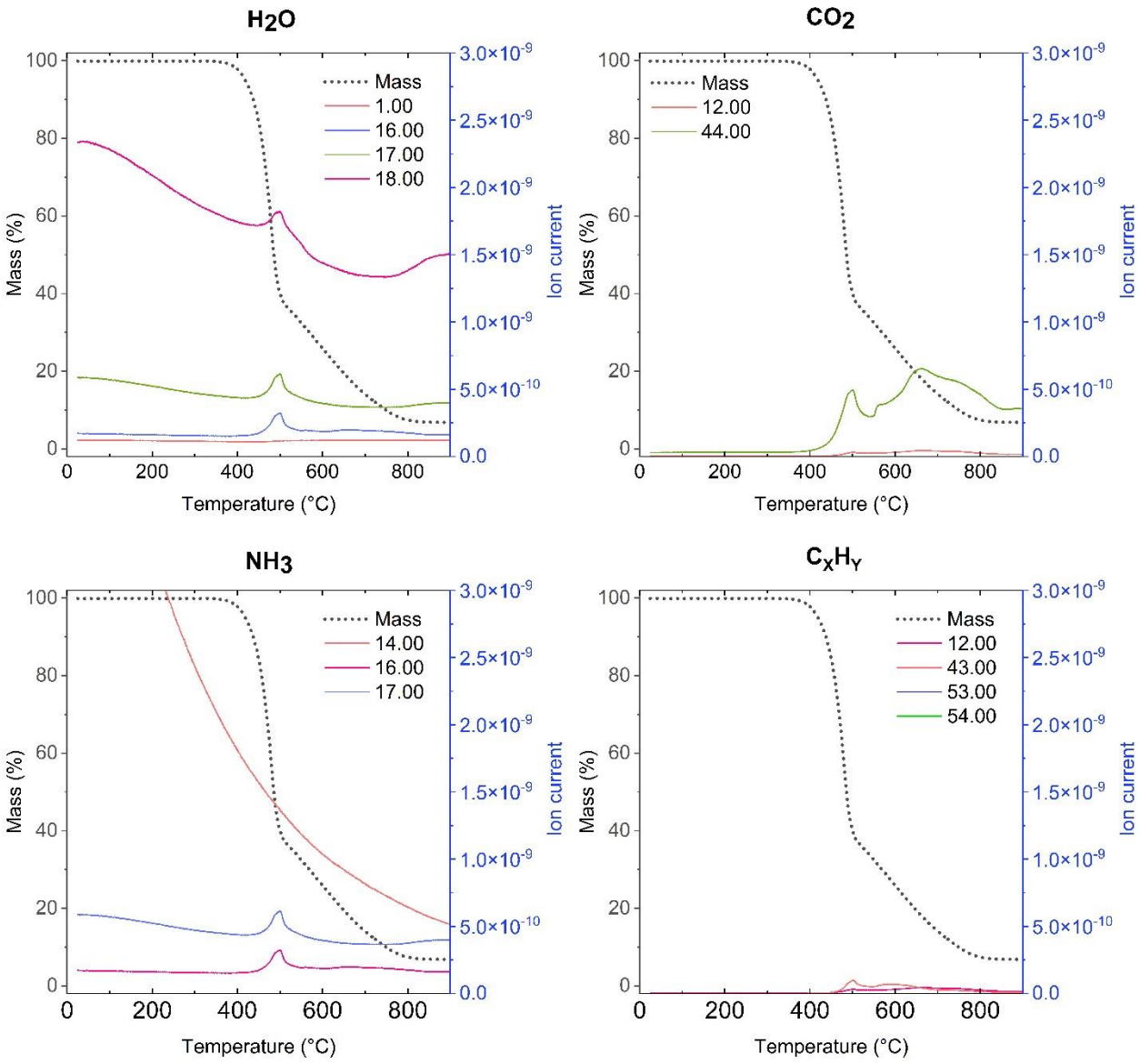

Figure S 4.1-1. TGA-MS in nitrogen atmosphere of guanine. Ion currents of 1, 16, 17, and 18 are ascribed to water; 12 and 14 to CO_2; 14, 16, and 17 to NH_3 and 12, 43, 53 and 54 to hydrocarbons or cyan compounds.

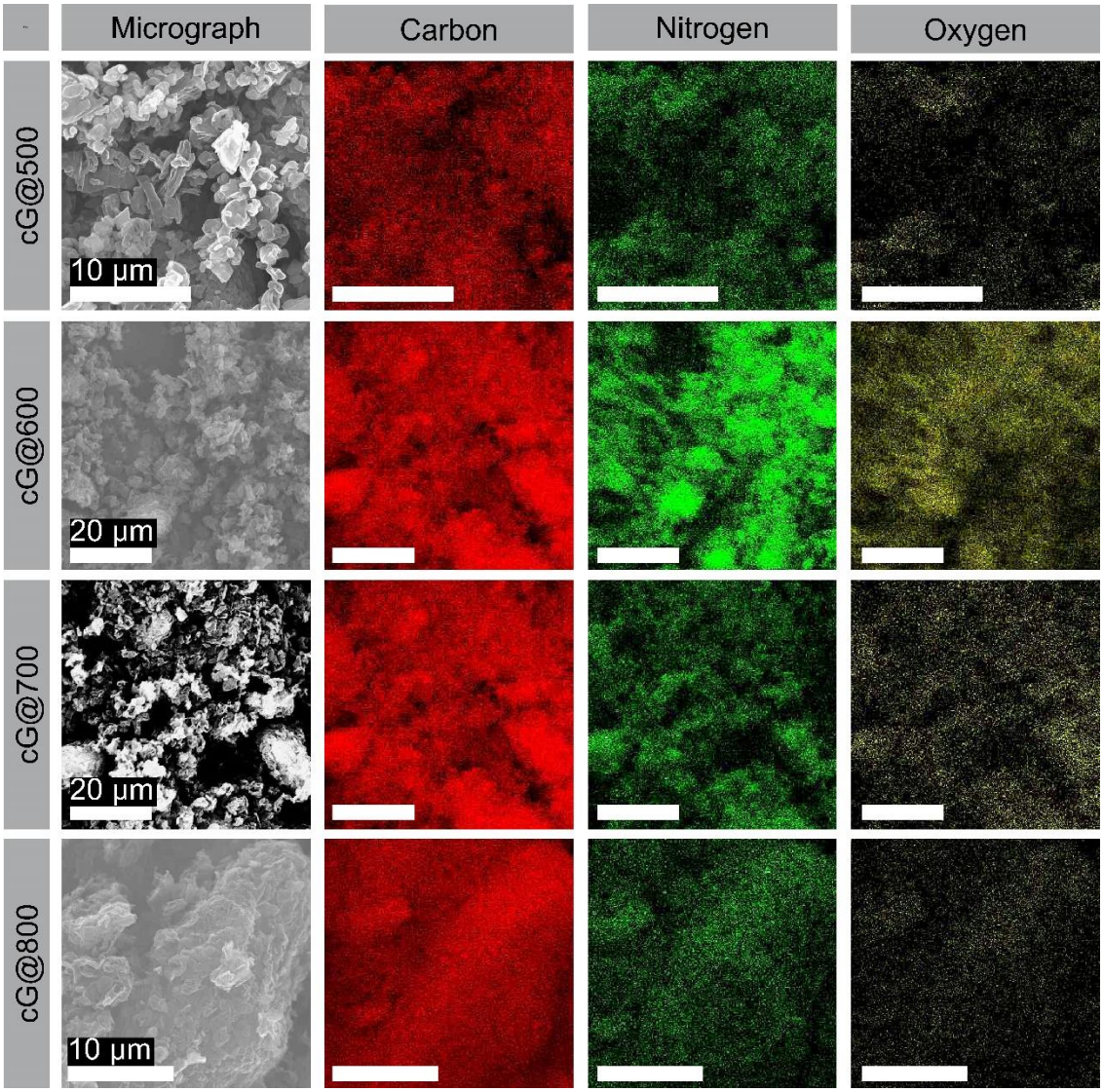

Figure S 4.1-2. SEM-EDX mapping of guanine condensed at different temperatures (cG@500, cG@600, cG@700, and cG@800). Carbon, nitrogen and oxygen are homogeneously distributed.

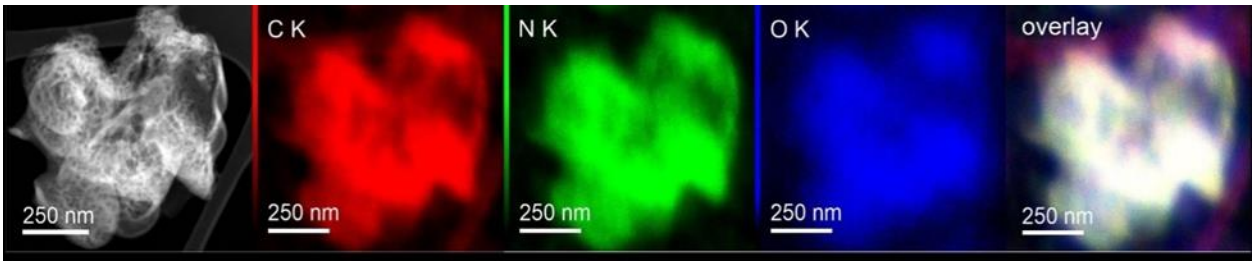

Figure S 4.1-3. STEM-EDX mapping of the sample cG@700.

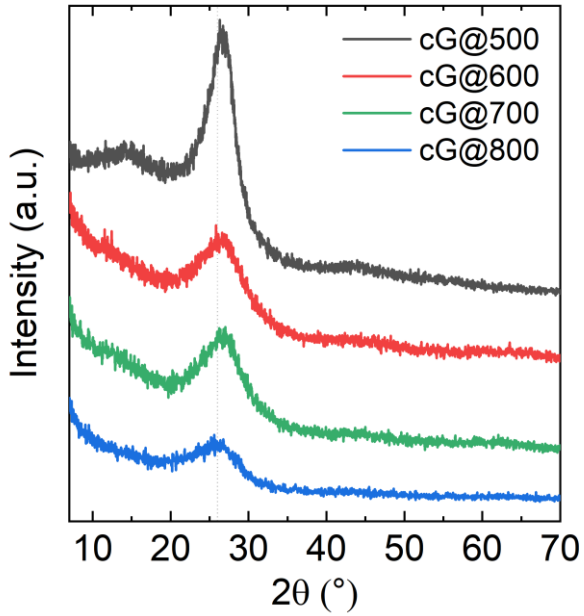

Figure S 4.1-4. PXRD pattern of guanine condensed at different temperatures.

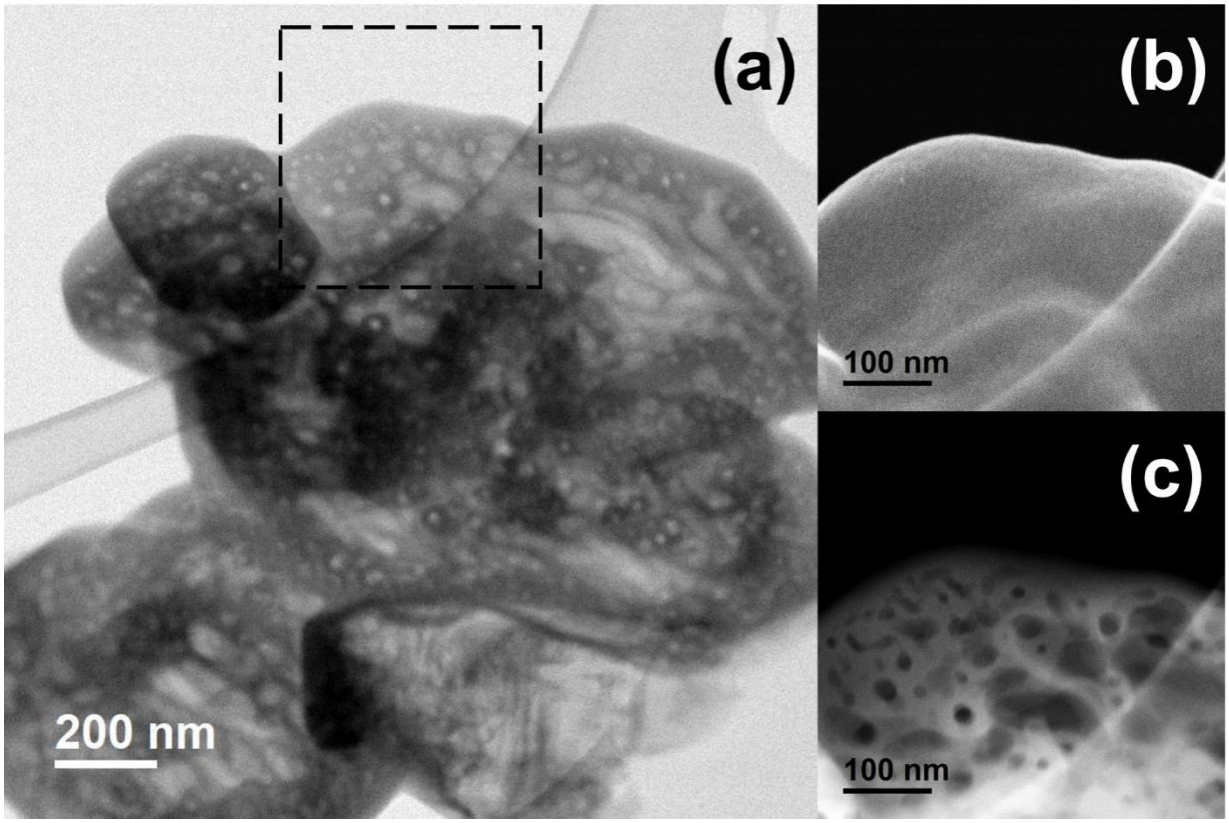

Figure S 4.1-5. A) BF-STEM image and enlargement of the area in dashed box: SE-STEM B) and HAADF-STEM C) images of the sample cG@600 showing the developed pores structure.

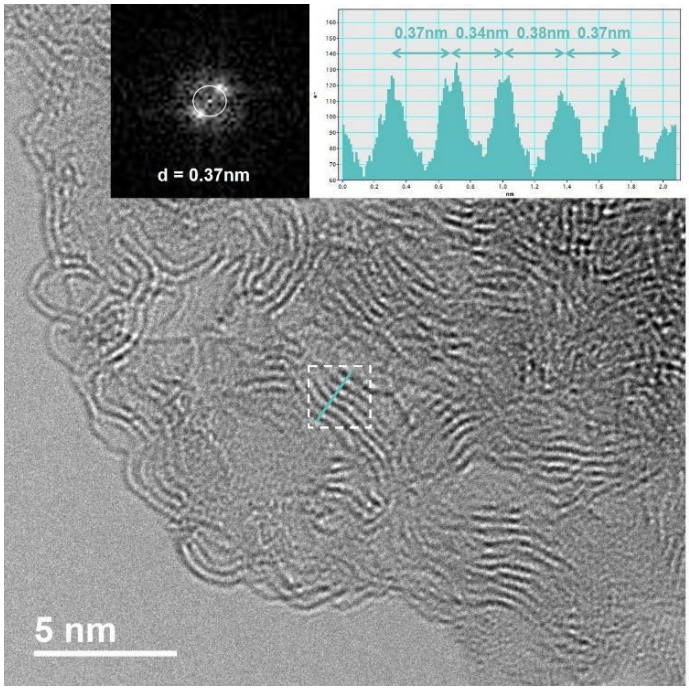

Figure S 4.1-6. TEM micrograph of the cG@700 sample. FFT of the area marked by the dashed white box and intensity profiles of the region marked with blue line are shown as insets.

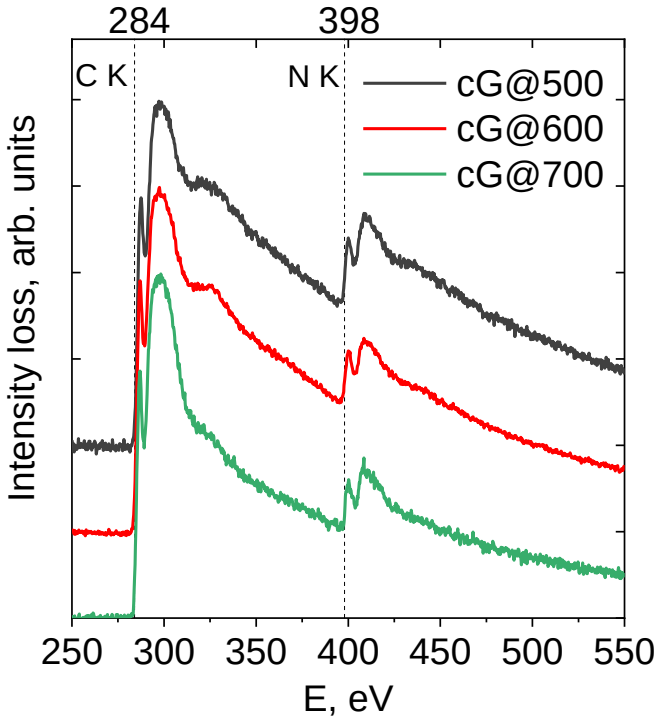

Figure S 4.1-7. EELS spectra of the samples cG@500, cG@600 and cG@700.

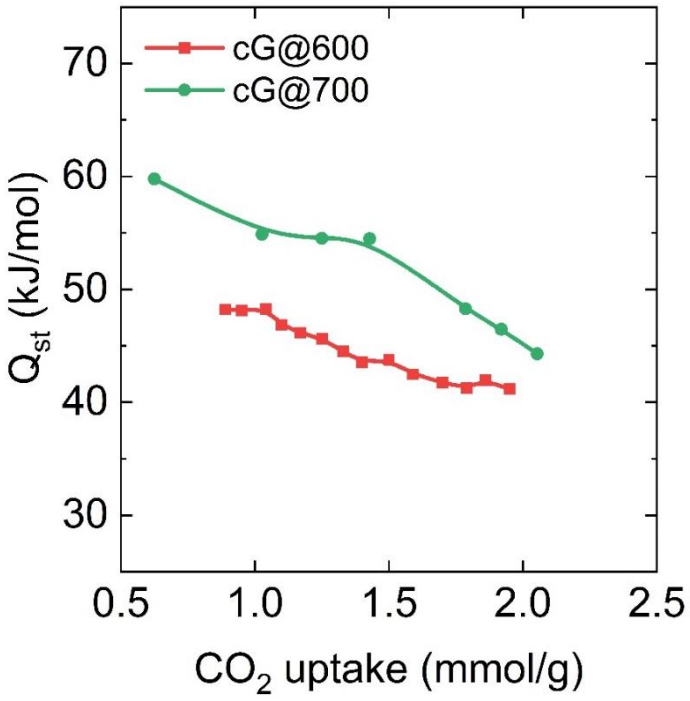

Figure S 4.1-8. Specific heat of adsorption (Qst) of cG@600 and cG@700 vs. CO_2 uptake. Calculated from CO_2 adsorption isotherms at 273K and 298K.

Table S 4.1-1. Comparison of inorganic, metal free carbonaceous adsorbents and their CO_2 adsorption properties.

Sample	Material	SSA ($m^2\ g^{-1}$)	CO_2 capacity (mmol/g) at 298 K		$IAST_{CO2/N2}$ selectivity at 298K (273K)	$Q_{st,\ max}$	Ref.
			1 bar	0.1-0.15 bar			
cG@600	C_1N_1	208	1.9	0.8	97	51	This work
cG@700	C_1N_1	212	1.4	0.8	66	59	This work
SU-MAC-500	NC	941	4.5	1.4	39	46	[260]
SU-MAC-600		1500	4.2	0.8	22		
SU-MAC-800		2369	3.1	0.4	11		
NC-1-500	NC	650	3.5	1.2	26	28	[241]
NC-1-600		807	4.1	1.2	23	24	
NC-1-700		1503	3.5	0.8	13	22	
SNS-1-20	NC	1180	3.7	1.7	63		[242]
SNS-2-20		2100	4.5	1.9	69	37	
CNF-1	NC	1730	3.3	0.9	10	35	[261]
CNF-2		1580	3.0	0.8	-	35	
KNC-A-HCL	NC	1004	4.0	1.0	26	31	[155]
HCM-DAH-1	N-containing carbon monolith	670	2.6	1.0	28	36	[262]
HCM-DAH-1-900-1		1392	3.3	0.9	17	27	
CP-2-600	NC	1700	3.9	0.9	-	32	[67]
CTF-1	CTF	746	1.4	0.2	20	30	[263]
FCTF-1		662	3.2	0.9	31	35	
R-HAC20	Triazine-Based Polymers	2546	3.9		28		[264]
PCBZL	Triazine-based polymers	424	2.4		148	40	[244]
Sbf-TMP@4:2	Triazine-based polymers	715	3.4		(74)	29	[265]
CIN	Covalent imine network	722	2.5		100	42	[243]
CTPP	Covalent triazine–piperazine linked	779	2.0		84	50	[266]
HAT-CTF-450/600	Conjugated triazine frameworks	1090	4.8	2.0	(183)	27	[267]

Supporting Information for section 4.2

Introduction of Surface Area to Guanine Condensates by Salt Melt Templating and the Potential in Heterogeneous Basic Catalysis

Table S 4.2-1. Synthetic details of guanine condensates with salt melt templating.

Sample	Guanine [g]	NaCl [g]	$ZnCl_2$ [g]	Temp. treatment program	Carbon yield [%]
cG@500-SZ1	1	0.5	0.5	RT to 500 at 1 °C/min, 2 h at 500°C	60
cG@500-SZ6	1	3.0	3.0	RT to 500 at 1 °C/min, 2 h at 500°C	64
cG@500-SZ10	1	5.0	5.0	RT to 500 at 1 °C/min, 2 h at 500°C	61
cG@600-SZ10	1	5.0	5.0	RT to 600 at 1 °C/min, 2 h at 600°C	42
cG@700-SZ10	1	5.0	5.0	RT to 700 at 1 °C/min, 2 h at 700°C	33
cG@800-SZ1	1	0.5	0.5	RT to 800 at 1 °C/min, 2 h at 800°C	16
cG@800-SZ6	1	3.0	3.0	RT to 800 at 1 °C/min, 2 h at 800°C	20
cG@800-SZ10	1	5.0	5.0	RT to 800 at 1 °C/min, 2 h at 800°C	22
cG@800-SZ15	1	7.5	7.5	RT to 800 at 1 °C/min, 2 h at 800°C	23

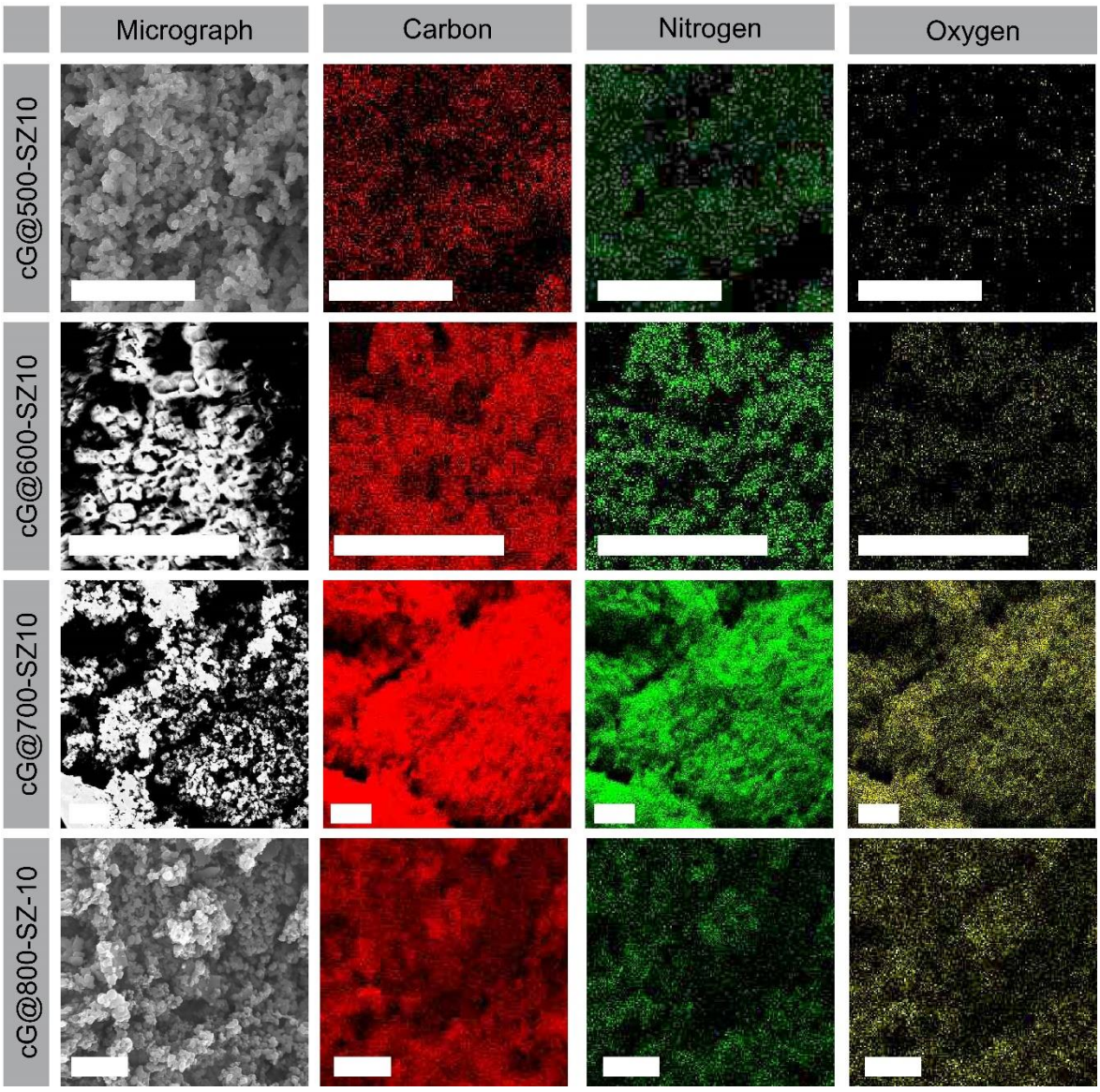

Figure S 4.2-1. SEM micrographs and EDX elemental mapping of guanine condensates at 500 °C, 600 °C, 700 °C, and 800 °C with a guanine to salt melt ratio of 1:10. Mapping shows, that carbon, nitrogen and oxygen are homogeneously distributed on the material. All scale bars: 10 nm.

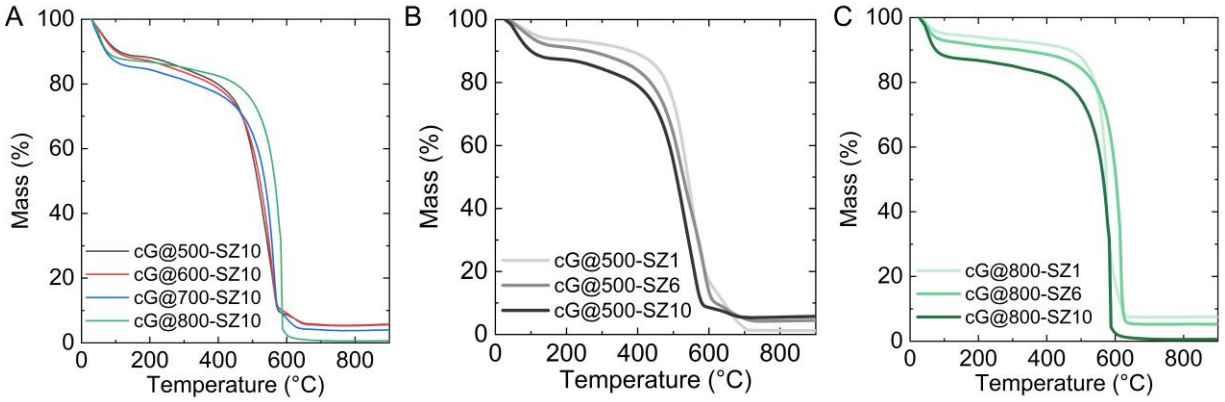

Figure S 4.2-2. TGA analysis in synthetic air A) prior degassing of the samples, B) of samples at 500 °C, and C) at 800 °C with increasing amount of salt.

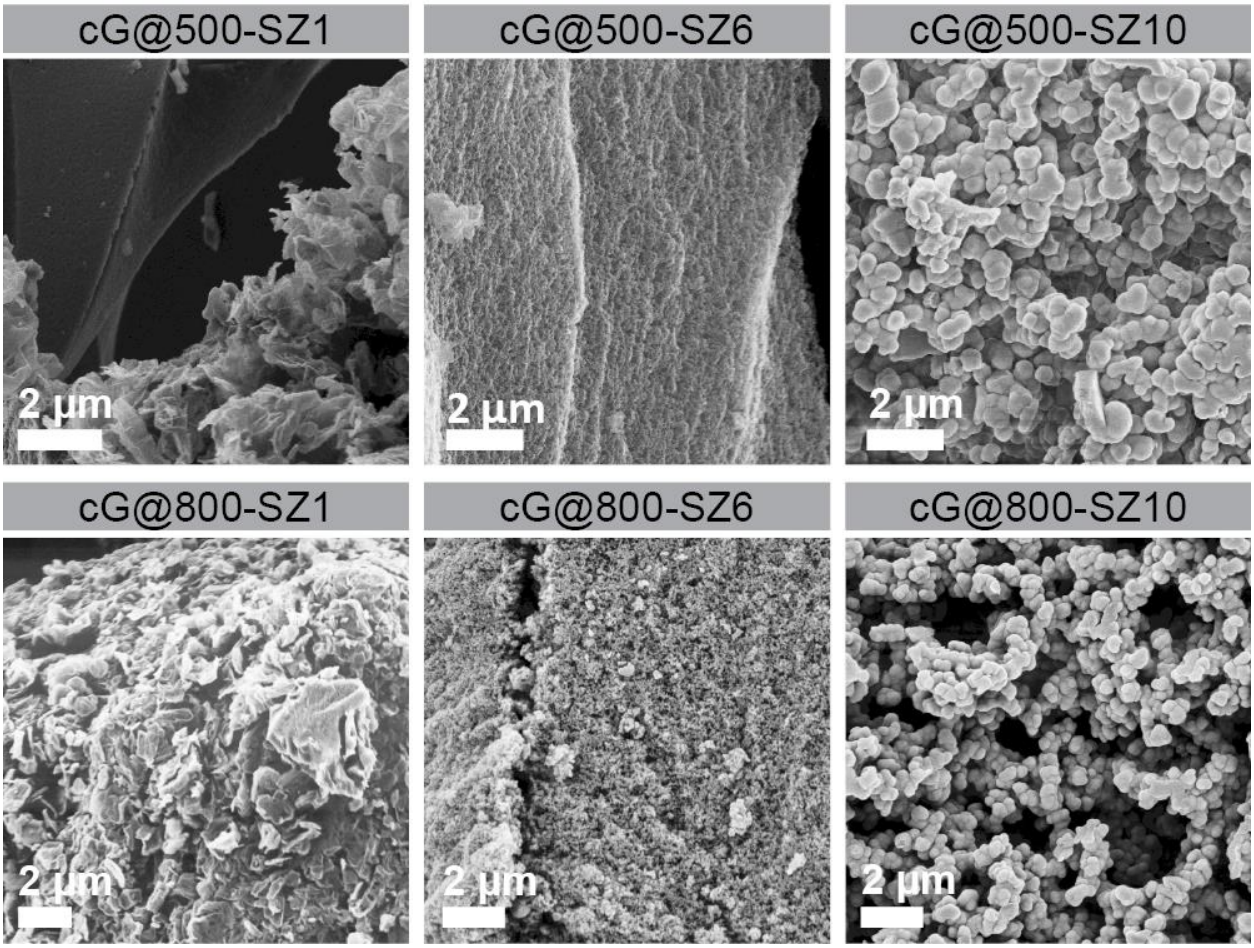

Figure S 4.2-3. SEM micrographs of guanine condensed at A) 500 °C and B) 800 °C with increasing amount of salt melt.

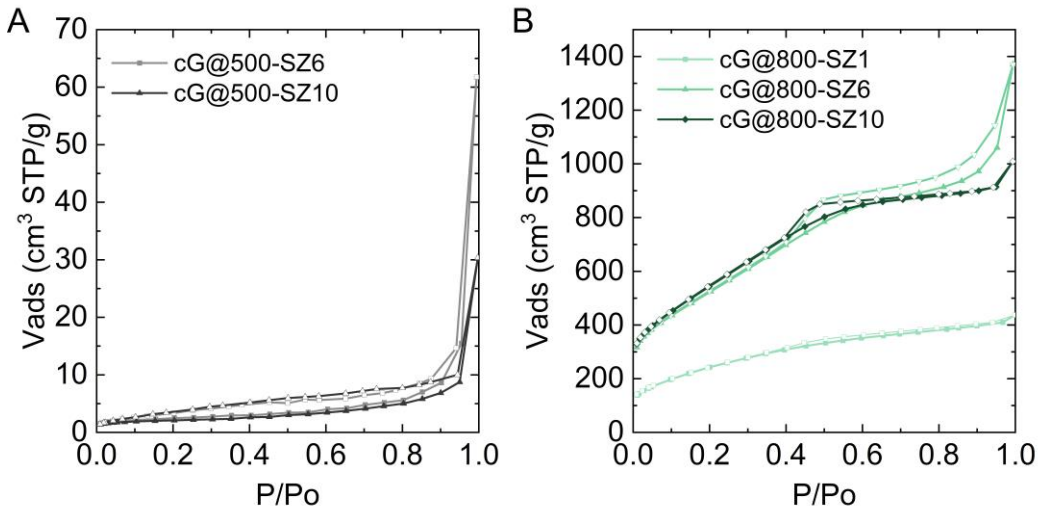

Figure S 4.2-4. Nitrogen adsorption (filled symbols)/desorption (empty symbols) at 77 K of guanine condensed at A) 500 °C and B) 800 °C with increasing amount of salt melt.

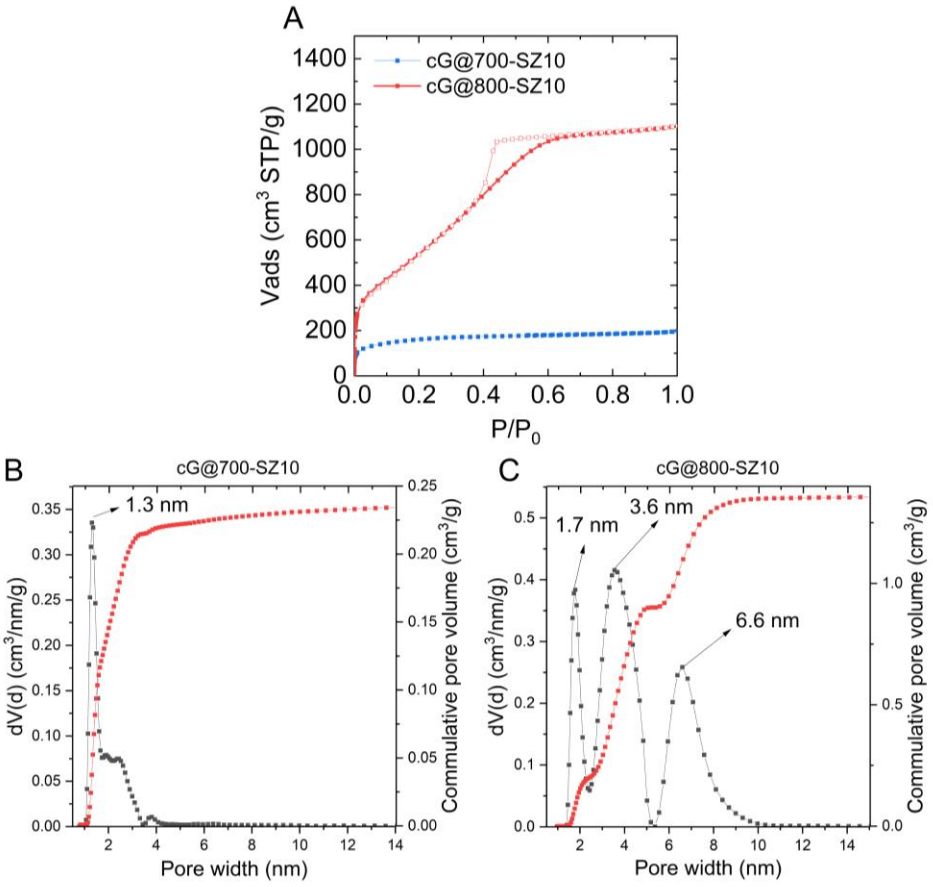

Figure S 4.2-5. Argon physisorption isotherms at 87 K A) and B) DFT pore size distribution of cG@700-SZ10 and C) cG@800-SZ10.

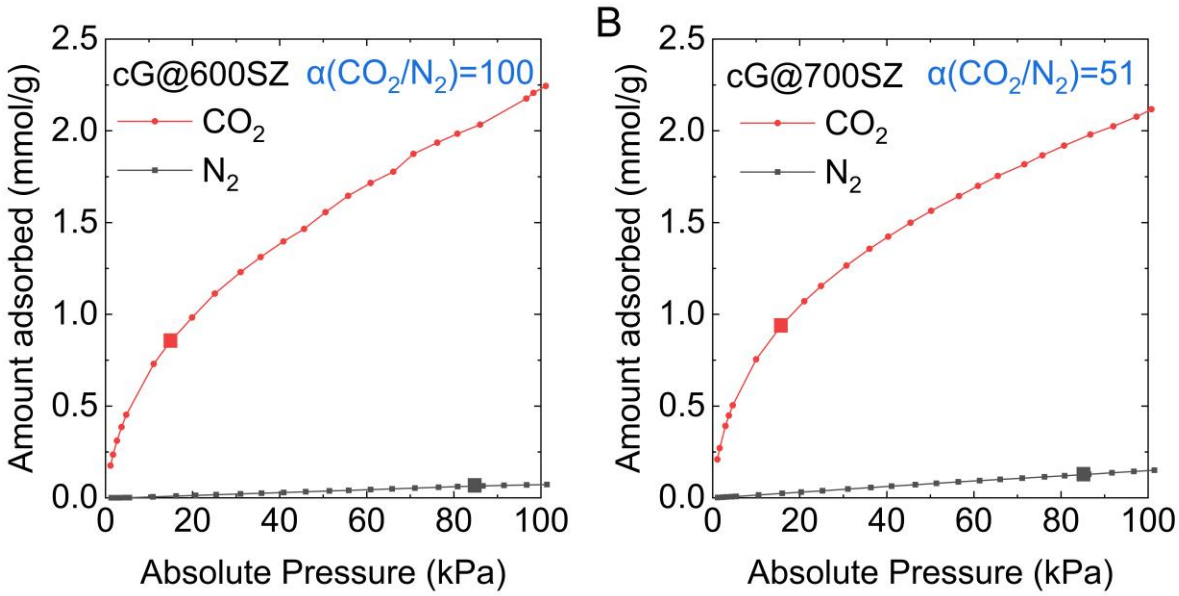

Figure S 4.2-6. CO_2 and N_2 adsorption isotherm at 298 K and calculated $IAST_{CO2N2}$ of A) cG@600-SZ10 and B) cG@700-SZ10.

Table S 4.2-2. Literature overview on Knoevenagel condensation reactions run using nitrogen-doped materials as catalysts.

Material	Nitrogen	S_{BET}	Pre-treatment	Reaction compounds	Reaction time / rate	Conversion / selectivity	Ref.
	wt%	$m^2\ g^{-1}$		Benzaldehyde +	h/ mmol $g^{-1}h^{-1}$	%	
N-doped Carbon	-	625	200 °C, 60 min, argon	Ethylcyanoacetate	20	32.7 / 13.7	[268]
C_3N_4-TEOS	-	-	200 °C, 60 min, argon	Ethylcyanoacetate	20	100 / 50.9	[268]
BS-700	4.4	4	-	Malononitrile	-	2.2 / 100	[269]
BSNC-600	4.7	962	-	Malononitrile	-	8.3 / 100	[269]
BSNC-700	2.8	1475	-	Malononitrile	-	16.1 / 100	[269]
BSNC-700-tBU	2.8	1475	tBU (1.0 M)	Malononitrile	-	79.9 / 100	[269]
BSNC-800	1.1	2271	-	Malononitrile	-	8.2 / 100	[269]
MM-NH2	1.6	120	Post functionalized with propargylamine	Malononitrile	20	73 / -	[270]
FM-NH2	5.9	480	Post functionalized with propargylamine	Malononitrile	20	74 /-	[270]
MS-NH2	2.1	225	Post functionalized with propargylamine	Malononitrile	20	92 / -	[270]
FS-NH2	3.5	758	Post functionalized with propargylamine	Malononitrile	20	76/ -	[270]
HC-10Bu2IMBr	8.2	170	-	Malononitrile	12	98/ -	[271]
HC-10Bu2IMBr	8.2	170	-	Acetophenon	20	99/ -	[271]
Mpg-C3N4	-	-	-	Malononitrile	2	33 / 74	[272]
Mpg-C3N4-tBu	-	-	tBuOk	Malononitrile	2	80 / 96	[272]
PAN-C500-AO400	17.3 (at.)		-	Ethyl cyanoacetate	- / 199	- / -	[273]

Supporting Information for section 4.3

Hydrophilic Porous Carbonaceous Materials derived from Uric Acid

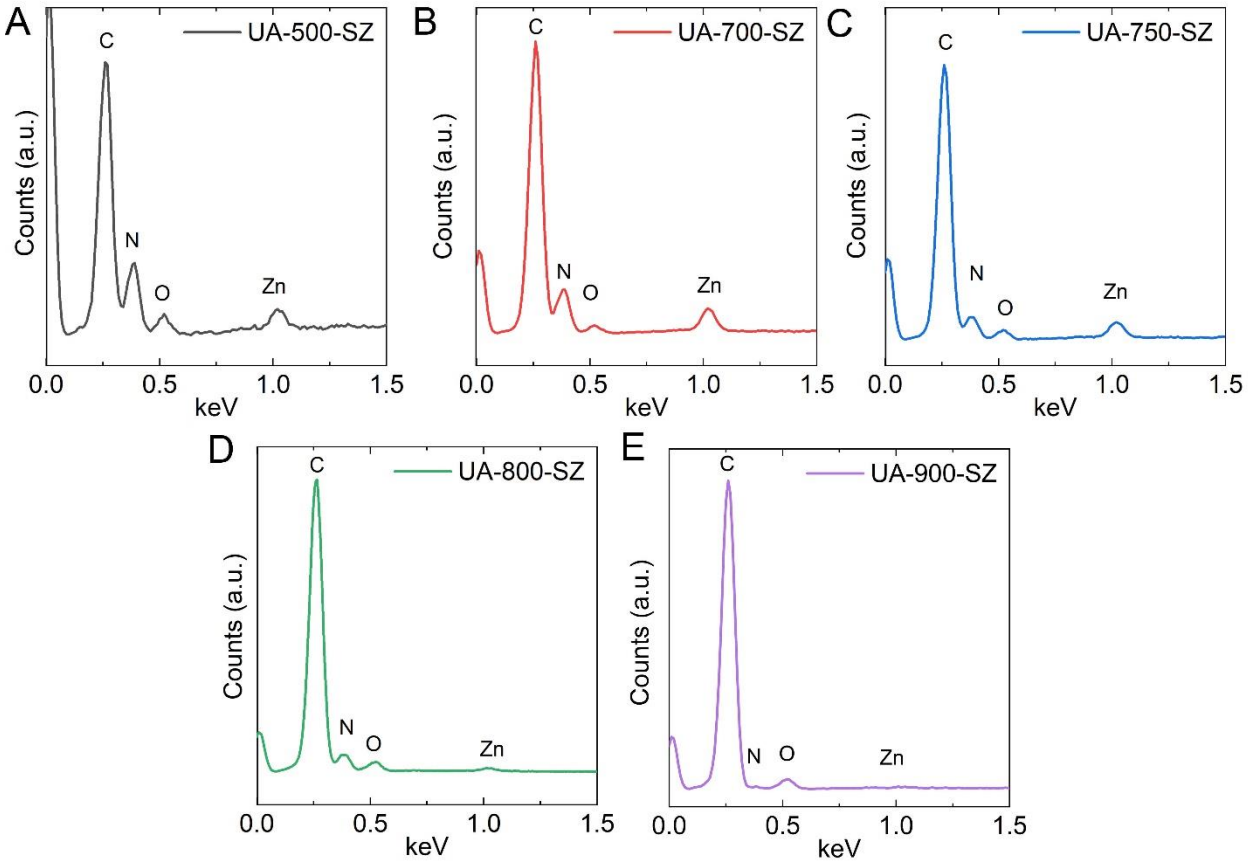

Figure S 4.3-1. EDX spectra of UA-500-SZ, UA-700-SZ, UA-750-SZ, UA-800-SZ, and UA-900-SZ with corresponding elements.

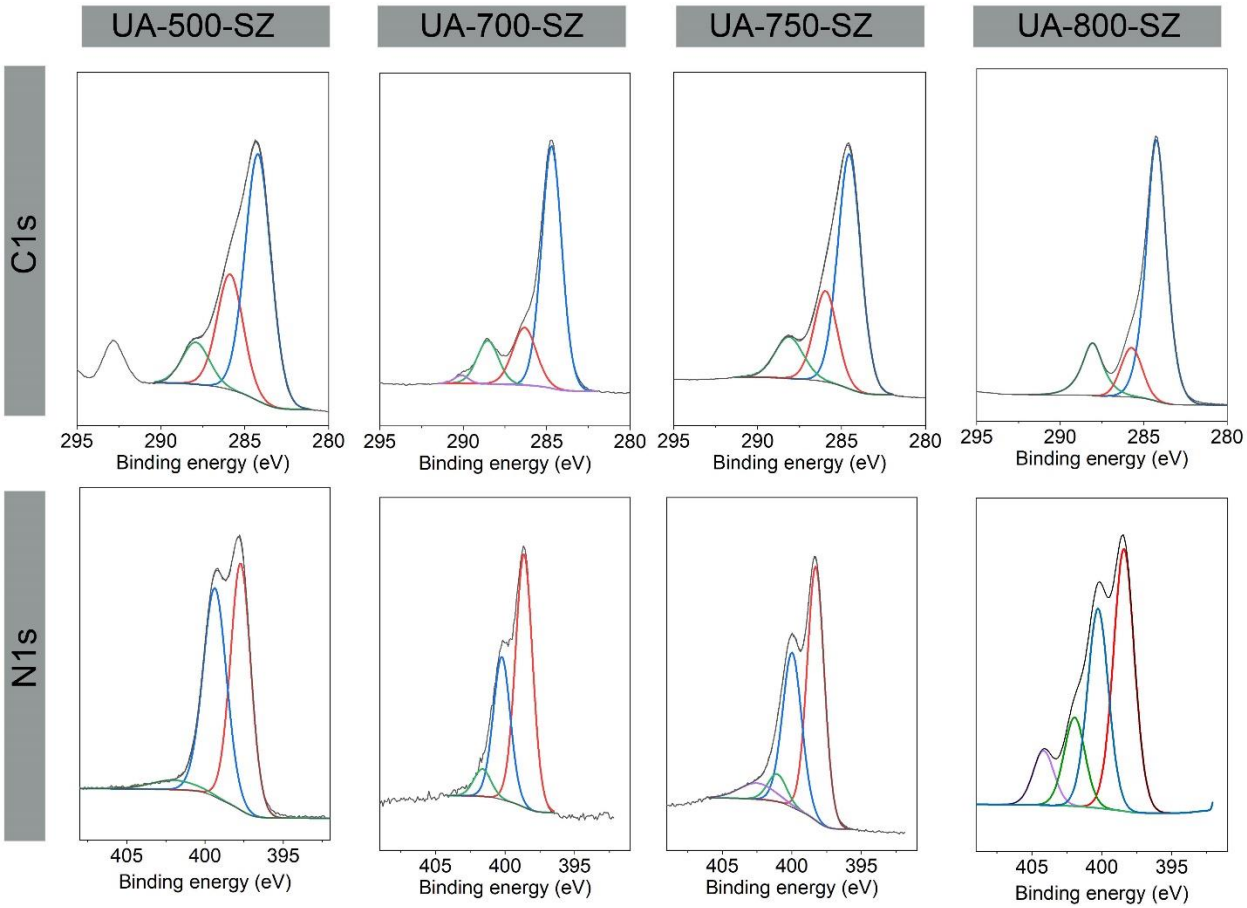

Figure S 4.3-2. XPS spectra and deconvolution if C1s and N1s peak of UA-500-SZ, UA-700-SZ, UA-750-SZ, and UA-800-SZ.

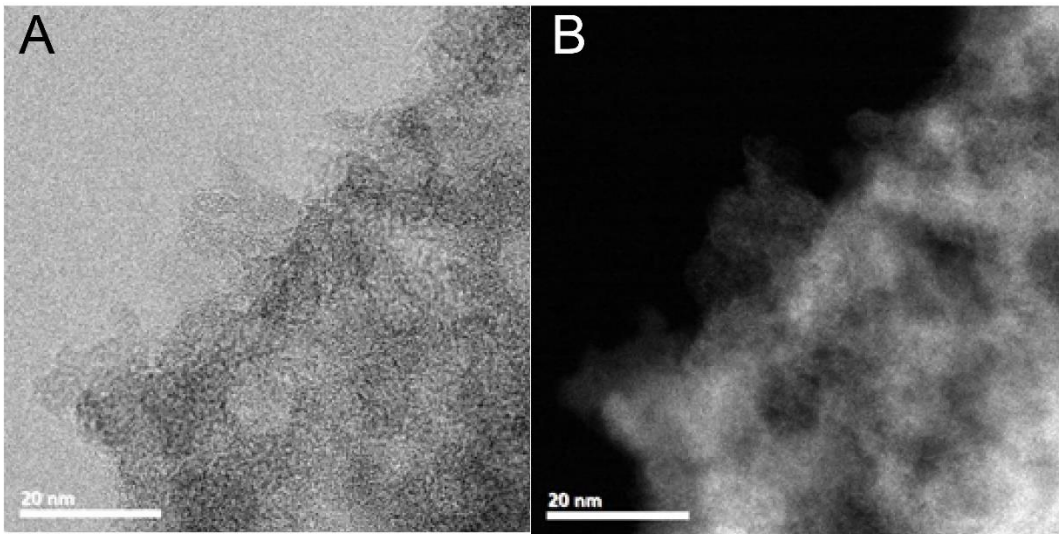

Figure S 4.3-3. A) BF-STEM and B) HAADF-STEM image of UA-800-SZ.

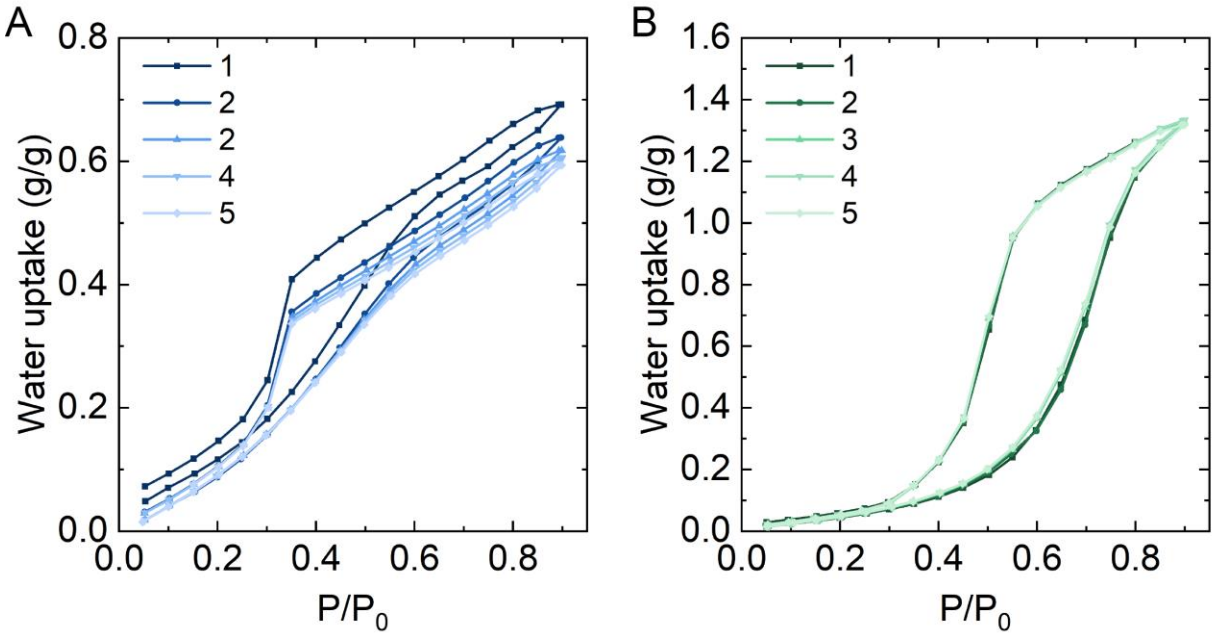

Figure S 4.3-4. A) UA-750-SZ and B) UA-800-SZ water vapor adsorption and desorption isotherms at 298 K. Stability tested by running 5 cycles without any degassing step in between measurements.

Table S 4.3-1. Literature compare of carbon based materials for water sorption (three of the best MOF materials are listed at the bottom for direct comparison). Listed parameters are oxygen and nitrogen content of the materials, BET surface area, pore volume of pores smaller than 2 nm (V_{micro}) and 7 nm (V_{meso}), and maximum water uptake.

Sample	Material	O / N content	SSA_{BET}	V_{micro}	V_{meso}	Max. H_2O uptake	Ref.
		at/at	$m^2\ g^{-1}$	$cm^3\ g^{-1}$	$cm^3\ g^{-1}$	$g\ g^{-1}$	
UA-500-SZ	NdC[a]	5 / 46	1	0.059	0.000	0.18	This work
UA-700-SZ	NdC	2 / 30	770	0.238	0.320	0.30	
UA-750-SZ	NdC	3 / 24	1547	0.328	0.760	0.69	
UA-800-SZ	NdC	2 / 14	2590	0.383	1.750	1.38	
C-HAT-CN-700	NdC	1.7 / 37.1	785	0.300	-	0.23[f]	[274]
N-RFCC	NdC	- / 8.0 wt%	1000	0.320	0.590	0.70[f]	[275]
HOMC	NdC	- / 14.0 wt%	1031	0.240	1.050	0.68	[276]
GU13-350	OdC[b]	17.7 / 4.3	17	0.000	-	0.34 [f]	[111]
GU13-500	OdC	13.3 / 4.5	1227	0.350	-	0.08 [f]	
PCC-1	OdC	26.0 / 14.0	826	-	-	0.32	[277]
A-p900-CO2-3h	OdC	7.7/ 4.3	1207	5.734	0.037	0.46	[278]
A-p900-1:1-KOH-1	OdC	3.3 / 0.4	839	0.400	0.021	0.40 [f]	[279]
NAC-K(700)	OdC	29.4 / 1.6 mmol g	2045	0.620	-	0.75 [f]	[280]
$NC_{ZIF\text{-}8}$1000A	OdC	8.6 / 1.1	3096	0.840	2.010	1.67	[281]
RUF-p900-CO3-3h	OdC	12.2 / 2.6	1075	0.510	-	0.50	[282]

Sample	Material	O / N content at/at	SSA_{BET} $m^2\ g^{-1}$	V_{micro} $cm^3\ g^{-1}$	V_{meso} $cm^3\ g^{-1}$	Max. H_2O uptake $g\ g^{-1}$	Ref.
UMC350	OdC	14.2 / -	1420	0.516	0.516	0.64	[283]
PMC550	PC[c]	-	2240	0.788	0.821	0.85	
CMK-8	OMC [d]	-	1373	-	-	0.89	[284]
CMK-1	OMC	-	1411	-	-	0.60	
CMK-8	OMC	-	1373	-	-	0.89	[185]
PIT11	MC[e]	-	2000	1.100	-	0.80	[285]
TpPa-1	COF[f]	-	984	-	-	0.44	[286]
bipy-CTF500	CTF[g]	- / 16.4	1548	0.640	0.710	0.44	[287]
pym-CTF500	CTF	- / 33.8	208	-	-	0.24	
Cr-soc-MOF-1	MOF[h]	-	4549	-	-	2.00	[177]
MIL-101Cr	MOF	-	2059	-	-	1.00	[168]
Co_2Cl_2(BTDD)	MOF	-	1912	-	-	0.97	[288]

[a] N rich carbonaceous materials (NdC); [b] O rich carbonaceous materials (OdC), ; [c] Porous carbon (PC); [d] Ordered mesoporous carbons (OMC); [e] Microporous materials (MC); [h] Metal-organic framework (MOF); [f] estimated from a figure.

Supporting Information for section 5

Cu(II)/Cu(I) Nanocluster Decorated N-Doped Carbonaceous Materials for Fast and Durable Oxygen Reduction Reaction

Table S 5-1. Composition according to SEM-EDX of BTCN-Cu0 and BTCN Cu0 heat-treated at 350 °C for 1h in air atmosphere.

Sample	SEM-EDX (at%)			
	C	N	O	C/N
BTCN-Cu0	74.0 (2)	20.4 (2)	5.0 (1)	3.6 (0.4)
BTCN-Cu0 350°C air	72.0 (1)	21.2 (1)	6.0 (1)	3.4 (0.2)

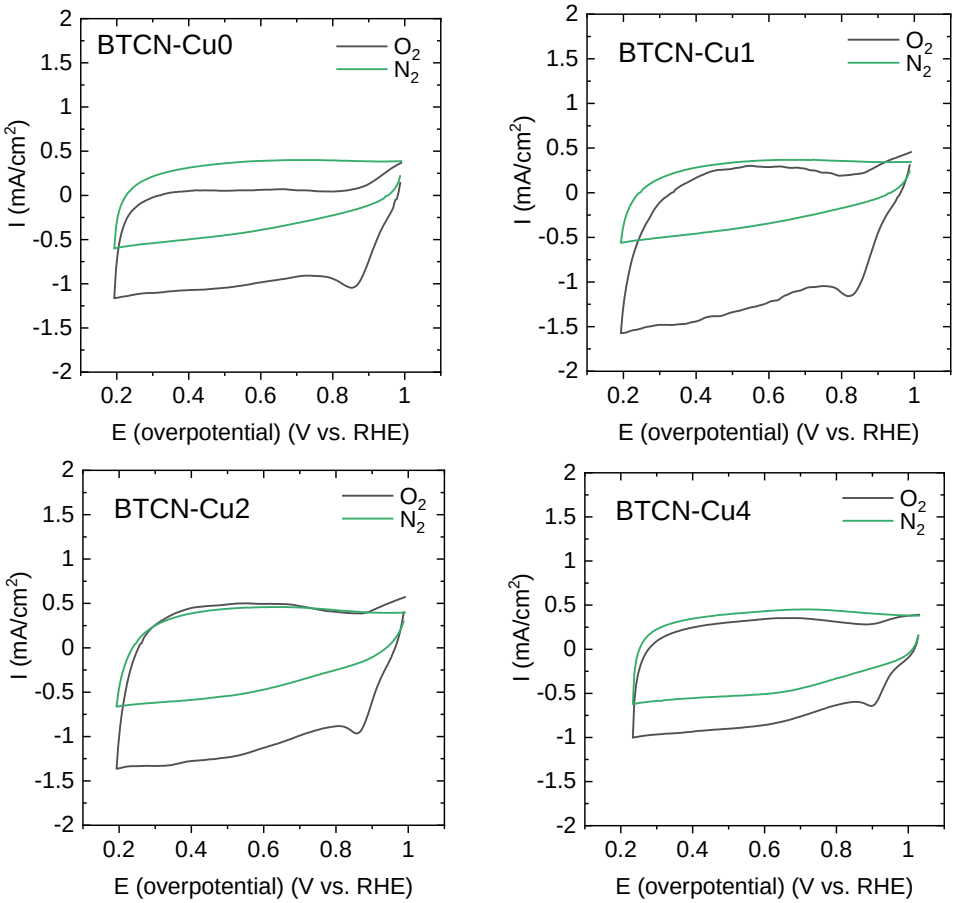

Figure S 5-1. CV curves of BTCN-CuX in nitrogen (green) and oxygen (black) saturated 0.1 M KOH solution at a scan rate of 10 mVs^{-1}.

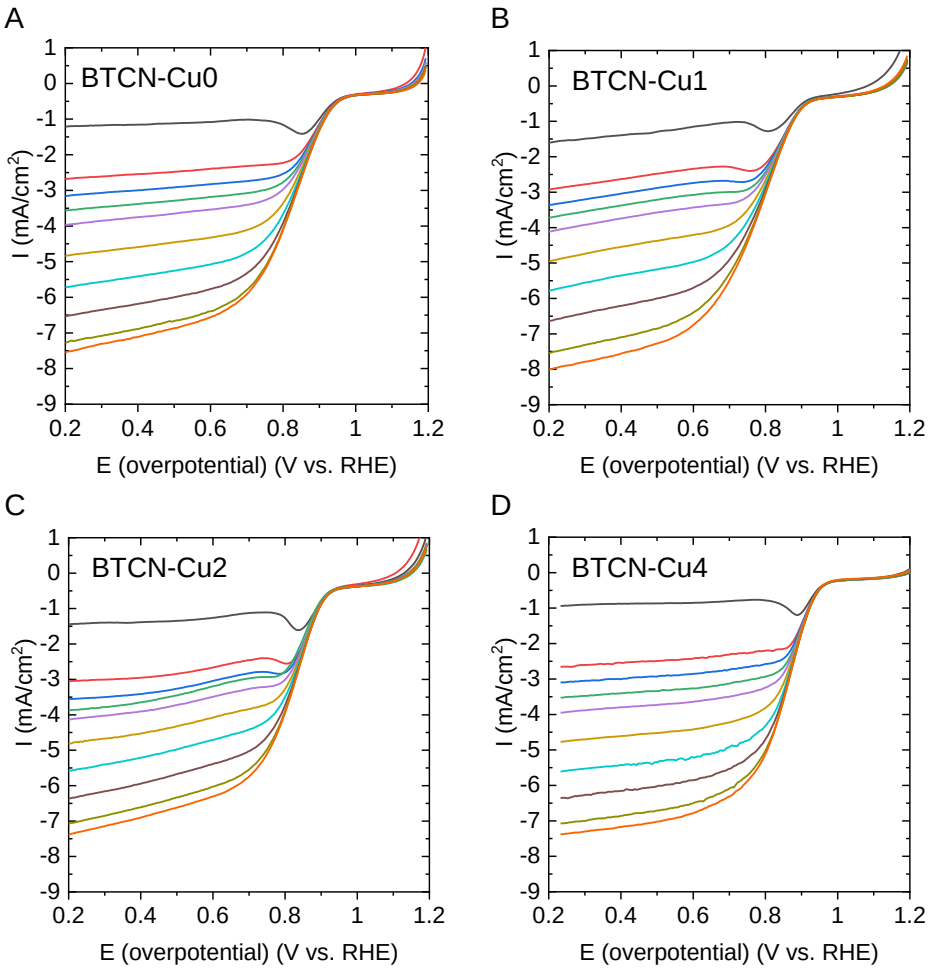

Figure S 5-2. Linear sweep voltammetry curves at different rotation speeds (from top to bottom: 0, 200, 300, 400, 500, 750, 1000, 1250, 1500, 1600 rpm) of A) BTCN-Cu0, B) BTCN-Cu1, C) BTCN-Cu2 and D) BTCN-Cu4.

Table S 5-2. Literature overview of the ORR performance of Cu-NCs obtained from RDE in 0.1 M KOH. Compare parameter are the onset potential (E_{Onset}), the half-wave potential ($E_{1/2}$), and the limiting current (J_L).

Sample	E_{Onset} V	$E_{1/2}$ V	J_L mA cm^{-2}	Ref.
cBTCN-Cu0	**0.93**	**0.83**	**-7.0**	
BTCN-Cu1	**0.81**	**0.78**	**-7.4**	
BTCN-Cu2	**0.91**	**0.83**	**-5.1**	**This work**
BTCN-Cu4	**0.94**	**0.86**	**-7.0**	
Carbon/Pt 20%	1.00	0.92	-6.5	
Cu SAC	0.97	0.81	5.5*	[191]
Cu-N-C	0.92	0.87	5.8*	[187]
Cu SAs/N-C	0.97	0.90	5.5*	[289]
Cu-N@C-60	0.89	0.78	-	[218]
N-rGO\Cu3N	0.89	0.7	-	[192]
Cu ISAS/N-C	1.05	0.92	-	[290]
Cu-NGS	0.92	0.81	5.84	[186]
Cu/G		0.85	3.79	[214]

* Numbers not given, estimated from a graph

8.4.1 List of Figures

8.4.2 List of Tables

List of Publications

1. N. Lopez-Salas, **J. Kossmann**, M. Antonietti, Accounts of Materials Research, Rediscovering Forgotten Members of the Graphene Family, (2020), 1, (2) 117-122.
2. **J. Kossmann**, D. Piankova, N.V. Tarakina, J. Heske, T.D. Kühne, J. Schmidt, M. Antonietti, N. López-Salas, Carbon, Guanine condensates as covalent materials and the concept of cryptopores, (2020), 172, 497-505.
3. **J. Kossmann**, T. Heil, M. Antonietti, N. López-Salas, ChemSusChem, Guanine Derived Porous Carbonaceous Materials: towards C1N1, (2020), 13, 6643.
4. **J. Kossmann**, R. Rothe, T. Heil, M. Antonietti, N. López-Salas, J. Colloid Interface Sci., Ultrahigh water sorption on highly nitrogen doped carbonaceous materials derived from uric acid, (2021), 602, 880-888.
5. **J. Kossmann**, M. L. Ortíz Sánchez-Manjavacas, H. Zschiesche, N. Tarakina, M. Antonietti, J. Albero, N. López Salas, J. Mater. Chem. A, CuII/CuI decorated N-doped noble carbonaceous electrocatalysts for the oxygen reduction reaction, (2022).

Declaration

Die vorliegende Dissertation entstand in dem Zeitraum zwischen April 2019 und September 2021 am Max-Planck-Institut für Kolloid- und Grenzflächenforschung unter Betreuung von Prof. Dr. Dr. h.c. Markus Antonietti.

Hiermit erkläre ich, dass die vorliegende Arbeit selbstständig angefertigt wurde und keine anderen als die angegebenen Hilfsmittel und Quelle verwendet wurden.

Die Arbeit wurde bisher weder im Inland noch im Ausland in gleicher oder ähnlicher Form einer anderen Prüfungsbehörde vorgelegt.

Es haben bisher keine früheren erfolglosen Promotionsverfahren stattgefunden.

The present work was carried during the period between april 2019 and august 2021 at the Max Planck Institute of Colloids and Interfaces under the supervision of Prof. Dr. Dr. h.c. Markus Antonietti.

I declare that I have written this work on my own and used no other than the named aids and references.

This thesis was not submitted to another examination board in this or other countries. There were no unsuccessful examination processes.

Janina Kossmann

Potsdam, 26.01.2022